COMPUTATIONAL INVESTIGATION OF THE INFLUENCE OF HEATING MODES AND MOISTURE CONTENT ON PYROLYSIS AND IGNITION OF LIVE FUELS

by

BANGALORE LINGARAJ YASHWANTH

A DISSERTATION

Submitted in partial fulfillment of the requirements
for the degree of Doctor of Philosophy
in
The Department of Mechanical and Aerospace Engineering
to
The School of Graduate Studies
of
The University of Alabama in Huntsville

HUNTSVILLE, ALABAMA

2015

In presenting this dissertation in partial fulfillment of the requirements for a doctoral degree from The University of Alabama in Huntsville, I agree that the Library of this University shall make it freely available for inspection. I further agree that permission for extensive copying for scholarly purposes may be granted by my advisor or, in his/her absence, by the Chair of the Department or the Dean of the School of Graduate Studies. It is also understood that due recognition shall be given to me and to The University of Alabama in Huntsville in any scholarly use which may be made of any material in this dissertation.

Bangalore Lingaraj Yashwanth (date)

DISSERTATION APPROVAL FORM

Submitted by Bangalore Lingaraj Yashwanth in partial fulfillment of the requirements for the degree of Doctor of Philosophy in Mechanical Engineering and accepted on behalf of the Faculty of the School of Graduate Studies by the dissertation committee.

We, the undersigned members of the Graduate Faculty of The University of Alabama in Huntsville, certify that we have advised and/or supervised the candidate of the work described in this dissertation. We further certify that we have reviewed the dissertation manuscript and approve it in partial fulfillment of the requirements for the degree of Doctor of Philosophy in Mechanical Engineering.

_____ Committee Chair
Dr. Babak Shotorban (Date)

_____
Dr. Shankar Mahalingam (Date)

_____
Dr. Kader Frendi (Date)

_____
Dr. Gabriel Xu (Date)

_____
Dr. David R. Weise (Date)

_____ Department Chair
Dr. Keith Hollingsworth (Date)

_____ College Dean
Dr. Shankar Mahalingam (Date)

_____ Graduate Dean
Dr. David Berkowitz (Date)

ABSTRACT

School of Graduate Studies
The University of Alabama in Huntsville

Degree Doctor of Philosophy College/Dept. Engineering/Mechanical and Aerospace Engineering

Name of Candidate Bangalore Lingaraj Yashwanth

Title Computational investigation of the influence of heating modes and moisture content on pyrolysis and ignition of live fuels

The burning of an isolated leaf-like element was computationally investigated in a series of studies, motivated by recent burning experiments performed on live leaves of manzanita (*Arctostaphylos glandulosa*). In this study, the relative importance of heating modes, effect of fuel moisture content on pyrolysis and combustion of live fuels is explored in stages. A preliminary study was conducted on a simplified one-dimensional configuration, using Gpyro. The heating sources were modeled through convection and/or radiation as boundary conditions. Results showed that the increase in radiative source temperature substantially affects ignition time; however, it has marginal influence on mass loss rate and charring rate. The increase of convective heating source temperature in presence of radiation had a marginal impact on ignition time and no influence on mass loss or charring rate. Next studies were conducted in full three dimensional configurations via Gpyro-3D/FDS. The solid fuel was under the radiative heating and a 5-step chemical kinetic mechanism was used for pyrolysis. Results indicated that temperature response and thermal degradation rate was higher for lower fuel moisture content (FMC) case and ignition occurred prior to

the higher FMC case. In the gas phase, high volume fraction of water vapor observed in the region close to the combustion zone as well as away from this region illustrated that evaporation and ignition occur together. In the next task of the modeling activities, an improved chemistry model was used, which included hemicellulose and lignin along with cellulose and moisture. A more advanced 12-step kinetic mechanism was used for the solid phase to simulate the multi-component decomposition process in detail. The solid fuel was oriented horizontally to mimic the burning experiments of individual leaves of manzanita by the Flat Flame Burner (FFB) apparatus and was exposed to convective heating. The simulations were consistent with the experimental results in terms of ignition and burnout time prediction, fire initiation and spread pattern. Local evaporation of moisture and temperature rise at the periphery of the solid fuel was observed, also a significant amount of moisture remained at the center of sample at the time of ignition indicating that different points in the domain evaporate and pyrolyze at different times. In the final study, the effect of both convection and radiation was investigated with the fuel element oriented vertically. Evaporation occurred at a higher rate near the leading, lateral and trailing edge of the solid fuel compared to the region located at the center. This pattern of heating was either due to the flame tilt observed during simulation or due to the effect of fluid dynamics. A boundary layer growth was observed above the surface of the solid fuel which reduces the heat transfer to the region located at the center. When radiation was used along with convective heating source, the peak value of mass loss rate was 20% higher than that in convection-only case.

Abstract Approval: Committee Chair _____
Dr. Babak Shotorban

Department Chair _____
Dr. Keith Hollingsworth

Graduate Dean _____
Dr. David Berkowitz

ACKNOWLEDGMENTS

I would like to thank my advisors, Dr. Babak Shotorban and Dr. Shankar Mahalingam, for giving me the opportunity to explore this fascinating field of fire modeling and providing the necessary guidance during the course of my research. I have benefited immensely from the discussions with members of the experimental group at Brigham Young University and Pacific Southwest Research Station. I also have to thank the members of my PhD committee, Drs. Kader Frendi, Gabriel Xu and David Weise for their helpful career advice and suggestions in general. I would like to thank my research colleagues Chandana Anand, Satyajeet Padhi, Selina Ferguson, Ambarish Dahale, Shreyas Bidadi, Rohit Dhariwal, Vijay Rani, Nishant Goli and Seyed Sadreddin Mirshafieyan for their useful suggestions. I am also thankful to the extremely friendly office staff at my university for their help. I would especially like to thank my family members, friends and others for their moral support which allowed me to pursue higher education and has always helped me overcome obstacles in life.

I would like to acknowledge USDA Forest Service PSW Research Station through cooperative agreement 11-JV-11272167-103 with The University of Alabama in Huntsville for providing the required financial support. The high performance computing (HPC) resources are provided by the Alabama Supercomputer Authority (ASA).

TABLE OF CONTENTS

List of Figures **xi**

List of Tables **xvii**

List of Symbols **xviii**

Chapter

1 Introduction **1**

1.1 Forest Fuel 5

1.2 Fuel Moisture Content 7

1.3 Heating Modes 9

1.4 Wildland Fire Modeling Approaches 13

1.5 Motivation 16

1.6 Outline 17

2 Physical Models **18**

2.1 Governing Equations 20

2.1.1 Gas-phase Equations 21

2.1.1.1 Chemical Reactions 25

2.1.1.2 Thermal Radiation Transport 25

2.1.1.3 Convective Heat Transfer 26

2.1.2 Solid-phase Equations 27

3 An Investigation of the Influence of Heating Modes on Ignition and Pyrolysis of a Slab of Wood 33

3.1 Introduction 33

3.2 Physical Configuration 35

3.2.1 Chemically Inactive Media 37

3.2.2 Chemically Active Media 39

3.3 Results and Discussions 41

3.4 Chapter Summary 52

4 Horizontal Fuel Configuration: Influence of Moisture Content and Radiative Heat Transfer 54

4.1 Introduction 54

4.2 Physical Configuration 57

4.2.1 Chemical Reactions 59

4.2.2 Thermophysical Properties 62

4.3 Model Verification and Validation 63

4.4 Results and Discussions 68

4.5 Chapter Summary 86

5 Horizontal Fuel Configuration: Influence of Moisture States and Convective Heat Transfer 87

5.1 Introduction 87

5.2 Computational Setup 89

5.3 Reaction Mechanism and Models 91

5.4 Chemical Kinetic Model Validation 96

5.5 Results and Discussion 97

5.6 Chapter Summary 115

6 Vertical Fuel Configuration: Investigation of the Effect of Heating Modes 117

6.1 Introduction 117

6.2 Computational Setup and Model 118

6.3 Results and Discussion 122

6.3.1 Convection-only Heating 122

6.3.2 Combined Convection and Radiation Heating 134

6.4 Chapter Summary 136

7 Conclusions and Future Work 137

7.1 Summary and Conclusions 137

7.2 Future Work 140

REFERENCES 148

LIST OF FIGURES

FIGURE PAGE

1.1 Various ignition phenomena. 4

2.1 Schematic figure showing different physical phenomena during a wildfire [1]. 19

2.2 Physical processes considered during the combustion of a solid fuel. . 19

2.3 Schematic represeing bilinear interpolation used to couple the solid-fuel domain solver variables to gas phase solver variables. FDS and Gpyro3D cells are shown by dark and gray solid lines respectively. . . 31

3.1 Schematic diagram of the physical configuration. A one dimensional slab of woody fuel of width L is subject to heating by either convection (hot air), radiation (heater), or mixed mode heat transfer. 36

3.2 Time history of temperatures at depths 0 mm (circle symbol), 5 mm (square symbol), and 10 mm (triangular symbol) from the surface of white pine irradiated at 40 kW/m^2 in nitrogen atmospheres in the configuration studied experimentally (dotted line) by Ohlemiller *et al.* [2], computationally with a two-step reaction (dashed line) by Lautenberger & Fernandez-Pello [3], and computationally with a single-step reaction in the present study (solid line). 41

3.3 Comparison of spatial variation of non-dimensional temperature between Gpyro and available analytical solution at various time instants. 42

3.4 Critical time against (a) heating source temperature (θ_{source} represents θ_h and θ_∞ in radiation and convection heating, respectively), and (b) total energy delivered in chemically inert media. 42

3.5 The dependence of critical time on source temperature for convective mode of heating, Bi = 7.6. 43

3.6 Critical time against convective source temperature for different Biot numbers under (a) convective mode of heating; and (b) combined convective and radiative mode of heating with $\theta_h = 3$. 45

3.7 Critical time against heater temperature in radiative mode of heating and combined radiative and convective mode of heating with θ_∞ = 2.33 and Bi = 7.6. 45

3.8 Time evolution of mass loss rate in g/m^2/s for convective mode of heating (left column) and combined convective and radiative mode of heating with θ_h = 3 (right column); (a, b) Bi = 7.6; (c, d) Bi = 9.2; and (e, f) Bi = 11.4. 47

3.9 Time evolution of the mass loss rate under (a) radiative mode of heating; (b) combined radiative and convective mode of heating with θ_∞ =2.33 and Bi = 7.6. 48

3.10 Charring rate in mm/s plotted as a function of dimensionless position, ξ in convective mode of heating (left column) and combined convective and radiative mode of heating with θ_h = 3 (right column) for (a, b) Bi = 7.6; (c, d) Bi = 9.2; and (e, f) Bi = 11.4. 50

3.11 Charring rate in mm/s versus dimensionless position ξ under (a) radiative mode of heating; (b) combined radiative and convective mode of heating with θ_∞ = 2.33 and Bi = 7.6. 52

4.1 (a) Isometric view of computational domain showing thin cellulose particle subjected to radiative heating from surface at x = -0.09 m and (b) two-dimensional view of computational domain along the xz-slice at y = 0. Point A located at x = -0.02 m, y = 0, z = 0.031 m is considered for analysis. 58

4.2 Verification of results of current study using Gpyro for cellulose pyrolysis with simulations of Di Blasi [4]. Quantities are plotted along the length of the specimen at different times; (a) temperature (b) mass concentration of active cellulose and (c) velocity of gas species. 67

4.3 Verification of results of current study using Gpyro TGA setup (solid line) with TGA data of Reed and Posey [5] (crossmarks). 68

4.4 Time history of (a) temperature, and (b) mass fraction of moisture at point A (see fig. 6.1) for three cases with an initial FMC of 5, 40 and 80%. 71

4.5 Variation of (a) temperature and (b) mass fraction of moisture along x at y = 0 and z = 0.031 m at time 5s in the solid phase for three cases with an initial FMC of 5, 40 and 80%. 72

4.6 Time history of (a) mass loss rate and (b) normalized mass in the solid phase for three cases with an initial FMC of 5, 40 and 80%. 73

4.7 Time history of (a) heat release rate and (b) burn rate in the gas phase for three cases with an initial FMC of 5, 40 and 80%. 74

4.8 Time history of (a) solid species and (b) gas species in the solid phase for a case with an initial FMC of 80% at point A. 75

4.9 Variation of moisture mass fraction (a) along x at $y = 0$ and $z = 0.031$ m and (b) along y at $x = 0.0125$ m and $z = 0.031$ m at various times in the solid phase for a case with an initial FMC of 80%. . . . 76

4.10 Contours of moisture mass fraction in the solid fuel along x at (a) $t = 5$ s (b) $t = 6.5$ s and (c) $t = 7.75$ s on an xy-slice located at $z = 0.031$ m for a case with an initial FMC of 80%. 78

4.11 Variation of mass fraction of tracked gas species at time (a) 5 s (b) 7.5 s and (c) 11 s along x at $y = 0$ and $z = 0.035$ m in the gas phase domain for a case with an initial FMC of 80%. 79

4.12 Gas phase contours of (a) temperature (°C), (b) water vapor mass fraction and (c) oxygen mass fraction at $t = 5$ s on an xz-slice located at $y = 0$ for a case with an initial FMC of 80%. 82

4.13 Gas phase contours of (a) temperature (°C), (b) water vapor mass fraction and (c) oxygen mass fraction along x at $t = 7.5$ s on an xz-slice located at $y = 0$ for a case with an initial FMC of 80%. 83

4.14 Gas phase contours of (a) temperature (°C), (b) water vapor mass fraction and (c) oxygen mass fraction along x at $t = 11$ s on an xz-slice located at $y = 0$ for a case with an initial FMC of 80%. 84

4.15 Time history of global radiation and convection fluxes for a case with FMC of 80%. Positive heat flux means heat is transferred from gas to solid particle and negative heat flux means vice versa. 85

4.16 (a) Gas phase temperature contours (°C), and (b) velocity vectors at time 15 s on an xz-slice located at $y = 0$ for a case with an initial FMC of 80%. 85

5.1 (a) Isometric view of computational domain showing thin solid fuel subjected to convective heating from the burner, (b) two-dimensional view of computational domain along the zy-slice at $x = 0$. Point A is located at y = -0.015 m, $x = 0$, $z = 0.051$ m. 90

5.2 Generic reaction scheme used to model cellulose, hemicellose and lignin pyrolysis [6] along with vaporization reaction of moisture. 92

5.3 Results obtained in the current study (dark line) with simulation results of Miller & Bellan [6] (colored line with symbols) and TGA experimental results of Koufopanos *et al.* [7] (colored symbols) for various heating rates. 97

5.4 Time histories of (a) mass loss rate, (b) temperature at point A (solid line) with experimental results of Pickett *et al.* [8] (symbols) for an initial FMC of 76%. 98

5.5 Time histories of (a) temperature, (b) free moisture mass fraction and (c) bound moisture mass fraction at point A for three cases with an initial FMC of 40, 76 and 120%. 100

5.6 Time histories of (a) mass loss rates, (b) normalized mass for three cases with an initial FMC of 40, 76 and 120%. 101

5.7 Time histories of heat release rates for three cases with an initial FMC of 40, 76 and 120%. 103

5.8 Time histories of (a) solid species and (b) gas species within the solid fuel at point A for a FMC of 76%. 104

5.9 Contours of bound water mass fraction in the solid fuel at (a) $t = 7$ s (b) $t = 7.3$ s on an xy-slice located at $z = 0.051$ m for a case with an initial FMC of 76%. 106

5.10 Color contours of (a) temperature (b) mass fraction of water vapor and (c) oxygen mass fraction in the gas phase at t =3 s on an xz-slice located at y =0 for a case with an initial FMC of 76%. 108

5.11 Color contours of (a) temperature (b) mass fraction of water vapor and (c) oxyegn mass fraction in the gas phase at t =8 s on an xz-slice located at y =0 for a case with an initial FMC of 76%. 109

5.12 Variation of mass fraction of tracked gas species at time (a) 3 s (b) 8 s along x at $y = 0$ and $z = 0.06$ m in the gas phase domain for a case with an initial FMC of 76%. 110

5.13 Contours of oxygen mass fraction and velocity vectors along an xz slice at $y = 0$for a case with an initial FMC of 76%. 112

5.14 (a)Time history of global radiation and convection fluxes for a case with FMC of 76%. (b) Close up of the figure during the initial preheating stage. Positive heat flux means heat is transferred from gas to solid particle and negative heat flux means vice versa. 114

5.15 Iso-surface of heat release rate (HRR) at $t = 9$s for a case with an initial FMC of 76%. 115

6.1 Figure 1: (a) Experimental apparatus: flat flame burner (A), radiant panel (B), IR camera (C), video camera (D), glass cage to prevent ambient air entrainment (E), sample location (F), mass balance (G) and sample holding rod (H); (b) Isometric view of computational domain showing a thin solid fuel subjected to combined convection and radiation surrounded by solid wall. 120

6.2 Comparison of time histories of mass loss rate (solid line) with experimental results of manzanita species (symbols) for an initial FMC of 65% using convection-only heating. 123

6.3 Time history of (a) temperature, and (b) mass fraction of free moisture (c) mass fraction of bound moisture at a point $x = y = 0, z = 0.04$m (see fig. 6.1) for three cases with an initial FMC of 44, 65 and 90%. . 124

6.4 Time history of (a) mass loss rate and (b) heat release rate in the solid phase for three cases with an initial FMC of 44, 65 and 90%. 126

6.5 Time history of (a) solid species and (b) gas species within the solid phase for a case with an initial FMC of 65% at point $x = y = 0, z = 0.04$m. 127

6.6 Variation of temperature along length of the solid fuel, z at $x = y = 0$ at various time instants for a FMC of 65% 128

6.7 Contours of temperature within the solid fuel along a zy slice at (a) $t = 7$ s (b) $t = 7.5$ s and located at $x = 0$ m for a case with an initial FMC of 65%. 130

6.8 Variation of temperature and vertical component of velocity along z axis at point $y = -0.0012$m and $x = 0$m at time $t = 4$s 130

6.9 Contours of moisture mass fraction in the solid fuel at (a) $t = 3$ s (b) $t = 3.5$ s and (c) $t = 4$ s on a xz-slice located at $y = 0$ m for a case with an initial FMC of 65%. 132

6.10 Contours of gas-phase temperature at times (a) $t = 3$ s, and (b) $t = 4.75$ s on a yz slice located at $x = 0$ for a case with an initial FMC of 65% using convection-only heating. 133

6.11 Comparison of time histories of mass loss rate (solid line) with experimental results of manzanita species (symbols) for an initial FMC of 65% using convection-only heating. 134

6.12 Comparison between time histories of (a) mass loss rate (b) heat release rate, using convection-only (solid line) and combined heating mode (dashed line) for an initial FMC of 65%. 135

1 Two dimensional contours of a) oxygen mass fraction b) mass fraction of carbon dioxide along a xy slice located at $z = 0.6$ for an initial FMC of 65%. 143

2 Two dimensional contours of water vapor mass fraction along a xz slice located at $y = 0$ for an initial FMC of 65%. 144

3 Iso-surface of a) temperature at 2000 ^{o}C and b) water vapor mass fraction value of $0.01, 0.03$ at $t = 9$s for an initial FMC of 65%. 145

4 Iso-surface of oxygen mass fraction value of $0.04, 0.23$ at $t = 9$s for an initial FMC of 65%. 146

5 Two dimensional contours of temperature along a xz slice located at $y = 0$ for an initial FMC of 65% for convection-only heating case at time instants (a) $t = 7$s and (b) $t = 7.5$s. 147

LIST OF TABLES

TABLE PAGE

2.1 Constitutive relations and subgrid models. The eddy viscosity is obtained from the constant coefficient Smagorinsky model, $\nu_t = (C_s\Delta)^2|\tilde{\mathbf{S}}|$ with $C_s = 0.2$ and $\Delta = \delta$. The magnitude of the strain rate is $|\tilde{\mathbf{S}}| = (2\tilde{\mathbf{S}} : \tilde{\mathbf{S}})^{1/2}$. The turbulent Schmidt and Prandtl numbers are assumed as $\mathrm{Sc}_t = 0.5$ and $\mathrm{Pr}_t = 0.5$, respectively. 24

2.2 Summary of source terms. The combustion model is based on mixing time, τ and in the radiation source term I represents the emission term based on filtered temperature of the gas or temperature of the solid fuel. The term U represents the integrated radiation intensity. A detailed description about the formulation of these terms could be found in [9]. 24

3.1 Thermophysical properties of the solid species at 25° C. 40

4.1 Initial mass fractions of solid and gas species within the solid fuel. . . 59

4.2 Kinetic data pertaining to 5-step reaction model in the solid fuel. . . 60

4.3 Thermophysical properties pertaining to 5-step reaction model in the solid fuel. 61

5.1 Initial mass fractions 91

5.2 Kinetic data pertaining to 12-step reaction model in the solid fuel. . . 93

5.3 Thermophysical properties pertaining to 12-step reaction model in the solid fuel. 94

6.1 Initial mass fractions 121

LIST OF SYMBOLS

SYMBOL	DEFINITION
ρ	density (kg/m^3)
t	time (s)
n_α	number of species
$\mathbf{u}$	velocity vector (m/s)
P	background pressure (Pa)
p	perturbation pressure (Pa)
T	temperature (K)
$\mathrm{R_u}$	universal gas constant (J/mole K)
s	source term in the gas phase
α	solid/gas phase species
$\dot{m}'''$	mass source term (kg/m^{3}s)
Y	mass fraction
J	diffusion flux of gas phase species (kg/m^{2}s)
τ	stress tensor
sgs	subgrid stress
h	sensible enthalpy (J/kg)

F	fuel species
$\sum$	summation
H_c	heat of combustion (J/kg)
W	molecular weight (kg/kmol)
ν_α	reaction stoichiometric coefficients
χ_s	fraction of consumed fuel mass converted to soot
$\hat{\mathbf{s}}$	unit vector
$\hat{\mathbf{x}}$	position vector (m)
g	gas phase within the solid fuel
s	solid phase
ϵ	emissivity
k	thermal conductivity (W/m K)
ψ	porosity
K	permeability (m^2)
D	diffusivity (m^2/s)
c_p	specific heat capacity (J/kg K)
x	distance (m)
y	distance (m)
z	distance (m)

s	solid phase
g	gas phase within the solid fuel
ν	kinematic viscosity (m^2/s)
f	formation
d	destruction
$\dot{\omega}'''$	volumetric source term (kg/m^3s)
$\dot{\mathbf{m}}''$	convective mass flux (kg/m^2s)
$\mathbf{J}_{\alpha}^{g}$	diffusion mass flux (kg/m^2s)
$\dot{Q}'''$	heat of reaction in the solid phase (W/m^3)
M_s	number of solid phase reactions
P_g	gas phase pressure within the solid fuel (Pa)
U	total radiation intensity in the gas phase (W/m^2)
∞	ambient (as in the solid-gas interface)
h_c	heat transfer coefficient (W/m^2K)
ϕ	generic scalar
X_i	x co-ordinate of the ith gas phase cell (as in FDS domain)
Y_j	y co-ordinate of the jth gas phase cell (as in FDS domain)
$\mathbf{S}$	strain rate
A	pre-exponential factor (1/s)

E	activation energy (kJ/mol)
Pr_t	turbulent Prandtl number
Sc_t	turbulent Schmidt number
ν_t	eddy viscosity (m^2/s)
C_s	smagorinsky constant
I	radiation intensity ($\mathrm{W/m^2sr}$)

Dedicated to those who sacrificed for the betterment of mankind.

Predictable is preventable.

—Gordon Graham

CHAPTER 1

INTRODUCTION

Wildfire or wildland fire is an uncontrollable fire spread through combustible vegetation, the intensity of which is governed by the fuel density, fuel physical parameters, fuel moisture content (FMC) and the external heating conditions. Fire is an important part of our planetary ecosystem with pros and cons for human lives and the environment. Wildland fires are important for various reasons such as maintaining an ecological balance for various plant species, creating a favorable habitat for some animal species, providing soil nutrition, killing diseases and insects that prey on trees, etc. [10]. At the same time wildfires can be a threat to human life and property if they occur in regions close to civilization. Over a period of 10 years, 4,649,565 acres of land was burnt by 49,403 fires. In 2012, wildfires in North America were responsible for burning more than 9 million acres of area, with 246,445 acres in the state of Colorado alone, causing tremendous loss to property and human life [11]. Recent studies indicate that changing climatic conditions, leading to global warming, are responsible for frequent occurrences of large wildfires [12]. In the past few decades, the costs involved to counter wildfires has dramatically increased to a seasonal expenditure of

about 1.7 billion dollars was spent by the governmental agencies in United States alone [13].

Wildfire may be categorized in a multitude of ways. Grishin [14] for example classifies forest fires into three broad categories depending on the physical characteristics of the fuel burnt. The first category is soil forest fires, occurring in the lowermost layer of the forest, where fuels like moss, lichen, litter, etc., are consumed. The rate at which soil fires spread is extremely slow and they are hard to detect as they do not appear on the surface. If small shrubs and the lower branches of the trees are consumed during fire propagation, then it is classified as a surface fire. A nearly uniform rate of spread is seen for the surface fires (depending on the wind velocity and vegetation properties). If the intensity of the surface fire is large, it will have great potential to start a crown fire. When top layer of the forest, consisting of the tree crowns is ignited the fire is classified as crown fire. Crown fires have highly unpredictable characteristics and usually are associated with high spread rates [15].

Wildland fires burn commonly through fuel elements such as branches and foliage. Branches are thick fuel elements made of wood and foliage are composed of cellulose, hemicellulose, lignin and water. Ignition of cellulosic and woody fuel elements has been studied extensively both experimentally and numerically using various reaction schemes. During a spreading fire, the external heat flux involves both radiation and convection as the main modes for heat transfer. When the fire is at a distance from the solid fuel, the dominant heat transfer mode is radiation and as the flame approaches closer to the fuel, convection becomes dominant, and somewhere inbetween both heating modes play an important role. The temperature

of a solid fuel increases from the heat transfer and when this reaches a critical/ignition temperature, it leads to the initiation of thermo-chemical decomposition/pyrolysis. The volatiles escape from the surface of the fuel particle, leaving a char layer behind. In the presence of oxygen, the volatiles may mix and react depending on the external heating conditions and this may result in a flame that combined with the external heat flux could further increase the rate of thermal decomposition. Ignition is the initial stage of burning which later leads to flame spread, heat release and mass loss. Ignition with a flame at the surface of a material exposed to external heating is called flaming ignition. Another mode where the solid burns without a flame is called smoldering (autoignition) or glowing ignition. A smoldering fire can evolve into flaming ignition depending on the rate of pyrolysis gases released, external heat flux, and the amount of oxygen available. As the solid fuel is heated, its temperature response also depends on the amount of moisture present within the fuel. As the fuel undergoes evaporation and pyrolysis, the water vapor is released along with the fuel vapors. This water vapor present in the gas phase also can impact ignition and the subsequent spread of the fire.

Some of the strategies for controlling fire spread include adding fuel breaks in the path of fire, creating back fires to eliminate the fuel, etc. [16]. Another approach for dealing with wildfires is to prevent their occurrence in the first place by avoiding the over accumulation of fuel. For this purpose, land management agencies use prescribed burning as a tool [17]. The area burnt during a prescribed burn was around 20 million acres nationally. In prescribed burning, fire is established under defined burning conditions to remove the accumulated fuel while minimizing the risk of starting

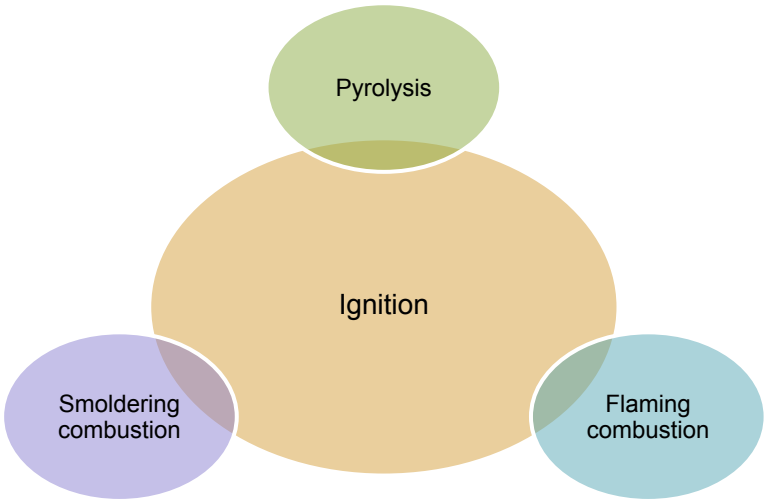

Figure 1.1: Various ignition phenomena.

large uncontrolled fires [18]. Fire control planning and resource management in this situation is a complex task which requires an understanding the fire behavior under given conditions [19]. Therefore, before carrying out prescribed burns or any kind of resource management activity associated with it, land management agencies usually use predictive wildfire models that can provide guidance on expected fire behavior under specified conditions. These predictive tools are also used to obtain data in case of an actual wildfire to plan strategies to control the fire. Data used to parameterize these models originated from experiments using dead woody material on the ground. These models [20–22] can predict fire spread rate well for the conditions under which the data were collected, however they are less accurate for other conditions when fuels are live and contain high moisture.

Section 1.1 discusses the various constituents of a forest fuel in detail followed by the effect of fuel moisture content, effects of external heating modes on fire behavior, and various wildfire modeling approaches in Sections 1.2-1.4.

1.1 Forest Fuel

Several studies have been conducted on the pyrolysis of wood in general, and its main components such cellulose, hemicellulose and lignin. Forage analysis of common forest fuel suggests that structural carbohydrates (cellulose, hemicelluloses, and lignin) account for about 30-45% of the dry mass. For example, in eight common chaparral species, the acid detergent fiber (cellulose and lignin) content of leaves and small green branches ranged from 17-33%, the neutral detergent fiber inclusive of ash (cellulose, lignin, and hemicellulose) ranged from 24-47%, and ash content ranged from 3-6%. In contrast, wood is composed of about 40-50% cellulose, 20-30% hemicelluloses, and 20-30% lignin and the nonstructural carbohydrates constitute a much smaller percentage, if present at all. Pyrolysis of such materials can roughly be described as two stages, related to primary reactions of virgin solid degradation and secondary reactions of evolved degradation products. The description of both primary and secondary reactions has been afforded mainly by lumping the pyrolysis products into a few main groups (tar, gas and char) and by means of semi-global kinetic mechanisms. Considerable scatter is observed in the reported kinetic data because of (a) the great variety of experimental techniques which give rise to different types of pyrolysis on dependence of solid and gas residence times, (b) the type of experiment (isothermal, dynamic), (c) the experimental conditions (temperature,

pressure, heating rate), (d) the physical properties of the solid (mainly moisture content and particle size) and (e) the chemical composition of the solid (contents of cellulose, hemicellulose, lignin and inorganic components). In general, kinetic studies can be classified into three main groups:

- One step global models: a one-step reaction is used to describe degradation of the solid fuel by means of experimentally measured rates of mass loss,
- One-stage, multi-reaction models: these are one-stage simplified kinetic models, consisting of several reactions describing the degradation of the solid to char and several gaseous species,
- Two-stage multi-step models: where kinetic mechanisms that describe solid degradation include both primary and secondary reactions.

The interest in modeling fire and using biomass as an energy fuel has resulted in a large body of work characterizing biomass fuels and their thermal degradation over the past 60 years [23–27]. The first kinetic models were proposed in the 1960s by Kilzer and Broido [28], Chatterjee and Conrad [29] and Shafizadeh [30], and form the basis of more recent kinetic models. Cellulose is assumed to decompose through two parallel or competitive reactions [28, 30]. Results obtained by Broido [28] and other investigators [29, 30] indicated that lower heating rates yield more char. Below approximately 280°C, it is assumed that the formation of char is favored while above this temperature, formation of tar is favored. The reason for this assumption could be due to the predominant depolymerisation reactions associated with the breakage of glycosidic bonds [31].

For high heating rates (4,000 to 10,000 °C/s), Lewellen *et al.* [32] suggested that there is no char formation and liquid tar is produced instead. Several investigators have also developed multi-step kinetic models derived from the original mechanism of Kilzer and Broido [28]. Bradbury *et al.* [33] reformulated Broido's reaction model by introducing active cellulose, as an intermediate species between native cellulose and reaction products and this reaction model is called as 'Broido–Shafizadeh model (BS)'. The 'extended Broido–Shafizadeh model' [34] was developed by Di Blasi [4] who used the BS model and extended it to include secondary reactions for tar cracking. Miller & Bellan used this extended BS model as a "skeleton" and formulated a superposed kinetic scheme for cellulose, hemicellulose and lignin kinetics.

1.2 Fuel Moisture Content

The vegetative fuel for wildland fire is typically a combination of living and dead plants. Many wildland fires burn in the elevated foliage and branches (collectively known as the plant's crown) of living vegetation. These fuel components have a variety of characteristics which influence the pyrolysis, ignition, and subsequent spread of a wildland fire [35]. Of particular importance to fire is the quantity of water contained in the fuel components. Living plants actively regulate the water contained in their plants cells while the dead components absorb and desorb water passively like a sponge [36]. These plants adapt various strategies to conserve water and the fuel moisture content (mass of water expressed as percentage of dry mass) ranges from approximately 30% to greater than 300% for some succulents. In con-

trast, the moisture content of dead fuels ranges from 5% to about 30% at saturation. Fires in live fuels can be sustained at higher moisture contents than observed for dead fuels. Moisture present within the solid fuel affects thermal decomposition and fire behavior. However, recent work suggests that moisture content changes (and hence flammability) over a growing season are also due to changes in the biomass as a result of growth and other physiological processes [37]. Jolly *et al.* [37] demonstrated that changes to dry matter exert a stronger control on seasonal live fuel moisture content dynamics than actual changes in water content, and their results challenge the assumption that the fuel moisture content variations are strongly related to water stress.

The Ignition temperature of wood has been found to increase by about 2°C for each percent increase in moisture [38]. Water has three effects on the solid phase [39]: it changes the thermal properties of the material (density, thermal conductivity, and specific heat), it transfers heat by molecular diffusion, and its evaporation is strongly endothermic. In addition to the local effects of fuel moisture on combustion and heat transfer, the vaporized moisture also contributes to the water vapor in the fire plume. When the moisture content contained in living vegetation exceeds 56%, and if combustion is complete, water vapor from vaporization exceeds the water produced by the combustion reaction [40]. In a series of numerical experiments wherein water vapor was introduced into the gas mixture of an opposed flow flame and of a diffusion flame, water vapor diluted the mixture making it more difficult to generate a flammable mixture [41].

Live fuels produce unpredictable and sometimes aggressive fire behavior that is not very well understood. These fires burn in coniferous forests in the Northern Hemisphere, eucalyptus forests in Australia, and in shrubland types such as California chaparral, Chilean mattoral, and Mediterranean maquis.

1.3 Heating Modes

The relative importance of external heat transfer mechanisms in wildland fire has been a subject of debate for several decades [42, 43]. The literature pertaining to heat transfer in wildland fire spread does not promote a single heat transfer mechanism as universally dominant. Rather, authors have suggested different mechanisms for different fire regimes, or even different mechanisms for the same regime [44]. Van Wagner [45] summarized three likely mechanisms for heat transfer in forest fires: (1) flame fuel contact, especially for wind-driven fires [46]; (2) radiation from burning fuel particles (i.e. embers), especially for crib fires [47], pine needle fires in still air [48], or other fires with low rates of advance; and (3) radiation from flames, especially for sloped beds or surface fires driven by moderate winds. Van Wagner found that his model, which exemplified mechanism 3, was descriptive of observed behavior but was inadequate to confirm the dominance of mechanism 3. Anderson [49] performed still-air experiments, in which he measured radiation heat flux through the fuel bed (i.e. mechanism 2) and from the flame (i.e. mechanism 3), and performed modeling studies to determine the role of radiant heat transfer in fire spread. Anderson found that between 15% and 40% of the heat required for fire propagation was supplied by radiation, and reasoned that the remainder was supplied by convection (i.e. mechanism 1).

Frankman *et al.* [50] concluded that at low wind speeds flame radiation dominated, with contributions from both particle radiation and gas phase conduction, and that at higher wind speeds, convection dominated, with contributions from flame radiation. Albini [51] derived a rigorous model for the radiation-dominated heat transfer case, arguing that radiation dominates for backing, no-wind and some heading fires; for other heading fires, convection could play a larger role. Rothermel [20], investigated the relative effects of convection and radiation by performing heading, no wind, and backing burns on fine fuel beds. His temperature-time plots of fuel element and gas temperatures suggest that radiation dominantly preheats fuel in no wind and backing burns, but for a heading fire at 5 mph (2.2 m/s) the fuel is significantly preheated by convection. Pagni and Peterson [52] formulated a model that included radiation, convection, and conduction heat transfer modes and compared the model output with laboratory results in pine needle fuel beds (Rothermel and Anderson [53]). In this model formulation under no-wind ambient conditions, radiation was dominant, but in wind-aided flame spread, convection was dominant.

Due to the complexity of processes that occur concurrently during a fire, the role of these two different modes of heating and the balance between them remain largely unresolved [50].

Weber [54] identified radiation heat transfer as the dominant heat transfer mode in wildland fires through a simple analytical model, and expressed the need for a short-range heat transfer mechanism for fires in still air. Dupuy [55] used experiments to verify multiple radiation driven models to determine if radiation alone can describe experimental results when it is considered as the dominant heat transfer mechanism

in flame spread. They concluded that a radiation dominant model could not account for experimental observations. Butler *et al.* [56] reported direct measurements of energy transfer in full-scale crown fires. The data suggested that radiative heating could account for the bulk of the particle heating ahead of the flaming front; however, it was indicated that immediately prior to ignition, convective heating was significant and possibly required, for ignition. Anderson *et al.* [57] reported an extensive set of wind tunnel experiments using porous beds of fine fuels wherein they focused on convective heating in advance of a spreading line fire. Their work showed that the gas temperature adjacent to a solid fuel particle remained below the solid fuel temperature until the flame was within a few centimeters of the fuel particle. Lawson and Simms [58] studied the time taken for ignition of wood when subjected to different intensities of irradiation to aid in identifying key parameters for comparison with experimental results; however, the effect of convection as a source of heat was not explored.

According to McAllister *et al.* [59] who also studied ignition of fine fuels, when thermal radiation alone was used as a heating mode, an additional pilot source was required to initiate ignition. However, according to Pickett *et al.* [8], when convective heating was used; by subjecting the fuel sample to hot gases, it led to ignition, without the aid of a pilot flame.

From literature discussed above, it appears that under high wind conditions convective heating is the dominant heat transfer mechanism however under still air conditions, radiation is the dominant heat transfer mechanism. Considering these

conditions as the two extremes, it is also likely to have a combined heat transfer mechanism where both radiation and convection contribute proportionally.

Thermal radiation from a fire front provides heat flux to unburnt fuel, leading to pyrolysis. Ignition of the pyrolyzates is then achieved by either an external source such as a spark or flame (piloted ignition) or through autoignition (sudden inflammation of a gaseous charge when exposed to a particular temperature and pressure). During convective heating, the sample is placed in a hot environment or hot gases are blown over the sample which results in pyrolysis and ignition through autoignition. In the chapter on ignition of solids (Chapter 7), Babrauskas [60] presents comprehensive theories and equations developed from first principles for ignition by thermal radiation and by convective heating; however, solving these equations requires significant computational effort. He notes that even though ignition of most solids is a gas-phase event, the details of gas-phase ignition have not been studied extensively. Engineering solutions to the theories have been devised for thermally-thick and thermally-thin materials. In the context of wildland fuels, fine fuels can be assumed to be thermally-thin implying that no temperature gradient exists within the fuel particle when heated. Most other fuels are thermally-thick with non-negligible temperature gradient within the fuel particle. It is currently unclear whether foliage and small branches < 0.63 cm diameter of live vegetation are thermally-thin or thermally-thick. McAllister *et al.* [59] who conducted piloted ignition of live fuels suggested that the foliage of shrubs and trees were thermally intermediate. Fletcher and coworkers [61] have reported that moisture was still present within a leaf when the edges of the leaf were igniting.

The ignition characteristics of foliage and small branches in live fuels subjected to different heating conditions is only poorly understood.

1.4 Wildland Fire Modeling Approaches

One of the first reports on the wildfire modeling approaches, developed during the period of 1940 to 1970, was written by Albini [62]. The models discussed in this work were mostly empirical in nature, i.e., these models aim to establish a direct relationship between physical and chemical properties of the fuel and the resulting fire behavior, such as forward spread rate, etc. According to Sullivan [63–65], an empirical model is one which is purely statistical in nature, i.e., no physical description of the phenomena involved is required to derive the model. On the other hand, a quasi-empirical model has some physical basis using which a statistical model is derived. The objective behind developing empirical or quasi-empirical models is to obtain global predictions of fire propagation, such as rate of fire spread, intensity, etc. Empirical models are derived from experimental data using techniques such as curve fitting. The model proposed by Noble *et al.* [66], for predicting fire spread rate through grassland fuels, falls under the category of empirical models. Zhou *et al.* [67] proposed an empirical model for probability of fire spread, under marginal burning conditions in chaparral like fuels, through laboratory experimentation. While conducting experiments, different fuel species with varying moisture content were considered. The effect of these variables on model formulation was accounted, but it had no physical basis. Empirical models perform satisfactorily in circumstances under which they are derived, but due to the lack of physical basis they cannot

be readily applicable to other circumstances [68]. One of the most famous quasi-empirical model widely used for fire management purposes in the United States, was proposed by Rothermel [69], based on the previous work of Frandsen [70]. This model is developed by applying the energy conservation principle to a control volume contained inside the fuel bed immediately ahead of the flame front moving in one direction. This model takes into account the heat flux required for igniting a given mass of fuel, the fraction of radiant heat flux emitted by the flame and received by the solid fuel, the effect of external wind on flame tilt, fuel moisture content of the solid fuel, intensity of reaction, etc., to calculate the fire spread rate through a homogeneous porous media. The various constants involved in the model were evaluated by conducting several series of laboratory scale experiments under varying conditions. The Rothermel model also forms the basis of the fire behavior prediction tool BEHAVE/BehavePlus, developed by Andrews [71]. The BEHAVE system, which is a collection of fire propagation models, essentially consists of two parts, the first deals with modeling of the fuels (FUEL sub-system) and the second accounts for the fire behavior (BURN sub-system). The limitations of these models are some critical assumptions made to derive the governing equations. For example, it is assumed that fire propagates through a matrix of dead fuel particles with diameters less than one-fourth of an inch, limiting the application of the model to relatively low moisture containing fuels.

Because of the simplicity of these (empirical and quasi-empirical) models and the low operational costs involved, in predicting important wildfire parameters (like rate of spread, etc.), they are still widely used for operational purposes by various

agencies across the world. But due to their inherent shortcomings, these models cannot be applied to complex problems such as blowup fires, fire spread through heterogeneous fuel beds, transition of fire from ground to crown, ignition of new fires due to transport of burning embers, generation of fire whirls, live fuel ignition etc. Physics based models, which seek numerical solutions to the governing physical equations can be applied directly to a wide variety of scenarios. Fire propagation involves many physical processes which are intricately linked to one another. The important mechanisms consists of; evaporation and decomposition of solid fuels into water vapor and pyrolysates respectively as a result of external heating, oxidation of these pyrolysis gases via gas-phase combustion, transfer of heat from gaseous flames back to unburnt solid fuel, formation of soot from both gas and solid phase combustion, turbulent flow field generation due to buoyancy effects (which further aids heat transfer), etc. Therefore to study such complicated phenomena a fully coupled solid-gas phase model which explicitly accounts for different physical processes is required.

Existing physical models can roughly be divided into three classes:

- Zero-dimensional models: A zero-dimensional simulation corresponds to a single homogeneous particle with negligible gradients of temperature (Biot number, Bi $<< 1$) and species. This is an idealized model of Thermogravimetric Analysis (TGA) experiment. In a TGA experiment, the fuel particle is exposed to a prescribed heating rate and its temperature is monitored with time. Quantities such as particle temperature, mass, and species mass fractions vary temporally, but not spatially.

- One-dimensional models: The second class of models consists of equations that are solved spatially in one-dimension. These models contain a more detailed description of the conversion process of the fuel layer. In these models, the heterogenous conversion of the fuel layer is described with devolatalization kinetics, and several reactions are included for the gas phase combustion process.

- Detailed multi-dimensional models: A third class of models use detailed two-dimensional and three-dimensional numerical simulations to completely resolve the fuel layer with grid cells much smaller than the particle size, while including various reactions for the solid phase. In the gas phase, three-dimensional transport equations are solved so that the flow dynamics and the associated combustion phenomena are described.

1.5 Motivation

In order to improve the suppression of wildfires and the prediction of prescribed fire, it is important to better understand wildland fire propagation in live fuels. Much of this previous research has been directed at developing useful empirical and semi-empirical models for operational fire prediction using data based on dead fuels. Research is needed to expand and clarify details about the fire spread process for a next-generation model. This is particularly important for fuel types that Rothermel model was not originally designed to describe, specifically live shrub fuels. Fire researchers have increasingly recognized the need to gain a more fundamental understanding including heat transfer, ignition and fuel combustion. Thus the main

objective in this dissertation is to develop better kinetic models that account for live fuel ignition behavior and to investigate:

1. How heat fluxes produced by convection and thermal radiation, individually and together, influence ignition and mass loss

2. If thermal radiation alone is sufficient, or if an additional source of heat (hot convection gases from a flame) is necessary to ignite the pyrolyzates

3. How moisture content affects the ignition of live fuel achieved via convection and/radiation heating source

1.6 Outline

Following the introduction and motivation presented in Sections 1.1-1.5, a detailed formulation of the physics based model is presented in Chapter 2. The relative effects of heating modes on pyrolysis and ignition of a woody wildland fuel is described in Chapter 3. The effect of radiation and the role of fuel moisture content on pyrolysis and combustion of a leaf-like fuel element is investigated in Chapter 4. Following these investigation, the effect of convection and moisture content is investigated in Chapter 5. The combined influence of convection and/radiation on the ignition behavior of live fuels is investigated in Chapter 6. Summary of the work, important conclusions and some recommendations for future work are proposed in Chapter 7. The Appendix contains additional figures.

CHAPTER 2

PHYSICAL MODELS

As discussed in Chapter 1, many wildland fires burn vigorously in the forest canopy that is composed of trees/shrubs. The fuels burnt include leaves and branches. The problem at hand consists of propagation of fire through a three-dimensional porous media subsequently followed by gas phase ignition. The overall burning process of a solid fuel is shown in figs. 2.1 and 2.2

As can be seen in figs. 2.1 - 2.2, to initiate burning, an external ignition mechanism is always required. The external heat supplied to the fuel, when sufficient, causes the solid fuel to undergo decomposition. As the temperature of the solid fuel starts to rise, the drying/evaporation process initiates and the moisture within the solid is converted into water vapor. With a further increase in temperature the solid fuel undergoes phase change and is converted into pyrolysis gases both locally and globally within the fuel depending on the temperature distribution. The composition of the pyrolysis gases is an extremely complex mixture of various hydrocarbons and varies for different species of solid fuel [72]. Finally, with a further rise in temperature, the solid media is converted into char, which is solid carbon. The pyrolysis gases undergo mixing with the ambient air, the process usually being turbulent, resulting

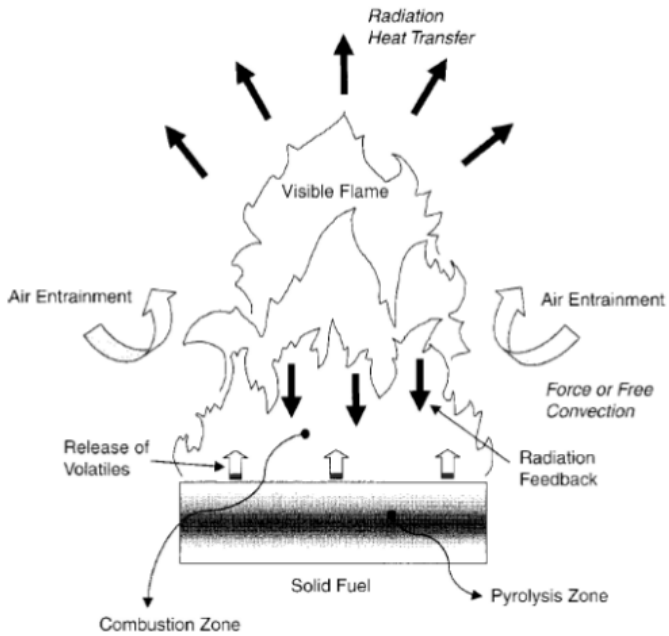

Figure 2.1: Schematic figure showing different physical phenomena during a wildfire [1].

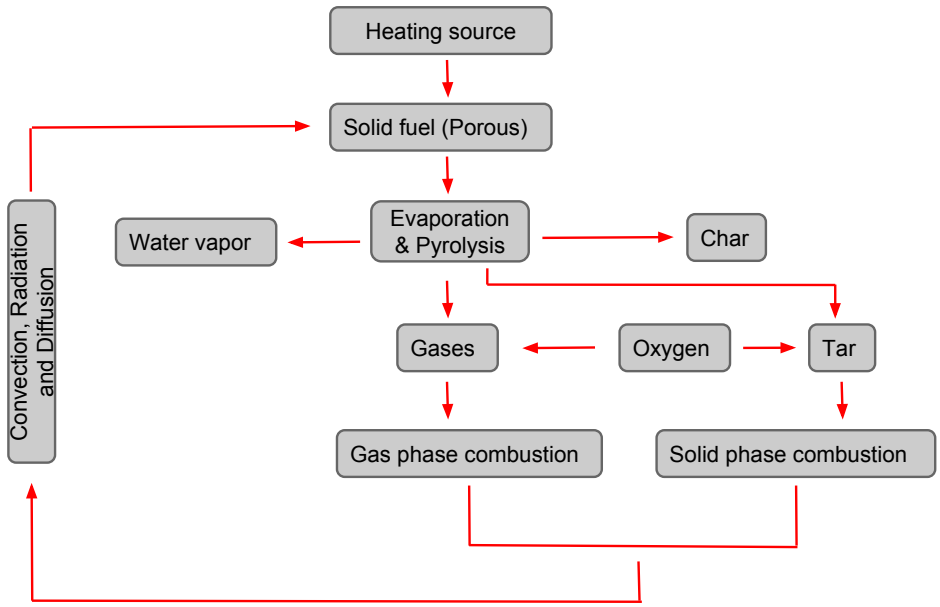

Figure 2.2: Physical processes considered during the combustion of a solid fuel.

in gas-phase combustion. Similarly, the oxidizer from the ambient directly reacts with the solid-phase, resulting in tar oxidation. The heat released from gas- and solid-phase combustion is transferred to the surrounding unburnt solid fuel through the mechanisms such as convection, radiation and conduction. This cycle will thus continue, either, till all the solid fuel is consumed or till the heat feedback mechanism to unburnt fuel is insufficient [73].

A physics based model should capture all these important mechanisms and adequately account for the coupling between them.

2.1 Governing Equations

Computational Fluid Dynamics (CFD) models such as FDS (Fire Dynamic Simulator) [9] and FireFOAM divide the surface of three-dimensional objects into multiple one-dimensional"patches"; heat is transferred only in the direction normal to the surface of a patch, but not laterally in the directions parallel to the surface [74], which is important in the present context. Therefore, to investigate the three-dimensional effects during fire initiation and propagation on fuel elements where multidimensional heat and mass transfer effects are significant, a fully coupled Gpyro3D-FDS model [74] is used. Gpyro3D (General pyrolysis) is capable of modeling thermo-chemical processes that occur in heated solids [74]. It can handle zero, one, two or three-dimensional configurations while including thermal and thermo-oxidative decomposition of condensed-phase species. Zero dimensional model represents the mass and species evolution of a lumped particle having negligible gradients of temperature and/ species as occurs in idealized thermogravimetric experiments. The solid phase

model Gpyro3D has been coupled to the gas phase (FDS), at the interface by Lautenberger [74]. A detailed description of the mathematical models used in Gpyro3D and FDS and the numerical methods adopted are given by Lautenberger [74] and McGrattan *et al.* [9], respectively. Here, an overview of the governing equations in FDS (gas phase domain) and Gpyro3D (solid phase domain) outlining the variables involved in describing the coupling between the solid and gas phase domain is presented here. Any part of the contribution made in this dissertation, existing and a new improved coupling method is developed and discussed.

2.1.1 Gas-phase Equations

Wildland fires are often associated with turbulent flow due to either air entrainment during combustion or due to winds from surrounding areas. Large eddy simulation (LES) is used to deal with turbulence in this study. Given a generic field variable $f(\mathbf{x}, t)$, which is a function of position vector $\mathbf{x}$ and time t, LES is based on spatial filtering expressed as:

$$\bar{f}(\mathbf{x}, t) = \int f(\mathbf{x}', t) G(\mathbf{x}, \mathbf{x}'; \Delta) d\mathbf{x}' \tag{2.1}$$

where overbar denotes a spatially filtered quantity. Here G is a normalized filter kernel function, with Δ denoting the filter width and the integration is performed over the spatial domain. For compressible flows, it is more convenient to work with density-weighted or Favre filtered field (denoted by tilde) defined $\tilde{f}(\mathbf{x}, t) = \overline{\rho f}/\bar{\rho}$.

The filtered equations of FDS that account for source terms pertaining to solid fuel thermal degradation are presented below followed by formulations for combustion chemistry, thermal radiation and convective heat transfer. Further details of the gas phase equations, including the numerical approach, discretization and boundary condition implementation can be found in [9]. The Favre-filtered transport equations for mass, species, momentum and enthalpy, combined with the equation of state (EOS), shown below in Eqs (2.2-2.6), provide $n_\alpha + 5$ independent equations (n_α is the number of species) for $n_\alpha + 5$ unknowns: density, $n_\alpha - 1$ mass fractions, 3 velocity components, hydrodynamic pressure, and enthalpy.

$$\frac{\partial \bar{\rho}}{\partial t} + \nabla \cdot (\bar{\rho}\tilde{\mathbf{u}}) = \overline{\dot{m}_{\mathrm{s}}'''} \tag{2.2}$$

$$\frac{\partial \bar{\rho}\tilde{Y}_\alpha}{\partial t} + \nabla \cdot \left(\bar{\rho}\tilde{\mathbf{u}}\tilde{Y}_\alpha\right) = -\nabla \cdot \left(\bar{\mathbf{J}}_\alpha + \mathbf{J}_\alpha^{\mathrm{sgs}}\right) + \overline{\dot{m}_\alpha'''} + \overline{\dot{m}_{\mathrm{s}\alpha}'''} \tag{2.3}$$

$$\frac{\partial \bar{\rho}\tilde{\mathbf{u}}}{\partial t} + \nabla \cdot (\bar{\rho}\tilde{\mathbf{u}}\tilde{\mathbf{u}}) = -\nabla\tilde{p} - \nabla \cdot (\bar{\boldsymbol{\tau}} + \boldsymbol{\tau}^{\mathrm{sgs}}) + \bar{\rho}\mathbf{g} + \overline{\dot{m}_{\mathrm{s}}'''}\tilde{\mathbf{u}}_{\mathrm{s}} \tag{2.4}$$

$$\frac{\partial \bar{\rho}\tilde{h}}{\partial t} + \nabla.(\bar{\rho}\tilde{\mathbf{u}}\tilde{h}) = \frac{D\bar{P}}{Dt} - \nabla \cdot (\bar{\mathbf{q}} + \mathbf{q}^{\mathrm{sgs}} + \bar{\mathbf{q}}_{\mathrm{d}}) + \overline{\dot{q}'''} - \overline{\dot{q}_{\mathrm{s}}'''} - \overline{\dot{q}_{\mathrm{r}}'''} \tag{2.5}$$

$$\bar{P} = \bar{\rho}\mathrm{R_u}\tilde{T}\sum_{\alpha=1}^{n_\alpha}\frac{\tilde{Y}_\alpha}{W_\alpha} \tag{2.6}$$

In equations (2.2-2.6), $\bar{\rho}$ is the filtered gas mixture density, $\tilde{\mathbf{u}}$ denotes the Favre-filtered velocity vector, $\bar{P}$ is the background pressure, $\tilde{p}$ is the perturbation pressure, $\tilde{T}$ is the filtered gas phase temperature, and $\mathrm{R_u}$ is the universal gas constant. In the mass conservation equation (2.2), $\overline{\dot{m}_{\mathrm{s}}'''}$ is the term that accounts for water vapor as a result of evaporation and fuel vapor during pyrolysis. In the filtered species conservation equation (2.3), $\tilde{Y}_\alpha$ is the mass fraction of the gas-phase species α, $\overline{\dot{m}_\alpha'''}$ is the chemical source term due to combustion, $\overline{\dot{m}_{\mathrm{s}\alpha}'''}$ is a combined term due to evaporation and pyrolysis $\overline{\dot{m}_{\mathrm{s}}'''} = \sum \overline{\dot{m}_{\mathrm{s}\alpha}'''}$, and $\bar{\mathbf{J}}_\alpha$ and $\mathbf{J}_\alpha^{\mathrm{sgs}}$ represent the molecular species diffusion flux and subgrid-scale (SGS) species diffusion flux, respectively. The terms that account for pyrolysis are only valid at the solid-gas phase interface. In the momentum equation (2.4), $\bar{\boldsymbol{\tau}}$ and $\boldsymbol{\tau}^{\mathrm{sgs}}$ represent viscous and SGS stress tensors, respectively, and $\overline{\dot{m}_{\mathrm{s}}'''}\tilde{\mathbf{u}}_{\mathrm{s}}$ is the term accounting for the effects of pyrolysis. In the energy equation (2.5), $\tilde{h}$ is the sensible enthalpy of the gas mixture, $\bar{\mathbf{q}}$, $\mathbf{q}^{\mathrm{sgs}}$ represent the conductive heat flux and the SGS conductive heat flux, respectively, $\overline{\dot{q}'''}$ denotes the source term due to heat release during combustion, $\overline{\dot{q}_{\mathrm{s}}'''}$ represent the heat absorbed by the solid fuel due to radiation and convection from the gas phase and $\nabla \cdot \overline{\mathbf{q}}_d$ represents the net radiative and the diffusive flux in the gas phase. All the formulations pertaining to flux and source terms are given in Tables 2.1 and 2.2 respectively.

FDS employs a staggered arrangement where in the scalars are present at cell centers and velocity components are at their respective face centers. It is second-order accurate in both space and time. To ensure boundedness of the scalar fields, FDS employs second-order total variation diminishing (TVD) transport schemes and the default flux limiter is the Superbee scheme. Equations (2.2-2.5) are solved using

Table 2.1: Constitutive relations and subgrid models. The eddy viscosity is obtained from the constant coefficient Smagorinsky model, $\nu_t = (C_s\Delta)^2|\tilde{\mathbf{S}}|$ with $C_s = 0.2$ and $\Delta = \delta$. The magnitude of the strain rate is $|\tilde{\mathbf{S}}| = (2\tilde{\mathbf{S}} : \tilde{\mathbf{S}})^{1/2}$. The turbulent Schmidt and Prandtl numbers are assumed as $\mathrm{Sc}_t = 0.5$ and $\mathrm{Pr}_t = 0.5$, respectively.

Species flux	$\left(\bar{\mathbf{J}}_\alpha + \mathbf{J}_\alpha^{\mathrm{sgs}}\right) = -\bar{\rho}(\tilde{D}_\alpha + \frac{\nu_t}{\mathrm{Sc_t}})\nabla\tilde{Y}_\alpha$
Momentum flux	$\bar{\boldsymbol{\tau}} = -2\tilde{\mu}\left(\tilde{\mathbf{S}} - \frac{1}{3}(\nabla\cdot\tilde{\mathbf{u}})\mathbf{I}\right)$
	$\boldsymbol{\tau}^{\mathrm{sgs,d}} \equiv \boldsymbol{\tau}^{\mathrm{sgs}} - \frac{1}{3}\mathrm{trace}\left(\boldsymbol{\tau}^{\mathrm{sgs}}\right)$
	$= -2\bar{\rho}\tilde{\nu_t}\left(\tilde{\mathbf{S}} - \frac{1}{3}(\nabla\cdot\tilde{\mathbf{u}})\mathbf{I}\right)$
Heat flux	$(\bar{\mathbf{q}} + \mathbf{q}^{\mathrm{sgs}}) = -(\tilde{k} + \bar{\rho}\tilde{c}_p\frac{\nu_t}{\mathrm{Pr_t}})\nabla\tilde{T}$

Table 2.2: Summary of source terms. The combustion model is based on mixing time, τ and in the radiation source term I represents the emission term based on filtered temperature of the gas or temperature of the solid fuel. The term U represents the integrated radiation intensity. A detailed description about the formulation of these terms could be found in [9].

Mass source term	$\overline{\dot{m}_{\mathrm{s}}'''} = \sum_\alpha \overline{\dot{m}_{\mathrm{s}\alpha}'''}$
Chemical source term	$\overline{\dot{m}_F'''} = -\frac{\min(\bar{\rho}\tilde{Y}_F, \bar{\rho}\tilde{Y}_{o_2}r_{o_2})}{\tau}$
	$\tau = C_{\mathrm{EDC}}\frac{\triangle^2\mathrm{Sc_t}}{\nu_t}, \quad C_{\mathrm{EDC}} = 0.1$
Radiation and diffusion source terms	$\overline{\mathbf{q}}_{\mathrm{d}} = -\sum_\alpha \bar{\rho}D_\alpha\tilde{h}_\alpha\nabla\tilde{Y}_\alpha$
	$\overline{\dot{q}_{\mathrm{r}}'''} = \kappa[4\pi I_b(\tilde{T}) - \overline{U}]$
	$\overline{\dot{q}_{\mathrm{s}}'''} = \overline{\dot{q}_{s,\mathrm{rad}}'''} + \overline{\dot{q}_{s,\mathrm{conv}}'''}$
	$\overline{\dot{q}_{s,\mathrm{rad}}'''} = \bar{\epsilon}\left[4\pi I_b(T_s) - \overline{U}\right]$
	$\overline{\dot{q}_{s,\mathrm{conv}}'''} = h_c(\tilde{T} - T_s)$

a Predictor-Corrector method. First the thermodynamic variables $\bar{\rho}$, $\tilde{Y}_\alpha$ and $\bar{P}$ are computed, followed by calculation of velocity divergence in the predictor step which is then used as a constraint to solve the Poisson equation for the hydrodynamic pressure in the correction step.

2.1.1.1 Chemical Reactions

The molar heat of combustion for a given chemical reaction at constant pressure is [75], [76],

$$\Delta H_c = -\sum_{\alpha} \nu_\alpha h_\alpha(T) W_\alpha \tag{2.7}$$

where ν_α, h_α, W_α are the stiochiometric coefficient, total enthalpy and molecular weight of the gas species α respectively.

The heat release rate (HRR) per unit volume of the combustion process can be represented in terms of heat of combustion,

$$\overline{\dot{q}'''} = -\overline{\dot{m}_F'''} \Delta \tilde{h}_c \tag{2.8}$$

where $\Delta \tilde{h}_c = \Delta H_c / W_F$ is the mass-based heat of combustion evaluated at $\tilde{T}$. The filtered chemical source term for fuel, $\overline{\dot{m}_F'''}$ is obtained from Eddy Dissipation Concept (EDC) [77], see Table 2.2.

2.1.1.2 Thermal Radiation Transport

The net contribution from thermal radiation in the energy equation of the gas phase is given by the radiation transport equation (RTE):

$$\hat{\mathbf{s}} \cdot \nabla \bar{I}(\mathbf{x}, \hat{\mathbf{s}}) = \kappa [I_b(\tilde{T}) - \bar{I}(\mathbf{x}, \hat{\mathbf{s}})] \tag{2.9}$$

where $\mathbf{x}$, $\mathbf{s}$ is a vector in spacial and angular direction, $I(\mathbf{x})$ is the radiation intensity, $I_b(\tilde{T})$ is the emission source term evaluated using the filtered temperature field $\tilde{T}$ [9]

and $\kappa(\mathbf{x})$ is the absorption coefficient. The absorption coefficients are obtained for various species during the chemical reaction and soot using a narrow-band model called RadCal [78]. Here we have invoked the grey gas assumption, which is appropriate for fires from vegetative fuels [79]. Soot evolution model is not used, instead the mass of soot generated is based on an assumed fraction, χ_s, of the mass of fuel gas consumed by the combustion reaction. The value assumed for χ_s is 0.01 based on data available for Douglas fir ranging from less than 0.01 to 0.025 under flaming conditions [80]. The radiation equation is solved in the spacial direction using a finite volume method based on Raithby and Chui [81] and in the angular direction it is discretized over solid angles. The finite volume solver requires about 20% of the total CPU time of a calculation, a modest cost given the complexity of radiation heat transfer. The number of solid angles used here was 104. Integrating the RTE (2.9) over all the solid angles gives the equation for conservation of radiant energy.

$$\overline{\dot{q}_{\mathrm{r}}'''}(\mathbf{x}) = \kappa[4\pi I_b(\tilde{T}) - \overline{U}(\mathbf{x})] \tag{2.10}$$

where $\bar{U}$ is the integrated radiation intensity. T.

2.1.1.3 Convective Heat Transfer

In the LES calculation, convective heat flux to the surface of the solid fuel is obtained from a combination of natural and forced convection correlations

$$h = \left[C|T_g - T_s|^{\frac{1}{3}}, \frac{k_g}{L}(0.0037)\mathrm{Re}^{\frac{4}{5}}\mathrm{Pr}^{\frac{1}{3}}\right] \quad \mathrm{W/m^2K} \tag{2.11}$$

where C is the coefficient for natural convection (1.52 for a horizontally oriented solid fuel) [82], L is a characteristic length related to the size of the solid fuel used, k_g is the thermal conductivity of the gas, and the Reynolds Re and Prandtl Pr numbers are based on the gas flowing past the obstruction. The convective heat flux calculation is based on the formulation given in Table 2.2.

2.1.2 Solid-phase Equations

The three-dimensional porous media conservation equations for mass, species, momentum and energy in Gpyro3D, the solid fuel model, are presented below in Eq (2.12-2.17). The following assumptions are inherent to this model:

- Each solid phase species α has well-defined properties that are temperature dependent: bulk density (ρ_α), specific heat capacity ($c_{p\alpha}$), effective thermal conductivity (k_α), emissivity (ϵ_α), permeability (K_α), porosity (ψ_α).
- Radiation heat transfer across pores is not accounted and only surface absorption of radiation is considered.
- All gaseous species within the solid fuel have equal diffusion coefficient, D (independent of temperature).
- Darcian pressure-driven flow through porous media (Stokes flow).
- Unity Schmidt number, hence $\nu = D$.
- Gas phase and solid phase are in thermal equilibrium ($T_g = T_s$).
- No shrinkage or swelling (volume change) occurs.

$$\frac{\partial \rho_s}{\partial t} = -\dot{\omega}'''_{fg}, \tag{2.12}$$

$$\frac{\partial \rho_s Y_\alpha^s}{\partial t} = \dot{\omega}'''_{fs\alpha} - \dot{\omega}'''_{ds\alpha}, \tag{2.13}$$

$$\frac{\partial (\rho_s h_s)}{\partial t} = -\nabla \cdot \mathbf{q}_s - \dot{Q}'''_{s-g} + \sum_{\alpha=1}^{M_s} (\dot{\omega}'''_{fs\alpha} - \dot{\omega}'''_{ds\alpha}) h_\alpha \tag{2.14}$$

$$\frac{\partial \rho_g \psi}{\partial t} + \nabla \cdot \dot{\mathbf{m}}'' = \dot{\omega}'''_{fg} \tag{2.15}$$

$$\frac{\partial \rho_g \psi Y_\alpha^g}{\partial t} + \nabla \cdot (Y_\alpha^g \dot{\mathbf{m}}'') = -\nabla \cdot \mathbf{J}_\alpha^g + \dot{\omega}'''_{fg\alpha} - \dot{\omega}'''_{dg\alpha} \tag{2.16}$$

where

$$\mathbf{q}_s = -k \nabla T_s, \quad \dot{\mathbf{m}}'' = -\frac{K}{\nu} \nabla P_g, \quad \mathbf{J}_\alpha^g = -\psi \rho_g D \nabla Y_\alpha. \tag{2.17}$$

The solid phase mass, species and energy conservation are given in Eqs (2.12-2.14). Similarly mass, and species conservation for the gas phase present within the solid fuel are presented in Eqs (2.15-2.16). In these equations, ρ_s, h_s, ψ, K, k denotes weighted quantities i.e. $k = \sum X_\alpha k_\alpha$. Subscripts s, g, α, f, d denote solid phase, gas phase within the solid fuel, solid/gas-phase species within the solid fuel, formation and destruction, respectively. Eq. (2.15) of the mass conservation of gas species is not explicitly solved, but it is used to form a pressure evolution equation through the ideal gas law for the gas phase density ρ_g and Darcy's law for the convective mass flux

$\dot{\mathbf{m}}''$ as shown in Eq. (2.17). The diffusion coefficient D in Eq. (2.17) is calculated from Chapman-Enskog theory [83]. In Eq. (2.17), ν is the kinematic viscosity of gas species. The term $\dot{\omega}'''$ represents volumetric source term for formation or destruction of species and $\dot{Q}'''$ represents the volumetric source term for heat generated or absorbed during any reaction. The details on the formulations of the source terms are given in [74].

When discretized, the above equations yield a system of coupled algebraic equations that are solved numerically. Due to the nonlinearity introduced by the source terms and temperature-dependent thermophysical properties, a fully-implicit formulation is adopted for the solution of all equations. The condensed phase energy conservation equation, gas phase species conservation equation, and gas phase momentum conservation equation are solved using the Tridiagonal Matrix Algorithm [84]. The solid fuel mass and species conservation equations are solved with a customized fully implicit solver that uses relaxation to prevent divergence [85].

Initially, the solid-phase domain in Gpyro3D consists of the solid phase species and the gas phase species in general is standard air including nitrogen and oxygen. The initial temperature and ambient pressure are 300 K and 101.3 kPa, respectively. Gpyro3D (solid fuel domain) is coupled to FDS (gas phase domain) by obtaining the temperature, total radiation intensity, species mass fractions and convective heat transfer coefficient from FDS, which are applied as boundary conditions to the solid phase. The following equation is used as the boundary condition for the solid phase energy equation (2.14):

$$-k\nabla T_s = \bar{\epsilon}\overline{U} - \bar{\epsilon}\sigma T_s^4 - h_c(T_s - \tilde{T}_\infty) \tag{2.18}$$

where quantities h_c, $\tilde{T}_\infty$, $\overline{U}$ that represent heat transfer coefficient, ambient fluid temperature, and total radiation intensity are obtained from the gas phase domain (FDS domain) external to the solid fuel. No boundary conditions are needed for the mass or solid phase species conservation equations since there are no convective or diffusive terms in Eqs (2.12) and (2.13). The gas phase species conservation equation (2.16) requires a boundary condition where the diffusive mass flux of gaseous species into or out of the decomposing solid following:

$$\bar{\psi}\rho_g D \nabla Y_\alpha^g = \frac{h_c}{c_{pg}}(\tilde{Y}_\alpha^\infty - Y_\alpha^g) \tag{2.19}$$

where $\tilde{Y}_\alpha^\infty$ represents the ambient mass fraction of the species α given by FDS.

In the existing coupling method [74], a solid fuel cell in Gpyro3D at the interface communicates with the closest gas phase cell in the FDS domain. This communication is schematically shown in fig. 2.3. In this figure, filled circles represent the centers of FDS cells shown by rectangles with dark lines. Open circles represent the centers of Gpyro3D cells shown by gray lines. Here, ϕ is a generic variable, e.g., a particular species, of the FDS domain. During coupling at the solid-gas interface, all the solid phase cells attain the same value irrespective of their location with respect to the gas phase cell center above. Following this there are large gradients between the solid cells which results in a low order accurate solution within the solid fuel. This limitation is circumvented by implementing a bilinear interpolation scheme at the solid-gas interface

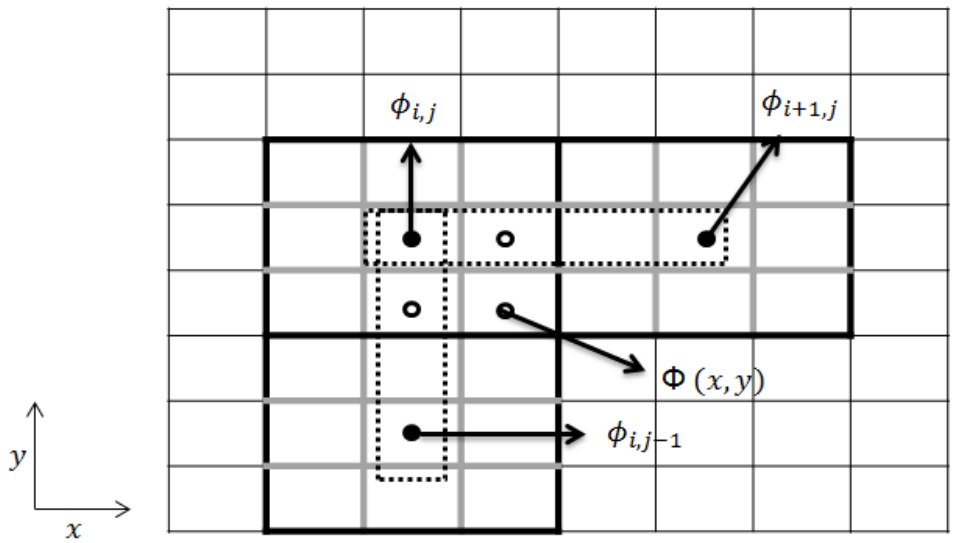

Figure 2.3: Schematic represeing bilinear interpolation used to couple the solid-fuel domain solver variables to gas phase solver variables. FDS and Gpyro3D cells are shown by dark and gray solid lines respectively.

Indices i and j represent the cell index of the FDS cell in x and y directions, respectively. Consider Φ to represent the interpolated value of the same variable in Gpyro3D. The bilinear interpolation scheme employed at the interface of solid fuel and surrounding gas phase is:

$$\Phi(x, y) = \phi_{i,j} + \frac{\phi_{i,j} - \phi_{i+1,j}}{x_i - x_{i+1}}(x_i - x) + \frac{\phi_{i,j} - \phi_{i,j-1}}{y_j - y_{j-1}}(y_j - y). \tag{2.20}$$

The above interpolation scheme was utilized at all interfaces of the solid-fuel and gas-phase domains. After the needed variables are passed from FDS to Gpyro3D, the solution is advanced for one time step for the solid-fuel domain. The obtained temperature, convective heat flux, species, and species mass fluxes at the interface

are then communicated from Gpyro3D to FDS. Then the FDS solver is advanced in time for one time step.

CHAPTER 3

AN INVESTIGATION OF THE INFLUENCE OF HEATING MODES ON IGNITION AND PYROLYSIS OF A SLAB OF WOOD

3.1 Introduction

Wildland fires burn commonly through fuel elements such as branches and foliages. Branches are thick fuel elements made of wood and the key ignition criteria identified for woody materials are surface ignition temperature, and critical mass flux of volatiles [86]. Critical mass flux is defined as the amount of pyrolysis gases that must be generated for a diffusion flame to be established above the surface of the solid fuel. The temperature at which wood decomposition is initiated is referred to as the critical temperature [58], [87] and the time taken for it to reach this temperature is referred to as the critical time. Examining the ignition behavior of woody wildland fuel under different heating conditions would help in determining the effective mode of heating that could result in ignition, and this can later be extended to investigate its effects on fire intensity and spread rate. The prediction of glowing/flaming ignition of solid fuels is also necessary in many fire safety applications, and from this viewpoint, it is also important to understand the ignition behavior of a woody material in order to predict the ignition delay and burn rate in the case of a fire.

A number of previous publications have focused on critical time [88–93], heating mode [50, 94–96] and mass loss rate [3, 86, 92, 97, 98]. Many of these studies were on pyrolysis and/or combustion models with an ignition criterion that utilized a critical surface temperature as the ignition temperature [3, 88, 89, 97]. According to Babrauskas [93], the critical ignition temperature for wood varied from 210 to 497 ^{o}C mostly for piloted ignition, and from 220 to 510 ^{o}C for autoignition. Such a wide variation might be due to differences in the definition of ignition temperature, design of the test apparatus, operating conditions such as moisture content, orientation of fuel, and the type of species of wood [50].

The relative importance of external heating modes in wildland fire has been long debated [99], [100]. Due to the complexity of processes that occur concurrently during a fire, the role of these two different modes of heating and the balance between them remain largely misunderstood [50]. Heating of unburnt vegetation ahead of a fire front involves both convection from the flame contact and radiation; however, both modes of heating are transient and vary in magnitude as wind gusts (hot gases) and intensity of burning of the vegetation might increase, increasing the overall magnitude of convection and radiation heat transfer respectively. Most of the research reported to date considered the influence of constant external heat flux on ignition time, MLR and charring rate, without explicitly focusing on differences due to modes of heating and their time varying nature [90], [101], [102]. The main goal here is to investigate the role of different magnitudes of radiation and convection as sources of heating of a slab of woody fuel by observing their influence on critical time, MLR and charring rate. Furthermore, the balance and effective role played by each mode is analyzed.

In the present work, first, a case wherein wood is considered an inert thermally thick substance is studied in a one-dimensional configuration. This is done in order to gain insight into the rate of change in surface temperature when the slab is subjected to time dependent radiative and convective heat source. Surface temperature response is one of the important criteria used for ignition and if this shows any variation in its response to heating mode and heating rate, it could imply that the thermal degradation and associated chemical activity following ignition may be directly influenced by this variation. In the second stage, the woody fuel slab is treated as a thermally thick, chemically active medium, and its detailed response to heating by different modes via examination of MLR, critical time, and charring rate is presented. The other side of the one-dimensional slab is insulated to serve as a symmetry boundary condition [96].

3.2 Physical Configuration

In a spreading wildland fire, unburnt vegetation that lies ahead of burning and burnt vegetation is exposed to varying magnitudes of convective and radiative heating. The physical model considered here is designed to focus on this situation. Although, idealized, the choice of this configuration involving a one-dimensional slab of woody material with fixed thickness is motivated in part by the simplicity it affords and its similarity to experimental configurations studied by McAllister *et al.* [59, 98]. This configuration enables a computational investigation of critical time, MLR and spread rate under the influence of different modes of heating. Gpyro, a one-dimensional version of Gpyro3D discussed in detail in Chapter 2, is utilized to solve the governing

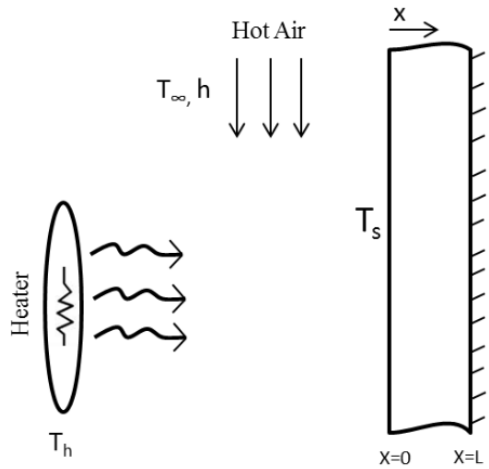

Figure 3.1: Schematic diagram of the physical configuration. A one dimensional slab of woody fuel of width L is subject to heating by either convection (hot air), radiation (heater), or mixed mode heat transfer.

unsteady equations. First, Gpyro is utilized to solve the one-dimensional chemically inert preheating problem outlined in Section 3.2.1. Second, it is used to solve the same configuration while taking into account the thermal decomposition of the chemically active media as presented in Section 3.2.2. A schematic of the physical domain along with the boundary conditions is shown in Fig. 3.1.

The woody fuel slab is considered dry and thermally thick with a thickness L. Related work has shown that the presence of water vapor can significantly alter ignition flame characteristics ([41]); however, this additional complicating factor is not included in the present setup. It is exposed to radiative and convective heating on one side ($x = 0$) and insulated on the other side of the domain ($x = L$). Here, T_∞ is the reference ambient air temperature for convective heating of the fuel slab, and likewise T_h is the source or heater temperature responsible for radiative heating,

and T_s is the time-varying surface temperature at $x = 0$. The symbol T_{source} denotes the relevant heating mode source temperature, T_∞ or T_h . In order to model the wind effects, a convective heat transfer coefficient of h is considered. The domain is initially at a uniform temperature $T_0 = 27^o$C. Since we use critical temperature as the ignition criteria, the time at which surface temperature reaches this value $T_{\text{cr}} = 370^o$C [93], [97], is referred here as critical time and is denoted by t_{cr}. It is noted that in this work, we are not dealing with flaming ignition for which the use of critical fuel mass flux is arguably a better criterion [103], [98]. Our focus is to investigate ignition, regarded as the initiation of pyrolysis, which occurs prior to flaming combustion. Here, it is noted that previous research that used the critical mass flux, as an ignition criterion for flaming ignition, and suggested values for this flux, are limited to cases where ignition is due to a pilot source. The need for a pilot source to cause flaming combustion in the context of wildfires is still an active area of research since wildfires could also be a result of autoignition of fuel vapors.

3.2.1 Chemically Inactive Media

Here the analysis is carried out, considering the woody fuel slab to be chemically inactive, focusing on the initial preheating stage. It is assumed that the thermophysical properties of wood are constant and no chemical decomposition takes place before the surface attains the critical temperature. The governing equation is

$$\rho c_p \frac{\partial T}{\partial t} = k \frac{\partial^2 T}{\partial x^2} \tag{3.1}$$

where T is temperature, t is time, and x is the one-dimensional spatial coordinate. In Eq. 3.1, ρ, c_p , and k are the density, heat capacity and thermal conductivity. The boundary conditions are

$$-k\frac{\partial T}{\partial x}\Big|_{x=0} = h(T_\infty - T_s) + \sigma\epsilon(T_h^4 - T_s^4) \tag{3.2}$$

$$\frac{\partial T}{\partial x}\Big|_{x=L} = 0 \tag{3.3}$$

and the initial condition is $T(x,0) = T_0$. Here σ is the Stefan-Boltzmann constant, h is the heat transfer coefficient and ϵ is the emissivity. Convective heating mode is investigated by eliminating the radiation contribution on the right hand side of Eq. 3.2. Likewise, radiation heating mode is investigated by eliminating the convective contribution in Eq. 3.2. Finally, combined or mixed mode heating is studied by including both terms. Dimensionless temperature, position, and time are defined as $\theta = \frac{T}{T_0}$, $\epsilon = \frac{x}{L}$, and $\tau = \frac{\alpha t}{L^2}$, respectively. Also, Bi $= \frac{hL}{k}$ is the Biot number, and R $= \frac{\sigma\epsilon T_o^3 L}{k}$ is a dimensionless number that characterizes external radiation [95]. Thus, θ_∞ and θ_h denote the dimensionless source temperatures associated with the mode of heating, convective and radiative respectively, and the dimensionless time taken for the surface temperature to reach critical temperature $\theta_{\mathrm{s-cr}}$ is τ_{cr} . Lastly θ_{source} denotes the dimensionless heating mode source temperature θ_∞ or θ_h.

3.2.2 Chemically Active Media

The model outlined in Section 3.2.1 is extended so that the one-dimensional fuel slab of woody material shown schematically in fig. 3.1 is presumed to be both thermally thick and chemically active. Wood is modeled as consisting of two condensed phase species (wood and char) coupled to one gas phase species (pyrolysate). The ambient gas phase external to the decomposing woody fuel slab contributes only to convective heating. Thus any reference to the gas phase, as far as the chemical reactions are concerned, pertains to the gases inside the pores or voids that form within decomposing wood. A single-stage, heterogeneous reaction kinetic scheme considered by Lautenberger & Fernandez-Pello [3] is used to model fuel decomposition in an anaerobic environment:

$$\text{Dry wood (s)} \longrightarrow \text{Char (s)} + \text{Pyrolysate (g)}$$

The model used by Lautenberger & Fernandez-Pello [3] is primarily based on wood and can be applied in the context of wildfires since it has been formulated using natural fuel, white (softwood) pine. Also, the value 40 kW/m^2, used by them for heat flux is typical of wildland fires. The kinetic parameters, were obtained by Lautenberger & Fernandez-Pello [3] through applying genetic algorithm optimization on the experimental data of Ohlemiller *et al.* [2]. The reaction given above is a reduced version of the two-step model employed by Lautenberger & Fernandez-Pello [3]. Their first-step reaction is for conversion of moist wood to dry wood while their second-step reaction is for conversion of dry wood to char. In the current work, we have used only

their second-step reaction as we only consider dry wood. This reaction is endothermic and the thermophysical properties of wood and char are shown in Table 3.1.

Table 3.1: Thermophysical properties of the solid species at 25° C.

Properties	Wood	Char
Density (ρ)	400 kg/m^3	0.0725 kg/m^3
Thermal conductivity (k)	0.2 W/mK	0.065 W/mK
Specific heat (c_p)	1200 J/kgK	1216 J/kgK
Thermal diffusivity (α)	4.1 $\times 10^{-7}$ m^2/s	7.32 $\times 10^{-7}$ m^2/s

The values used for activation energy, pre-exponential factor and heat of reaction are 135 (kJ/mol), 3.29 $\times 10^9$ (s^{-1}) and 5.33 $\times 10^5$ (J/kg) respectively [3]. This model although simple, can be used to address the initial preheating stage during thermal breakdown of wood. To support this claim, a comparison between our simulation results obtained using this one-step reaction, experimental results of Ohlemiller *et al.* [2] and numerical results of Lautenberger & Fernandez-Pello [3] is shown in fig. 3.2. The computational setup used for this case is similar to Ohlemiller *et al.* [2] and consists of a one-dimensional slab of white pine irradiated with 40 kW/m^2 on one side and convectively cooled on the other. The heat transfer coefficient and the dimension of the slab used are 10 W/mK and 3.8 cm respectively [3].

As seen in in fig. 3.2, temperatures obtained in the current study match reasonably well with the temperatures obtained by Ohlemiller *et al.* [2] and Lautenberger & Fernandez-Pello [3]. This match confirms that the effect of drying phase reaction on temperature response is small and hence can be neglected.

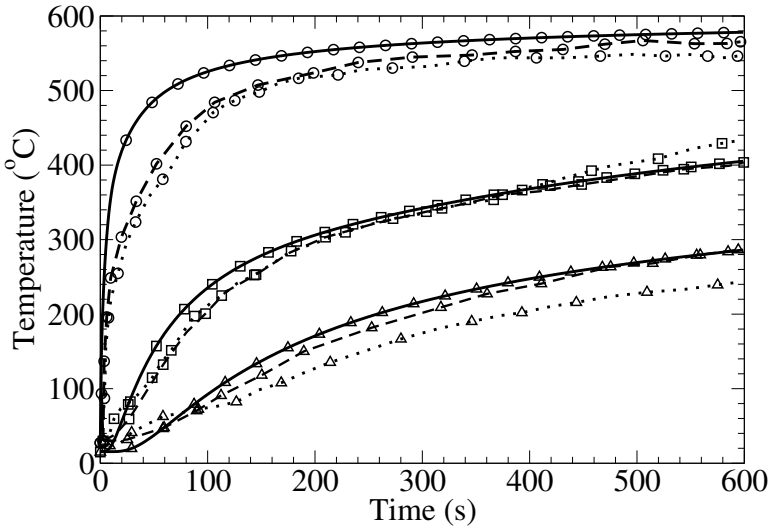

Figure 3.2: Time history of temperatures at depths 0 mm (circle symbol), 5 mm (square symbol), and 10 mm (triangular symbol) from the surface of white pine irradiated at 40 kW/m^2 in nitrogen atmospheres in the configuration studied experimentally (dotted line) by Ohlemiller *et al.* [2], computationally with a two-step reaction (dashed line) by Lautenberger & Fernandez-Pello [3], and computationally with a single-step reaction in the present study (solid line).

3.3 Results and Discussions

The chemically inactive problem formulated in section 3.2.1 has an infinite series solution in the case of convective mode heating [104]. This case was used to validate the computational method adopted here. The computed solution for a number of input parameters considered, shown in 3.3, matched the analytical solution satisfactorily at various time instants.

Figures 3.4 (a, b) display the dependence of the critical time as a function of the source temperature associated with the selected mode of heating and the total delivered energy to the slab over the course of the critical time for these situations. In all cases, for a chosen θ_{source}, the initial surface heat flux for the two heating modes are

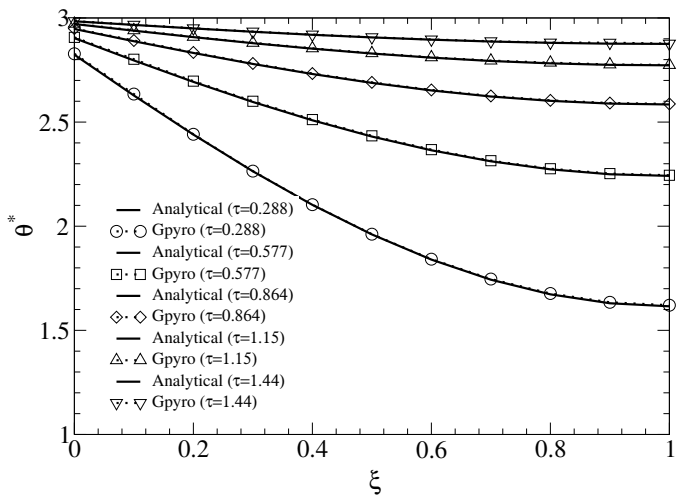

Figure 3.3: Comparison of spatial variation of non-dimensional temperature between Gpyro and available analytical solution at various time instants.

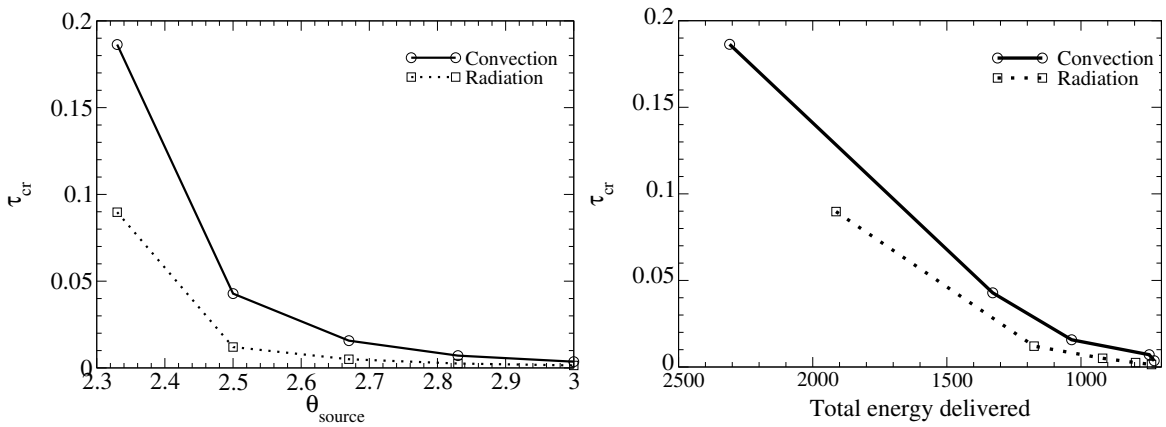

(a) (b)

Figure 3.4: Critical time against (a) heating source temperature (θ_{source} represents θ_h and θ_∞ in radiation and convection heating, respectively), and (b) total energy delivered in chemically inert media.

matched. The total energy delivered to the slab to raise the surface temperature to the critical temperature obtained as $\int_0^{\tau_{\text{cr}}} \left.\frac{\partial\theta}{\partial\epsilon}\right|_{\epsilon=0} d\tau$ is computed via a simple quadrature.

From fig. 3.4(a) it is evident that the critical time decreases with increasing source temperature for both modes of heating, as expected. This decrease is more than

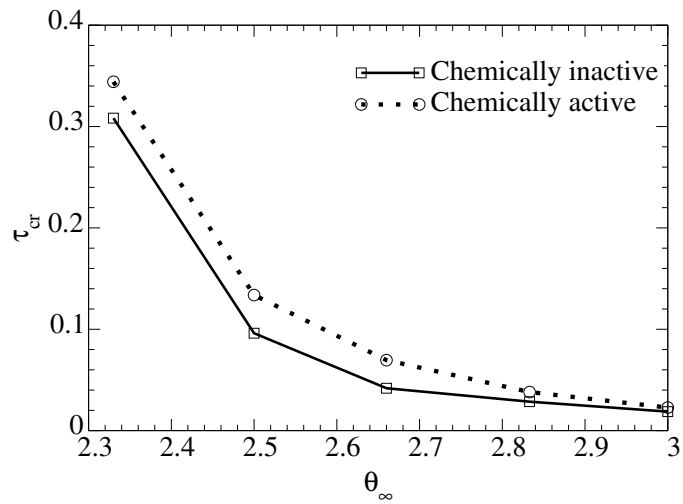

Figure 3.5: The dependence of critical time on source temperature for convective mode of heating, Bi = 7.6.

an order of magnitude for the range $\theta_{\text{source}} = 2.3$ to 3.0 (corresponding to T_{source} of 690 to 900K). For a fixed value of the source temperature, the critical time for radiation mode heating is substantially smaller than for convection, especially for smaller source temperatures. The variation of the critical time against the total delivered energy is displayed in fig. 3.4(b). From figs. 3.4(a) and 3.4(b), it is observed that higher source temperatures require less amount of total energy delivered to the slab over the critical time period. Higher heating rates are attained at higher temperatures; therefore, at higher heating rates, the material heats faster resulting in lower critical times. The inference here is that the heating process in case of radiative boundary condition (BC) is faster than that in case of convective BC. Also, the total amount of energy delivered until the temperature reaches the critical temperature in case of radiative BC is less than that in convective BC. The dependence of the critical time as a function of the source temperature $\theta_{\text{source}} = \theta_\infty$ under convective mode heating is

shown in fig. 3.5 for both active and inert media. Although the trends of the curves for both media are similar, the difference between them is somewhat significant. The chemically inactive approximation for the pure convection cases considered here considerably under predicts the chemically active results. A single-stage model for breakdown of wood was considered here since it was found that the critical time was affected only due to preliminary endothermic reactions concerning the preheating of wood and it remains unaffected due to any other secondary exothermic reactions such as char oxidation and gas phase reactions. Results discussed in the remainder of this section focuses on a detailed parametric study of a chemically active media when it is subjected to different modes of heating. We examine convective and mixed mode heating process at constant θ_h and Bi, and subsequently study radiation and mixed mode heating process at constant θ_∞. This approach helps in comparing different cases systematically, thereby providing a complete understanding of the entire problem.

In the case of chemically active media, the dependence of critical time on θ_∞ is displayed in fig. 3.6 for various Bi numbers. In fig. 3.6(a), the heating mode is only convection whereas in fig. 3.6(b), it is mixed mode heating. The radiative heat source temperature is $\theta_h = 3$ in all cases studied in fig. 3.6(b). As seen in fig. 3.6(a), the critical time reduces as the convective fluid temperature increases. Higher temperature leads to higher convective heat flux, and hence results in lower critical times. The effect of heat transfer coefficient has been also investigated here by considering various Bi numbers. Higher Bi numbers used here is similar to the situation wherein the wood is subjected to high wind speed [95, 105–107]. From figs

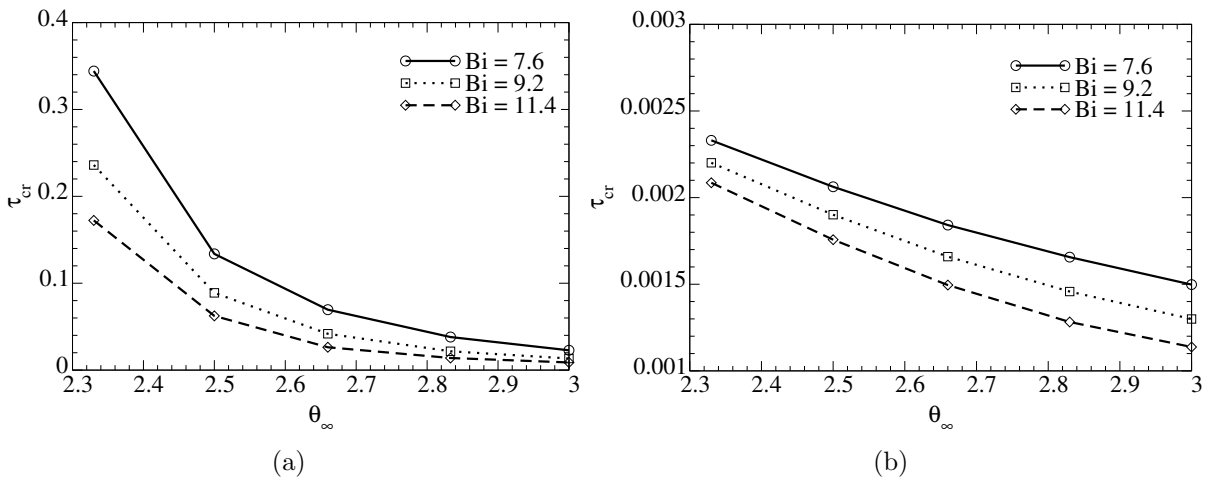

Figure 3.6: Critical time against convective source temperature for different Biot numbers under (a) convective mode of heating; and (b) combined convective and radiative mode of heating with $\theta_h = 3$.

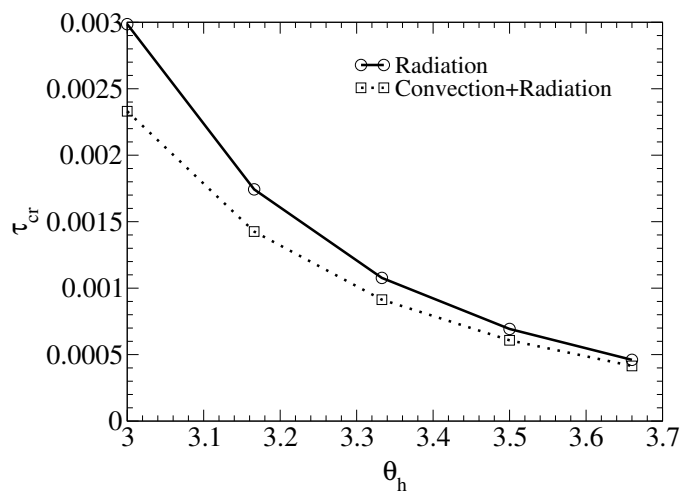

Figure 3.7: Critical time against heater temperature in radiative mode of heating and combined radiative and convective mode of heating with $\theta_\infty = 2.33$ and Bi = 7.6.

3.6 a-b, it is evident that larger the Bi number, smaller is the critical time for both convective and mixed mode heating. A comparison of these figures reveals that the addition of radiation mode to the convection mode of heating, results in a reduction in critical time by an order of magnitude in the cases considered.

Shown in fig. 3.7 is the critical time versus the radiative heating source temperature (θ_h). The range of temperature used here is chosen based on reported temperatures in wildfires [108]. It is seen that when θ_h is decreased from 3.7 to 3 the critical time increases six fold from around 5×10^{-4} to 3×10^{-3}. The addition of convection heating to radiative heating results in the decrease of the critical time. This decrease is around 20% at $\theta_h = 3$ while it is not as significant at larger values of $\theta_h = 3.66$.

Inclusion of chemical degradation of wood subject to convective, radiative, and mixed mode heating allows us to also examine the temporal evolution of MLR. MLR is a global parameter that measures the rate of thermal degradation of the material in the entire domain. The MLR is obtained by the calculating the total formation rate of pyrolysate from the condensed/solid phase [3].

The time evolution of MLR for different convection source temperatures and various Bi numbers under convective and combined modes of heating are shown in fig. 3.8. The MLR starts with a zero value at τ=0 in all cases, increases to reach a maximum value and then slowly decreases in almost all cases shown. The entire process occurs much faster for cases with combined convective and radiative heating. The reason for the initial increase of the MLR is the increase in reaction rates, which in turn is attributed to the initial increase of temperature. On the other hand, the decrease of MLR, after reaching a maximum, is due to the decrease of the mass of reactants. The MLR peak values are much larger for these cases, compared to the ones in which heating mode is only convection. The ratio of the peak MLR in the case of mixed mode heating to the peak MLR in the convective mode ranges from

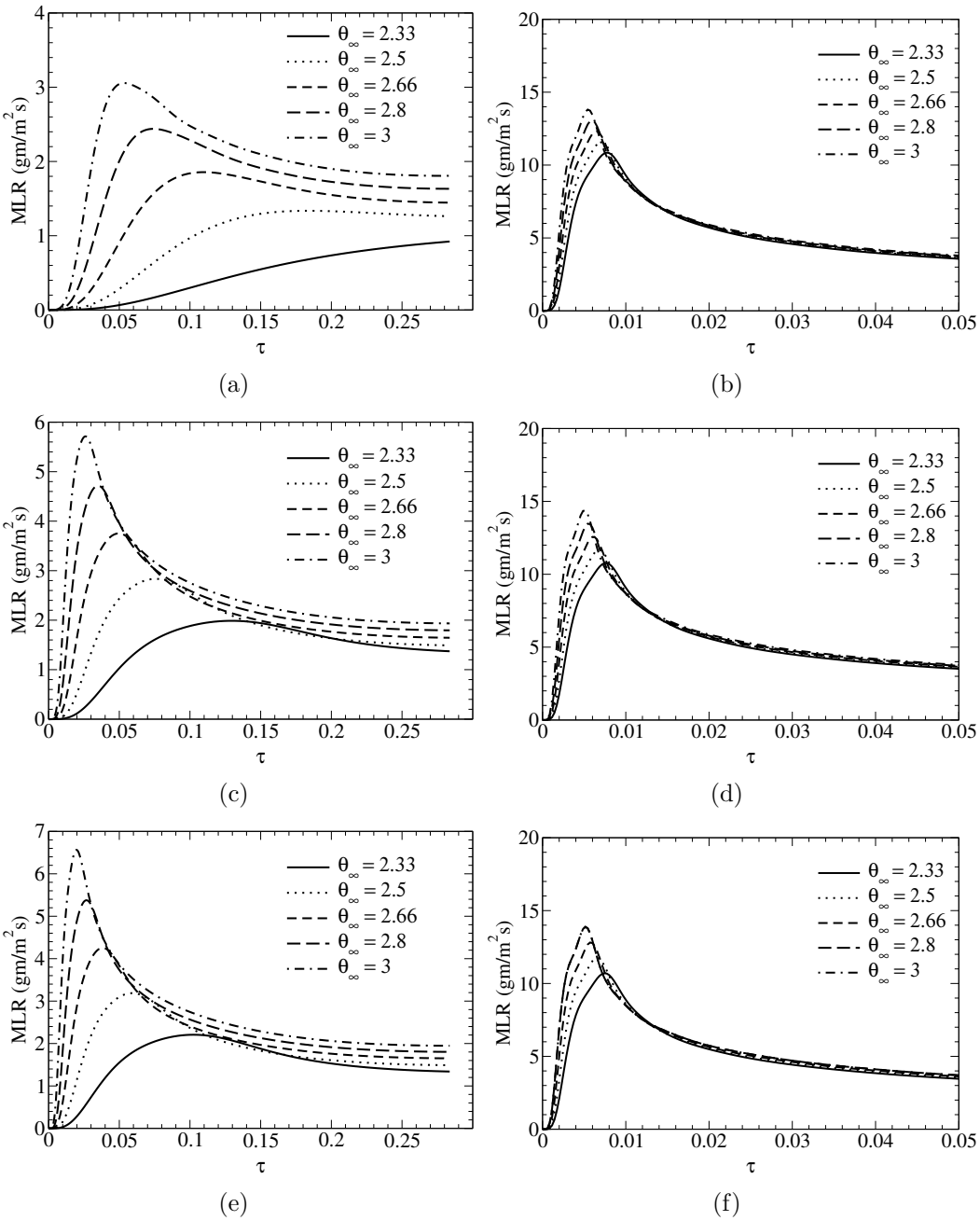

Figure 3.8: Time evolution of mass loss rate in g/m^2/s for convective mode of heating (left column) and combined convective and radiative mode of heating with $\theta_h = 3$ (right column); (a, b) Bi = 7.6; (c, d) Bi = 9.2; and (e, f) Bi = 11.4.

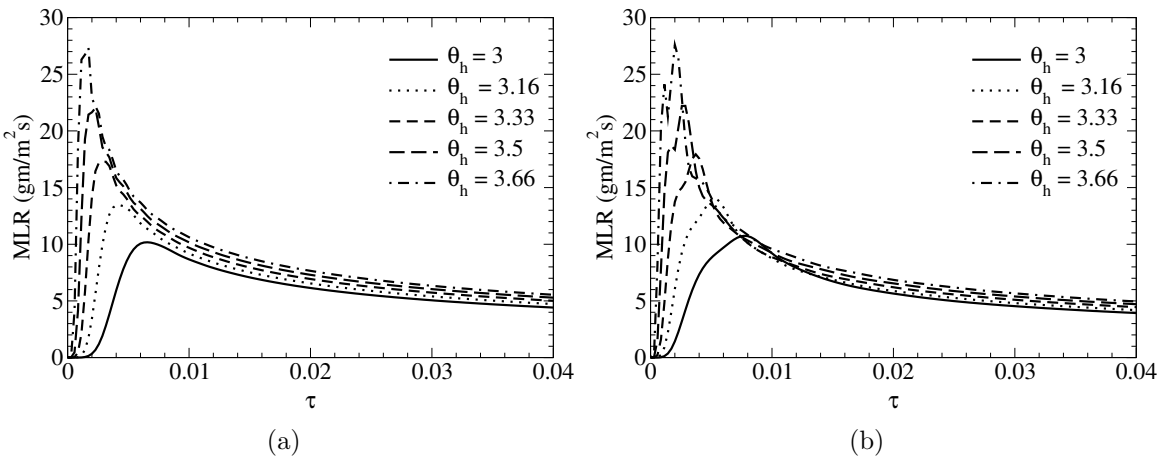

Figure 3.9: Time evolution of the mass loss rate under (a) radiative mode of heating; (b) combined radiative and convective mode of heating with θ_∞ =2.33 and Bi = 7.6.

about 4.6 for Bi = 7.6 to about 2.1 for Bi = 11.4. It is seen in fig. 3.8 that the influence of the change of the Bi number on how MLR evolves, is minimal for cases where convective heating is combined with radiative heating; however, as can be seen, this influence is significant under convective mode heating. The overall effect of the increase of θ_∞ is to increase the maximum of the MLR and to shift the time of its occurrence to an earlier time in all cases. In cases where radiative heating is present, a short while after the MLR has peaked, not much of difference is observed between the time evolutions of MLR curves labeled by different values of θ_∞. This observation shows that the MLR evolution is not sensitive to the variation of Bi in these cases, suggesting that convective heating is suppressed by the radiative heating after an initial stage ($\tau > 0.01$). On the other hand, the MLR is very sensitive to the variation of both Bi and θ_∞ when the only mechanism responsible for heating is convection. The MLR values are larger at higher Bi.

The time evolution of the MLR is shown for various radiative heating source temperatures θ_h in fig. 3.9. With an increase of θ_h from 3 to 3.66, it is seen that the peak MLR increases from around 10 to above 25 g/m^{2}s. A power regression ($y = Ax^B$) for this peak value against θ_h reveals that the peak MLR is correlated with $\theta_h^{4.94}$ in the radiative mode of heating (fig. 3.9a) and with $\theta_h^{4.70}$ in a combined mode of heating (fig. 3.9b). It is noted that the radiative heat flux is correlated with θ_h^4 when the heating source temperature is much larger than the surface temperature. A comparison between a typical curve of a constant θ_∞ in fig. 3.9(a) and its counterpart in fig. 3.9(b) reveals that the addition of the convection mode to the radiation mode increases the MLR only slightly. This increase is obviously attributed to the fact that the overall energy transferred to the solid fuel is more in fig. 3.9(b) compared to that in fig. 3.9(a). Yet, the addition of the convection mode seems to have other effects including the widening of the peak of MLR and the shift in its time of occurrence to earlier times.

The charring rate is a quantity that provides an insight into the char formation rate and its dependence on external heating. Char formation is a result of thermal degradation of the material [109]. Here, charring rate for a computational cell is computed by

$$\text{charring rate} = \frac{x_{0.9}^{i} - x_{0.9}^{i+1}}{t_{0.9}^{i} - t_{0.9}^{i+1}} \tag{3.4}$$

where i and $i+1$ denote adjacent cell numbers, $x_{0.9}^{i}$ and $x_{0.9}^{i+1}$ are the x coordinates of the cell centers in dimensional terms, and $t_{0.9}^{i}$ and $t_{0.9}^{i+1}$ denote the moments at which the char mass fractions of cells i and $i+1$ exceed 0.9. Figure 3.10 shows the

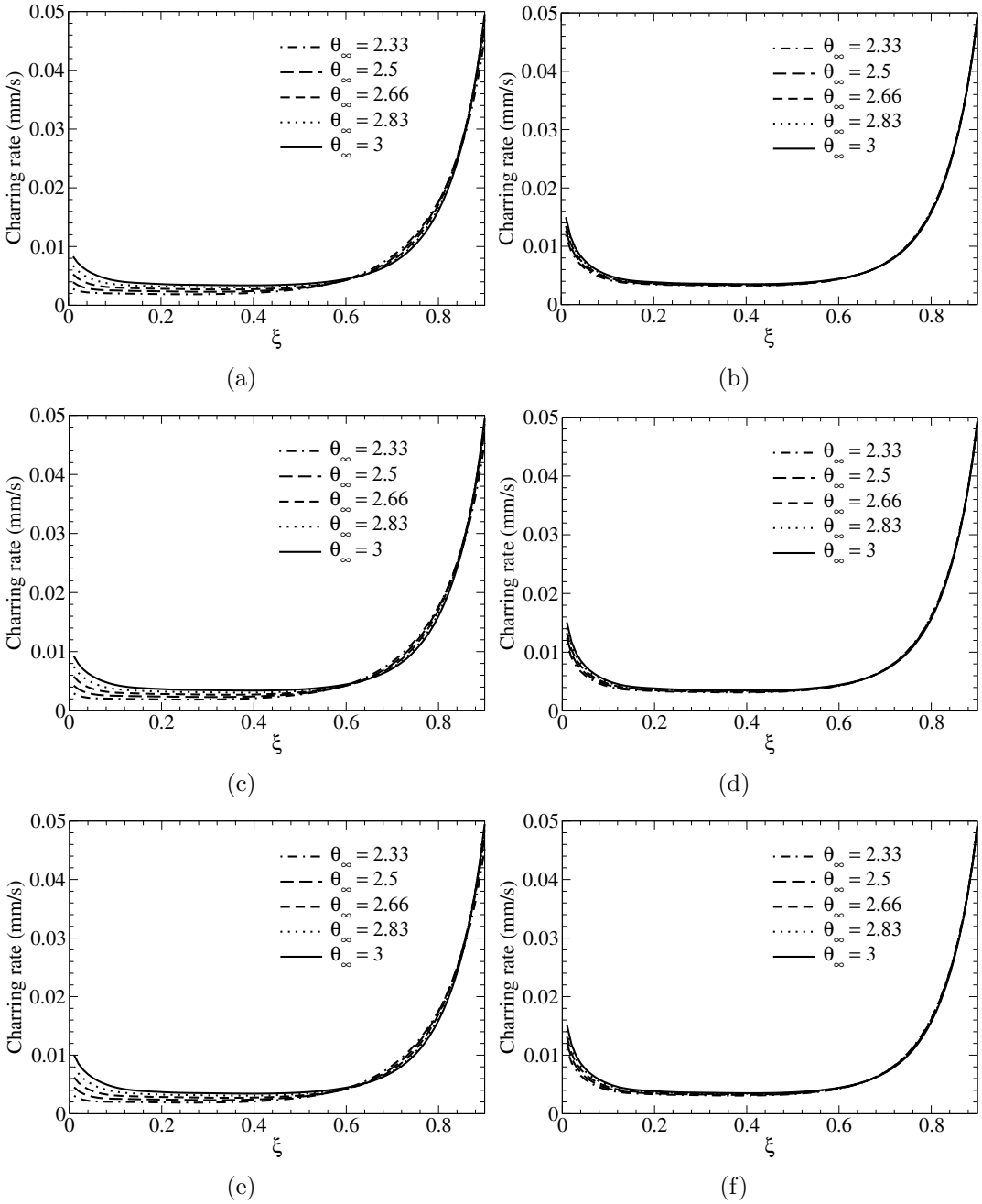

Figure 3.10: Charring rate in mm/s plotted as a function of dimensionless position, ξ in convective mode of heating (left column) and combined convective and radiative mode of heating with $\theta_h = 3$ (right column) for (a, b) Bi = 7.6; (c, d) Bi = 9.2; and (e, f) Bi = 11.4.

charring rate versus position. In all cases, the charring rate starts from around 0.01 mm/s at ξ=0, then decreases slightly and reaches a plateau that extends from around ξ=0.1 to around ξ=0.6. Then it starts increasing until it reaches about 0.05 mm/s at ξ=1.0. Starting values of the charring rate are somewhat smaller for smaller values of ξ in pure convection cases. As seen in the right panels, the variation of θ_∞ in cases where there is radiative heating in addition to convection has little influence on the behavior of the charring rate. The variation of Bi number does not seem to have much influence either on the behavior of the charring rate. The charring rate starts out high because the region close to the left boundary is closer to the heating source and its temperature increases early in time. On other hand, the heating rate in the midsection of the slab is smaller and because of that, charring rates are smaller in this region. The charring rate starts out high initially as a result of higher heating rate due to proximity of this region to the heating source. As the char layer thickens, the heat transfer rate into the unreacted wood slows down [109] and this explains the lower charring rate observed in the midsection. The increase in charring rate towards the end of the domain could be a result of low heat transfer in the regions closer to the right boundary, which is an insulated boundary condition.

The charring rate is plotted against ξ in fig. 3.11 for different values of θ_h. The trends of the curves in this figure are similar to the ones shown in fig. 3.10. However, the initial behavior of the charring rate, seen in fig. 3.11, is highly dependent on θ_h: The charring rate at the range between $0< \xi <0.2$ is substantially smaller for smaller values of θ_h. On the other hand for $\xi >0.6$, the difference between the charring rates at different values of θ_h is insignificant. Comparing the charring rate values in fig.

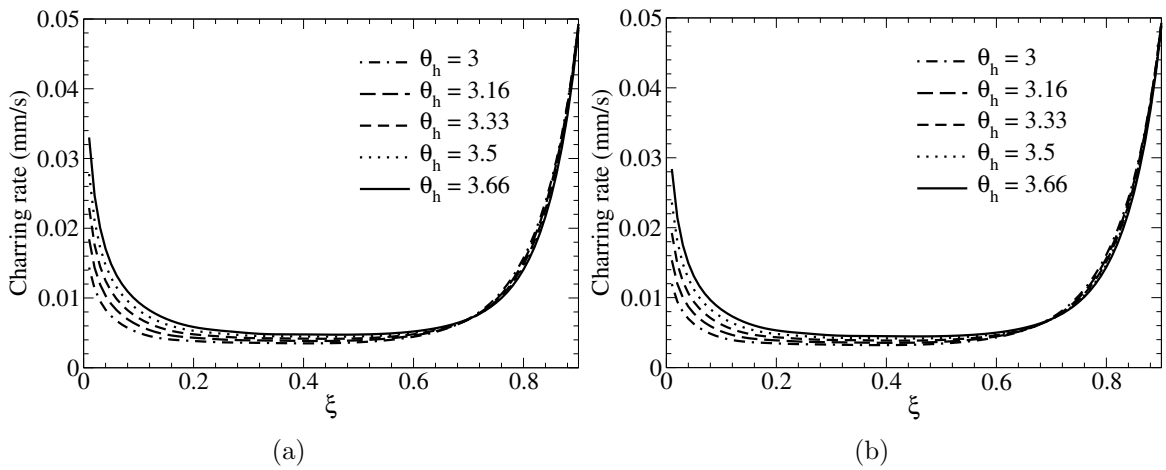

Figure 3.11: Charring rate in mm/s versus dimensionless position ξ under (a) radiative mode of heating; (b) combined radiative and convective mode of heating with $\theta_\infty = 2.33$ and Bi = 7.6.

3.11(a) to the ones in fig. 3.11(b) reveals that the addition of the convective mode to the radiation mode of heating results in a small reduction in charring rate.

3.4 Chapter Summary

Numerical investigation of the influence of convective, radiative, and mixed mode heating on critical time, mass loss rate and charring rate was carried out for a slab of wood using Gpyro. A one-step model approximation for wood degradation was validated initially with experimental results of Ohlemiller et al. [2] and numerical results of Lautenberger & Fernandez-Pello [3]. The increase in convective source temperature by 7% and Bi number by 17% reduces the critical time by 15% and 8%, respectively, in combined convective and radiative heating. The increase in radiation source temperature by 5% during mixed mode of heating in the presence of a constant convective source results in the decrease of critical times by 35%. These cases clearly

indicate the balance between the two modes of heating during the preheating period of wood in a wildfire scenario. In order to study the effects of heating once ignition takes place, MLR and charring rate were extensively investigated. As the MLR is a global quantity, it shows marginal variation during the mixed mode heating when the convective temperature and Biot numbers were increased by 7% and 17%, respectively. In the case of charring rate, during mixed mode heating the charring rate is independent of heating rate used and is identical at all convective source temperatures and is also insensitive to changes in Bi number. However, it is found that the time advancements of MLR and charring rate experience negligible changes when a convection mode is added to the radiation mode.

CHAPTER 4

HORIZONTAL FUEL CONFIGURATION: INFLUENCE OF MOISTURE CONTENT AND RADIATIVE HEAT TRANSFER

4.1 Introduction

In the previous Chapter, the study was carried out for a thick woody fuel element while neglecting the effect of moisture content. Moreover, the model used for the fuel decomposition was a simple one-step mechanism, and the ignition criterion was based solely on the surface temperature of the solid fuel since a detailed behavior of external gas phase was not included in the modeling. High intensity fires are more common in smaller fuel elements such as foliage. Furthermore, some of the important issues concerning the ignition of smaller fuel elements are: 1) effect of radiation on ignition, 2) effect of moisture content on solid- and gas-phase ignition. In order to investigate these issues, the effect of gas phase combustion processes should also be included in the modeling, which is done in the current chapter for a thin leaf-like fuel element.

Many wildland fires burn in the elevated foliage and branches of living vegetation. The chemical composition of the living fuel is substantially different from the wood. Hemicellulose, cellulose, lignin and moisture are the main constituents of

a biomass fuel, respectively [35, 110, 111] with cellulose as the main component [110]. There are various kinetic mechanisms available in the literature to model cellulose decomposition as reviewed in Chapter 1. In this work, the 'extended Broido–Shafizadeh model' [34], is used to model the thermal degradation of cellulose.

Water/moisture present in vegetation is an important factor that influences the burning behavior of live fuels [112]. The flammability of vegetation for example has been associated with its moisture content. In addition to water contained within living plants, water is also a product of pyrolysis and combustion reaction [113]. When the moisture content exceeds 56% in an idealized fuel, the amount of water released by evaporation exceeds the amount produced by combustion [114]. Most living vegetation will burn at fuel moisture content well in excess 56%.

According to McAllister *et al.* [59], when thermal radiation alone was used as a heating mode, an additional pilot source was required to initiate ignition. They also reported significant temperature and moisture gradients inside the solid during pyrolysis of live foliar fuels, which was assumed thermally thin. Pickett *et al.* [8] reported that when convective heating was applied through subjecting the fuel sample to hot gases, it led to ignition without the aid of a pilot flame. On the other hand, they observed that when radiation with an initial heat flux of 50 kW/m^2 was used as the heating source, no ignition was observed. This observation was confirmed through preliminary numerical investigation in the current study when a thermal radiation flux of similar magnitude was applied. As reviewed in detail in Chapter 1, there appears to be some consensus that radiative heat transfer likely plays a major role in ignition and fire spread in fires propagating in still air conditions. Furthermore,

under low-wind conditions, there is considerable literature that suggests radiation as the dominant heating mode. Pickett *et al.* [8].

Experiments to date in the published literature [8,59,115] have been successful in describing the burning characteristics of individual live leaf samples. Specifically, temperatures at which moisture is released, the dependency of ignition time on the species FMC and burnout times were characterized. [8] also reported that ignition did not occur at the end of global evaporation, as predicted by operational/conventional models, but possibly at the end of local evaporation. They found that at the time of ignition, a significant amount of moisture (30–60%) remained in the sample for most species they investigated. Their experiments did not investigate pyrolysis and other physical processes inside the fuel.

In spite of these recent developments in characterizing the burning of live fuel fuels, there is a dearth of information on how the constituents of the live fuel species are structurally and chemically different from other species [116] and even less information on how moisture is distributed within them. To the best of our knowledge, behavior of moisture in the context of wood has been well established but in the context of live fuels, more investigation is required in order to accurately model the physical system. Considering such a limitation, our investigation focuses on main components such as cellulose and water, based on available literature of wood in order to facilitate computational modeling of an individual leaf-like fuel element.

The main aim of the work discussed in this chapter is to better understand the effects of thermal radiation and moisture content on pyrolysis of a leaf-like fuel composed of cellulose and the subsequent gas phase ignition. This is accomplished

by taking into account multi-step thermophysical processes occurring in the solid fuel and the associated combustion of the released gases using a three-dimensional solid-gas coupled model. The solid model used Gpyro3D [74] for pyrolysis and the gas phase fluid dynamics and combustion were solved by Fire Dynamics Simulator (FDS) [9, 117]. The development and validation of this model is the first step in our effort to model the pyrolysis and ignition of live vegetation and compare the results to data from the FIST apparatus and a flat-flame burner with a radiant panel [59,115]. It is noted that in this chapter, a criterion different from that described in the previous chapter is used for identifying the ignition. Here it is based on the gas phase. A single value of heat release rate, as a reasonable criterion for ignition, has been proposed [118, 119]. In this study ignition time is defined as the time at which the HRR exceeds 200 kW/m^3 in the gas phase. HRR above this critical value would represent an active flame over the solid fuel.

4.2 Physical Configuration

The radiant heat fluxes associated with crown fires can be as high as 200 kW/m^2 [**?**]. Following this, the heat flux used in the present case was close to 225 kW/m^2. A fuel element ($0.04 \times 0.04 \times 0.002$ m, Length $\times$ Width $\times$ Thickness along x, y, z coordinate) of cellulose simulated the leaves studied by Pickett *et al.* [8] and Gallacher *et al.* [115]. The top surface of the solid fuel was located at $z = 0.032$ m with $y = 0$ representing the leaf center line. Point A, a location in the domain within the fuel at which various quantities were graphed, was located at $x = -0.02$, $y = 0$, and

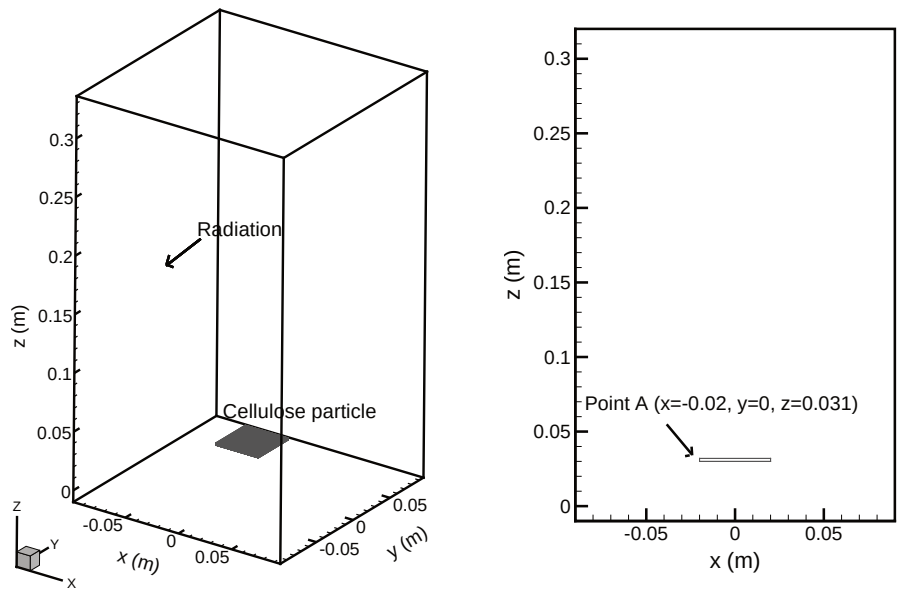

(a) (b)

Figure 4.1: (a) Isometric view of computational domain showing thin cellulose particle subjected to radiative heating from surface at x = -0.09 m and (b) two-dimensional view of computational domain along the xz-slice at $y = 0$. Point A located at x = -0.02 m, $y = 0$, $z = 0.031$ m is considered for analysis.

$z = 0.031$. A schematic of the physical domain along with the boundary conditions is shown in fig. 4.1.

The computational domain used for the gas-phase solver FDS, was a rectangular cube of size $0.18 \times 0.18 \times 0.32$ m ($x \times y \times z$). The grid resolution in the gas phase was $72 \times 72 \times 92$, respectively. The solid fuel particle was centered in the gas-phase domain and located at $z = 0.03$ m in the computational domain. The solid fuel element was simulated by Gpyro3D with a grid spacing of $0.0008 \times 0.0008 \times 0.0003$ m resulting in 13824 grid cells. The fuel element was exposed to a radiant surface on one side located at x = -0.09 m and all the other sides had open boundary conditions. The radiating surface was maintained at a constant temperature of 1500 K. Initially, the

solid-phase domain in Gpyro3D consists of the solid phase species including moisture and cellulose, and the gas phase species including nitrogen and oxygen with initial mass fractions given in Table 4.1. The initial temperature, moisture content, pressure, gaseous species mass fractions, and condensed phase species were set uniform throughout the solid. All computations were performed using Message Passing Interface (MPI) with 36 processors of Dense Memory Cluster (DMC) located at Alabama Supercomputer Authority. A typical simulation of 30 seconds required a wall time of 72 hours and 64 GB of memory.

Table 4.1: Initial mass fractions of solid and gas species within the solid fuel.

FMC	Moisture	Cellulose	N_2	O_2
80%	0.46	0.54	0.77	0.23
40%	0.22	0.78	0.77	0.23
5%	0.04	0.96	0.77	0.23

4.2.1 Chemical Reactions

The chemical reactions included in the solid phase to model pyrolysis are as follows:

$$\text{Moisture (s)} \longrightarrow \text{Water vapor (g)} \tag{R1}$$

$$\text{Cellulose (s)} \longrightarrow \text{Active cellulose (s)} \tag{R2}$$

$$\text{Active cellulose (s)} \longrightarrow \text{Char (s)} + \text{Fuel vapors (g)} \tag{R3}$$

$$\text{Active cellulose (s)} \longrightarrow \text{Tar (g)} \tag{R4}$$

$$\text{Tar (g)} + \text{O}_2\text{ (g)} \longrightarrow \text{Fuel vapors (g)} \tag{R5}$$

Reactions R2-R4 suggested by Bradbury et al. [33] are primary reactions and R5 [4] is a secondary reaction that collectively model pyrolysis of cellulose. The primary reactions are modeled with the breakdown of cellulose to lower molecular weight gases while the secondary oxidation reaction, is concerned with the tar breakdown to low molecular weight gases. In the current study, reaction R1 and the thermophysical properties pertaining to it are included to investigate the effects of FMC [120]. For reactions R2-R5, they are adopted from [4]. The kinetic parameters and thermophysical properties for the above set of equations are given in Table 4.2, 4.3 respectively.

Table 4.2: Kinetic data pertaining to 5-step reaction model in the solid fuel.

Reaction	A (s^{-1})	E (kJ/mol)	Δh (kJ/kg)
R1	5.13×10^{10}	88	44
R2	2.8×10^{19}	242.4	0
R3	1.3×10^{10}	150.5	418
R4	3.28×10^{14}	196.5	418
R5	4.28×10^{6}	108	-42

Table 4.3: Thermophysical properties pertaining to 5-step reaction model in the solid fuel.

Species	Molecular weight (g)	Density (kg/m^3)	Thermal conductivity (W/mK)	Specific heat (kJ/kgK)	Source
Moisture	-	1000	0.596	4.2	[120]
Cellulose	-	420	0.24	2.3	[121], [4]
Active cellulose	-	420	0.24	2.3	[121], [4]
Char	-	73	0.1	1.1	[121], [4]
Gases & Tar	28	-	0.025	1.005	Assumed (Air)

A simplified stoichiometric relation

$$CH_4 + 2(O_2 + 3.76N_2) \rightarrow CO_2 + 2H_2O + 7.52N_2 \tag{4.1}$$

is used to model the chemical reaction between air and fuel vapor in the gas phase generated by solid pyrolysis, where the latter is modeled as methane. It is noted that the main pyrolysis gases produced by cellulose contain carbon dioxide, carbon monoxide and hydrogen in addition to methane. It was indicated by Yang *et al.* [110] that methane is a main gas product during the pyrolysis of cellulose, hemicellulose and lignin. Following the work by Dahale *et al.* [122] who used methane as a surrogate fuel for the modeling of wildland fires, here, methane is used as a surrogate to facilitate the modeling.

4.2.2 Thermophysical Properties

Due to a lack of correlations for thermo-physical properties of cellulose, the given correlations for wood are used. As discussed in Section 1, FMC affects the thermal properties of the material which we modeled as follows. The Fiber saturation point (FSP) of most woods ranges from 30–40% (dry basis) which is equivalent to 23–29% (wet basis) [37, 123]. Beyond the FSP, all the water in the plant cell lumen existed as free state. Below the FSP, as FMC increases, both the density and volume increases until FSP is reached; above FSP, only density increases. For all FMC, Eq .4.2 described the relationship between density and FMC [123]. Thermal conductivity and specific heat capacity were considered moisture dependent only when FMC is below FSP using Eqs. 4.6–4.7 from [123]. Eqs. 4.3 and 4.4 are used for the conductivity and heat capacity respectively, when FMC = 0. The correlation in Eq. 4.6 given in [123], which includes the moisture content through dependency on FMC has been proposed for temperature 24°C. It is noted that the value of conductivity calculated by setting FMC = 0 in this correlation differs slightly from the value obtained through Eq. 4.3 for 24°C. These thermophysical property correlations were used for the solid species for all the simulations. The properties for the gas species were assumed from the available data for air.

$$\rho_{\text{cellulose}} = 1000\, G_m \left(1 + \frac{M_c}{100}\right) \qquad (\text{kg}\,\text{m}^{-3}), \tag{4.2}$$

$$k_{\text{cellulose}-d} = 0.08124 + 0.003695\, T \qquad (\text{W}\,\text{m}^{-1}\,\text{K}^{-1}), \tag{4.3}$$

$$c_{\text{cellulose}-d} = 0.1031 + 0.00386\,T \qquad (\text{kJ}\,\text{kg}^{-1}\,\text{K}^{-1}), \tag{4.4}$$

$$A = (2.31 \times 10^{-4}\,T - 1.33 \times 10^{-4}\,M_c - 0.06191)\,M_c \tag{4.5}$$

$$k_{\text{cellulose}-m} = G_m\,(0.1941 + 0.004064\,M_c) + 0.01864 \qquad (\text{W}\,\text{m}^{-1}\,\text{K}^{-1}), \tag{4.6}$$

$$c_{\text{cellulose}-m} = (c_{\text{cellulose}-d} + 0.0491\,M_c)/(1 + 0.01\,M_c) + A \qquad (\text{kJ}\,\text{kg}^{-1}\,\text{K}^{-1}), \tag{4.7}$$

$$c_{\text{char}} = 1.39 + 0.00036\,T \qquad (\text{kJ}\,\text{kg}^{-1}\,\text{K}^{-1}), \tag{4.8}$$

Here ρ, G_m, M_c, k, T and c represent density, specific gravity, FMC, thermal conductivity, temperature and specific heat, respectively. Subscripts m and d represent moist and dry conditions. The specific gravity was based on softwood species [123]. The properties for the remaining solid species were considered constant.

4.3 Model Verification and Validation

In order to investigate the adequacy of the resolution used in the gas phase, simulations with FMC of 80% were conducted at two other resolutions, a higher

resolution $120 \times 120 \times 160$, and a lower resolution $48 \times 48 \times 64$. The sensitivity of the results to the grid size was studied by comparing the heat release rates (HRR) calculated for three resolutions including the original one $72 \times 72 \times 96$. The peak HRR was found to increase by 10% as the grids were refined. This dependency of the results on the grid is believed to be inevitable due to the LES approach used in this work, which is based on spatial filtering (physical LES) [124]. The grid size δ is identical to the filter width Δ, i.e., $\Delta/\delta = 1$. This ratio is widely used in LES computations while it is acknowledged that it leads to less numerical accuracy, compared to the case simulated with the same δ but higher Δ. In other words, for an LES wuth fixed computational cost (fixed δ), the case with a larger value of Δ/δ will produce more numerically accurate results; however, a smaller range of turbulent motions will be resolved [124]. Another criterion for testing the grid resolution in fire modeling is based on the ratio $D^*/\delta x$, where D^* is a characteristic length scale of the fire obtained from the total heat release rate $\dot{Q}$ and ambient density, specific heat, temperature and δx is the grid size.

$$D^* = \left(\frac{\dot{Q}}{\rho_o c_p T_o \sqrt{g}} \right)^{2/5} \tag{4.9}$$

Based on past numerical experiments, a ratio of 5–10 "usually produces favorable results at a moderate computational cost" [125]. In the present work, for the grid $72 \times 72 \times 92$, the ratio $D^*/\delta x$ is about 15, which meets this criterion.

Another criterion to test the resolution based on the measurement of turbulent resolution (MTR) has been investigated to assess the quality of the grid [117],

$$\mathrm{MTR}(\mathbf{x}, t) = \frac{k_{\mathrm{sgs}}}{k_{\mathrm{res}} + k_{\mathrm{sgs}}} \tag{4.10}$$

where

$$k_{\mathrm{res}} = \frac{1}{2}\tilde{u}\tilde{u} \tag{4.11}$$

$$k_{\mathrm{sgs}} = \frac{1}{2}(\tilde{u} - \hat{\tilde{u}})(\tilde{u} - \hat{\tilde{u}}) \tag{4.12}$$

Here, $\tilde{u}$ is the resolved filtered LES velocity and $\hat{\tilde{u}}$ is test filtered at a scale 2Δ. The time averaged values of MTR were found to lie between $0.25 - 0.4$ indicating that $60 - 80\%$ of the kinetic energy was being resolved in the flow using the resolution of $72 \times 72 \times 96$.

Prior to simulating the effects of FMC and radiation on pyrolysis and ignition in the configuration described in Section 4.2, verification and validation exercise was performed. Most bench-scale pyrolysis experiments that have been conducted to date are essentially designed to provide 1D/0D behavior [74] and hence verification was done for simpler configurations. Direct validation of results through comparison with experiments involving the three-dimensional configuration using radiation as the heat source was not possible. This is because there is no known facility that has the capability to study the phenomena in detail. Recent experiments conducted by Pickett *et al.* [8] and Gallacher *et al.* [115] are three-dimensional in nature; however, they focused on using convective heating, not radiation. The modeling results were

compared with the available experimental data of Pickett *et al.* [8] and Gallacher *et al.* [115] with convective heating and the results could be found elsewhere [126, 127].

In order to verify the extended BS model, we compared results from [4] with simulations from Gpyro, a one-dimensional version of Gpyro3D without the external gas phase. The configuration consisted of a one dimensional slab of cellulose with thickness of 0.025 m exposed to combined radiative and convective heating on one side and insulated on the other. The radiative and convective temperatures increased from 450 K to 1100 K using a heating rate of 15 K/s, following Ref. [4]. Since [4] did not include moisture, reaction R1 was not included for this validation. The thermophysical properties used for this study is given in Table 5.3 following [4].

Figures 4.2(a-c) illustrate the comparison between temperature, mass concentration of active cellulose and gas phase species velocity along the thickness of the slab. It is evident from these figures that the results of the current study are in reasonably good agreement with Di Blasi's results [4]. The greatest discrepancy between the current model and Di Blasi's occurred in the gas phase velocity. We attribute this difference to unavailable data with respect to the molecular weights and specific heats of gas species in Di Blasi [4] for which the data pertaining to air has been assumed. Note the abrupt increase and decrease in the concentration of active cellulose fig. 4.2(b). Active cellulose is formed initially as a result of depolymerization of cellulose; however, due to pyrolysis, it underwent further destruction to char and gas species. The gas phase species velocity, in fig. 4.2(c) arises from pressure gradients inside the specimen. The difference in magnitude of velocities in Di Blasi's and the present study was 0.01 m/s.

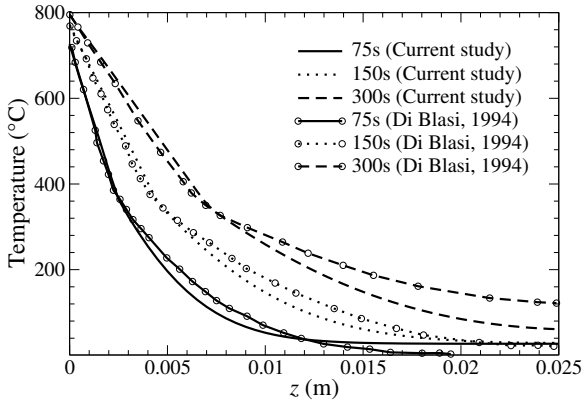

(a)

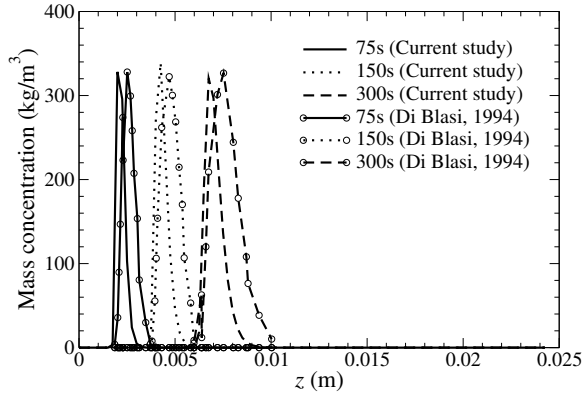

(b)

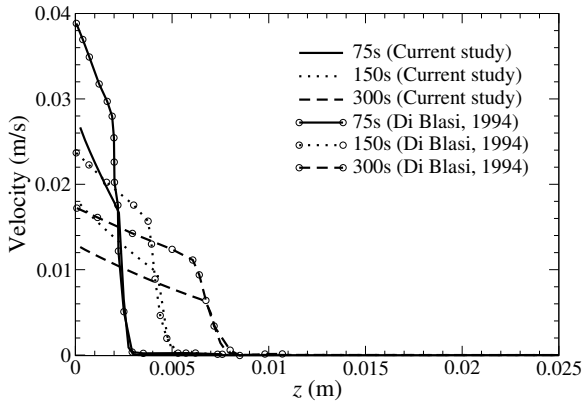

(c)

Figure 4.2: Verification of results of current study using Gpyro for cellulose pyrolysis with simulations of Di Blasi [4]. Quantities are plotted along the length of the specimen at different times; (a) temperature (b) mass concentration of active cellulose and (c) velocity of gas species.

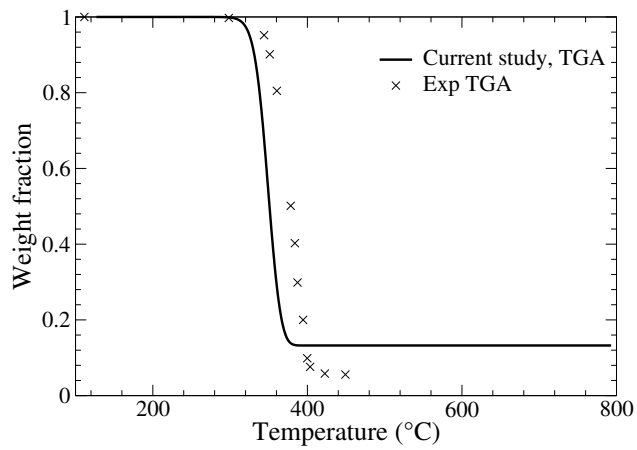

Figure 4.3: Verification of results of current study using Gpyro TGA setup (solid line) with TGA data of Reed and Posey [5] (crossmarks).

Reed and Posey [5] heated 0.006 g of cellulose at a rate of 40 K min^{-1} to generate TGA data. Their data provided an opportunity to further verify the BS model. A zero-dimensional version of Gypro with the BS model simulated the TGA data. Here gain the R1 reaction was excluded. As seen in fig. 4.3, the remaining weight predicted by the model for this setup agreed well with the experimental data [5].

4.4 Results and Discussions

The classical combustion model for a thermally thin fuel particle assumes that all moisture will first evolve from the sample at a temperature near the boiling point of water [20]. Ignition occurs when a combustible mixture of pyrolysis gases are obtained and follows shortly after moisture evaporation is complete [8]. Results from our simulation of the ignition of a modeled leaf by radiation enabled us to test this assumption. The time history of temperature and mass fraction of moisture in the

simulated fuel are plotted at the point A in fig. 4.4 for FMCs of 5, 40 and 80%. This point A in fig. 4.1, is located in the solid phase in proximity to the heat source. As FMC increased, the time at which rapid temperature increase occurs is delayed slightly; the difference in time was less than 1 second (fig. 4.4a). This behavior could be attributed to a higher bulk thermal conductivity as the amount of water in the solid fuel increased. Also, from this figure, we observed that ignition occurred when the temperatures reached 400-500°C for all the FMC cases. The decay of mass fraction of moisture can be found in fig. 4.4(b). Note that the moisture mass fraction is equivalent to the moisture content expressed on a wet mass basis in [37]. Rapid moisture loss occurred earliest in the driest fuel and later in the fuels with higher water content; however, the time at which all moisture was evaporated differed by 0.8 seconds. For all the FMC's, considered evaporation occured when the temperatures reached 200-300°C.

In order to analyze the temperature and FMC in the solid fuel at a region away from the heat source, temperature and mass fraction distribution of moisture were plotted in fig. 4.5 at time 5 s at which gas phase ignition had occurred for 5% FMC case. From figs. 4.5(a,b) its is observed that temperature rise and evaporation of moisture were confined to a local region close to the heat source. The temperature was higher by approximately 700 K for 5% FMC case at the leading edge of the solid fuel. The 40 and 80% cases differed in temperature by less than 50 K in this region and differed by very little along the rest of the solid fuel. Similarly, the temperature for the 5% FMC decreased by only 100 K over the majority of the solid fuel (-0.017 to 0.02 m). Also a significant amount of moisture remained in the sample

at the time of ignition for the 40 and 80 % cases. In the area closest to the heat source (-0.02 to -0.016 m), the moisture mass fraction was 0; however, the mass fraction was unchanged in the region -0.012 to 0.02 m indicating the local nature of the evaporation process. In contrast, evaporation occurred in the 5% case along the majority of the fuel length. Pickett *et al.* [8] included some discussions on time histories of temperature at two points on the surface of manzanita species, one located on the perimeter and the other at the middle of the leaf. They reported that at the perimeter point, evaporation occurred when the temperature was in the range of 200-300°C. Furthermore, they observed that ignition occurred at this point after the evaporation process was completed and its temperate reached around 350-400°C. When the perimeter point ignited, the measured temperature at the middle point was 150°C. They concluded that a significant amount of moisture was present at the middle when the perimeter point ignited. This local evaporation feature as observed in the experiments is consistent with the local evaporation phenomenon found in the present work.

The evolution of overall mass loss rate (rate at which gas species are formed from the solid) and overall mass normalized by initial total mass is shown in fig. 4.6(a) and 4.6(b), respectively. MLR in each of the computational cell within the solid fuel is calculated following the expression $\sum_{\alpha}(\dot{\omega}'''_{fg\alpha} - \dot{\omega}'''_{dg\alpha})\nabla \mathrm{v_s}$, where α, v represents gas phase species and the volume of the computational cell respectively. Later, this is integrated over the domain of the solid fuel to obtain the overall MLR. Water vapor evaporating from the fuel and fuel vapor comprised the gas species that diffuses from the solid phase to the external gas phase domain. The time at which MLR is positive

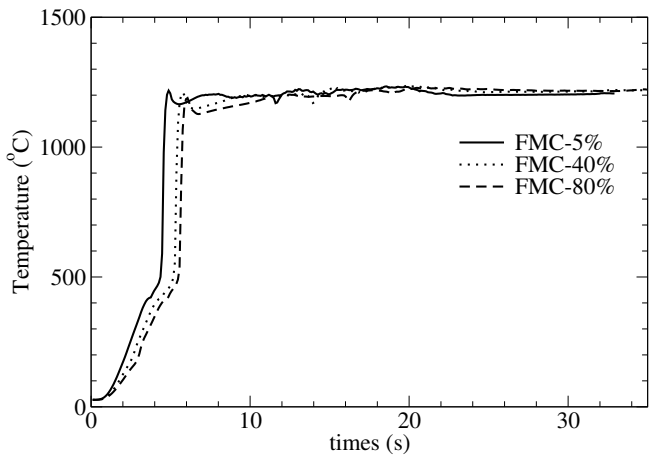

(a)

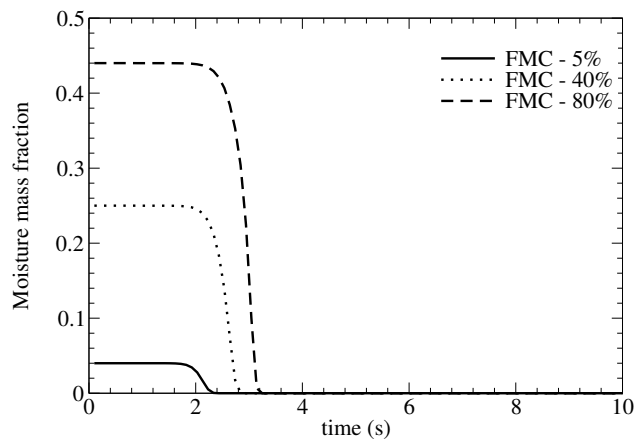

(b)

Figure 4.4: Time history of (a) temperature, and (b) mass fraction of moisture at point A (see fig. 6.1) for three cases with an initial FMC of 5, 40 and 80%.

may be considered as the time of initiation of moisture loss which occurred at 2.5 s for all FMC's. Note that the MLR curves exhibited two overall peaks. The first peak represented water vapor and the second peak represented fuel vapor. As FMC increased, the first peak increased in magnitude due to more water vapor being lost during the drying phase. The MLR associated with the second peak did not differ greatly for varying FMC; maximum MLR at the second peak ranged from 0.09 to 0.12 g s^{-1}. The normalized mass exhibited a similar trend for all three FMCs.

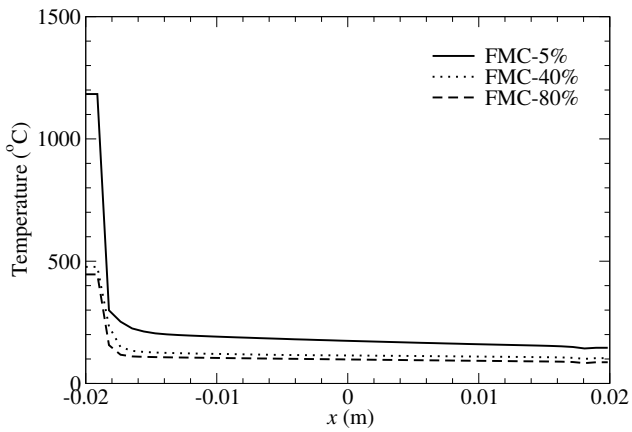

(a)

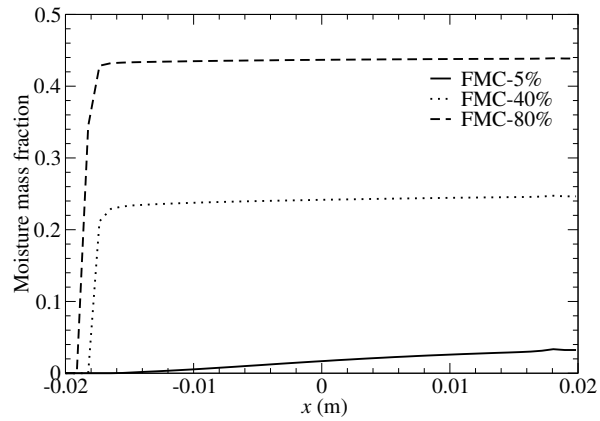

(b)

Figure 4.5: Variation of (a) temperature and (b) mass fraction of moisture along x at $y = 0$ and $z = 0.031$ m at time 5s in the solid phase for three cases with an initial FMC of 5, 40 and 80%.

Oxidation of the gas phase fuel vapors results in flaming combustion. The time histories of global HRR and burn rate are shown in fig. 4.7(a) and 4.7(b) for three FMC's investigated. The HRR quantifies the amount of heat generated due to stoichiometric combustion of fuel vapors with oxygen in the gas phase (Eq. 2.8). The global HRR is computed using the expression $\sum \overline{\dot{q}'''} \nabla \mathrm{v}$, where $\overline{\dot{q}'''}$ and v represents HRR per unit volume (Eq. 2.8) and volume of the computational cell in the gas phase domain respectively. HRR values are used as an indicator of gas phase

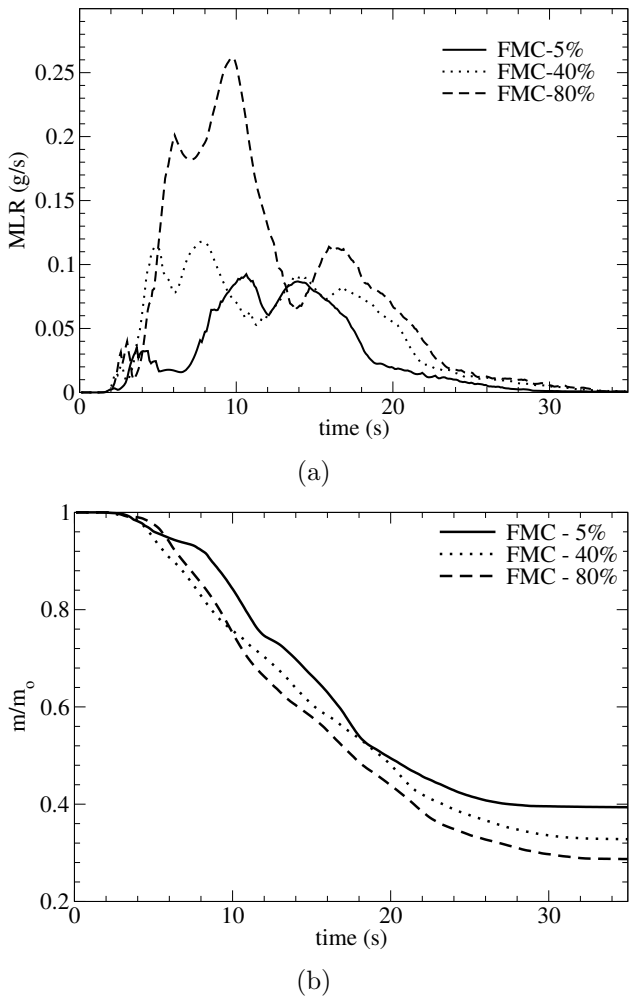

Figure 4.6: Time history of (a) mass loss rate and (b) normalized mass in the solid phase for three cases with an initial FMC of 5, 40 and 80%.

ignition. From fig. 4.7(a), it can be seen that the initial FMC influenced the time at which ignition occurred. Ignition occurred at t=3.5, 4, and 4.2 s for FMC = 5, 40, and 80% ,respectively. The second ignition point occurred at $5.8, 8.0, 10.0$ s for FMC of 5, 40 and 80%, respectively. The burn rate indicates the rate at which the fuel is consumed by the combustion reaction in the gas phase. From the figures, it is observed that burn rate follows the same trend as the HRR displaying two ignition points.

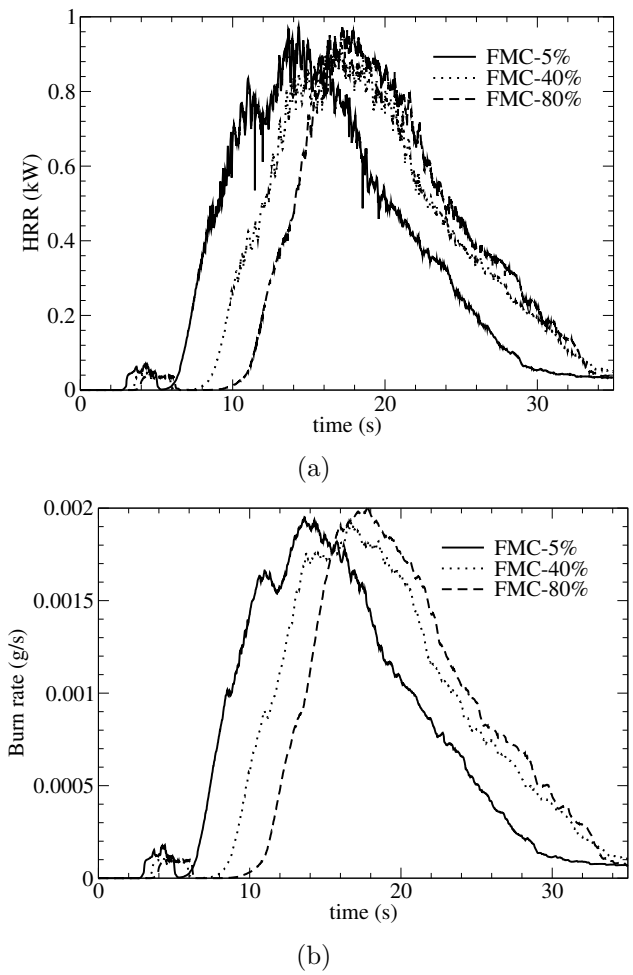

Figure 4.7: Time history of (a) heat release rate and (b) burn rate in the gas phase for three cases with an initial FMC of 5, 40 and 80%.

In order to the investigate the evolution of moisture in detail, the case with FMC of 80% was chosen. The solid fuel degradation model based on the 5-step extended BS mechanism included four solid and four gas phase species (Eq. R1-R5). Figures 4.8(a) and 4.8(b) illustrates the time history of all mass fractions of solid and gas species at point A inside the solid fuel, respectively. The conversion of solid to gas during thermal decomposition occurred as follows. In case of solid species, the first degradation reaction occurred around 2.5 s and accounted for phase

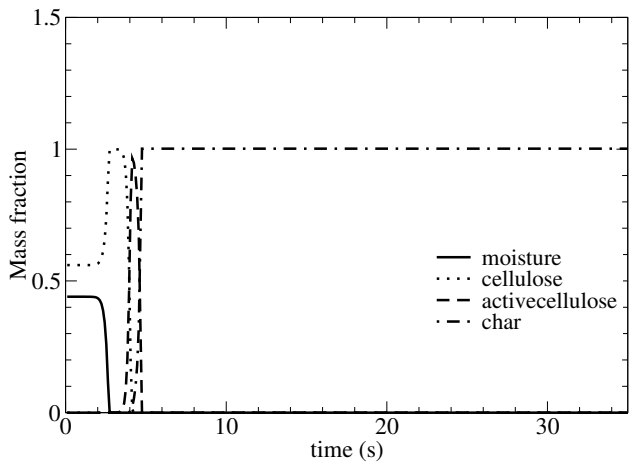

(a)

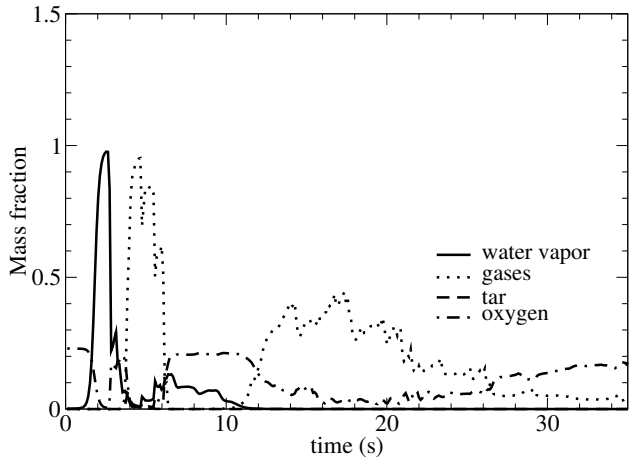

(b)

Figure 4.8: Time history of (a) solid species and (b) gas species in the solid phase for a case with an initial FMC of 80% at point A.

transformation of moisture to water vapor. At this time, an increase in the mass fraction of cellulose occurs as the mass of moisture exits the solid phase. Shortly thereafter as the temperature of the solid fuel increases, cellulose is converted to active cellulose which then later breaks down to char, fuel vapors, and tar. Char remains as a residual species in the solid fuel and does not undergo further degradation. From fig. 4.8(b) it is evident that water vapor formed in the solid and fuel vapors begin

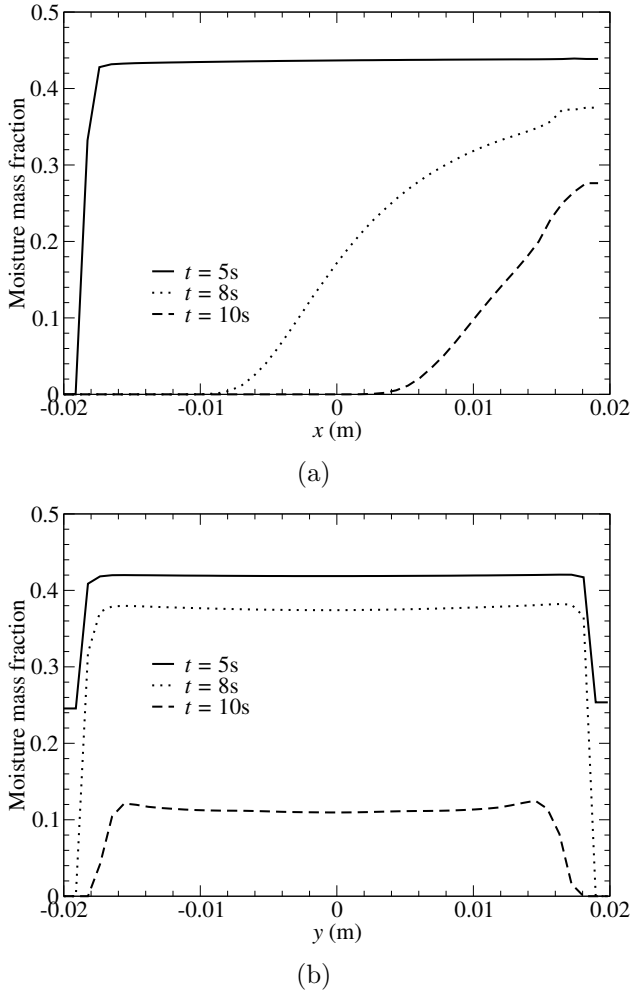

Figure 4.9: Variation of moisture mass fraction (a) along x at $y = 0$ and $z = 0.031$ m and (b) along y at $x = 0.0125$ m and $z = 0.031$ m at various times in the solid phase for a case with an initial FMC of 80%.

to evolve before the water vapor diffused out. The fuel vapors diffused into the gas phase domain at 5 s which resulted in ignition due to reaction with oxygen at t=5 s. The mass fraction of fuel vapors increased at t=10 s due to diffusion from the neighboring solid phase cells. Tar cracking consumed oxygen; however, it eventually diffused back into the solid from the external gas phase domain.

The spatial variation of moisture mass fraction within the solid fuel along x and y axis is illustrated at different time instants in figs. 4.9(a) and 4.9(b) in the solid fuel. In fig. 4.9(a) a drying front propagated along the length of the solid fuel over time. Two drying fronts propagated transversely from the edges of the solid fuel inward (fig. 4.9(b)). It is clear that evaporation occurs at the edges of the solid fuel at a higher rate than in the center. At t= 10 s local peaks in mass fraction of moisture are observed in regions located closer to the edges of the solid fuel. This is a result of non-uniform heating that arises due to the propagation of thermal fronts from the leading edge and the two lateral edges of the solid fuel. At the time of ignition, the solid fuel still contains a significant amount of moisture, indicating that different regions in the domain pyrolyzed/ignited at different instants (figs 4.10a, b, c). The appearance of high moisture gradients at the leading and the two lateral edges indicated a non-uniform evaporation phase during the ignition of the solid fuel in our simulations. This observation is in a general agreement with the observation made by Pickett *et al.* [8] through the IR measurements.

As described by [114], water vapor in the combustion environment arises from two sources–evaporation of water contained in the fuel and water produced by the combustion reaction. The simulations tracked H_2O in the gas phase by solving a single transport equation. The mass fractions of H_2O, CO_2, O_2 and fuel vapors immediately above the solid fuel changed along the length of the fuel (x). At time 5 s in the fig. 4.11(a), we observe a reaction zone corresponding to the first ignition point accompanied by products such as water vapor and carbon dioxide at x = -0.02 with an oxygen deficient region ahead of the reaction zone at x = -0.0125 m characterized

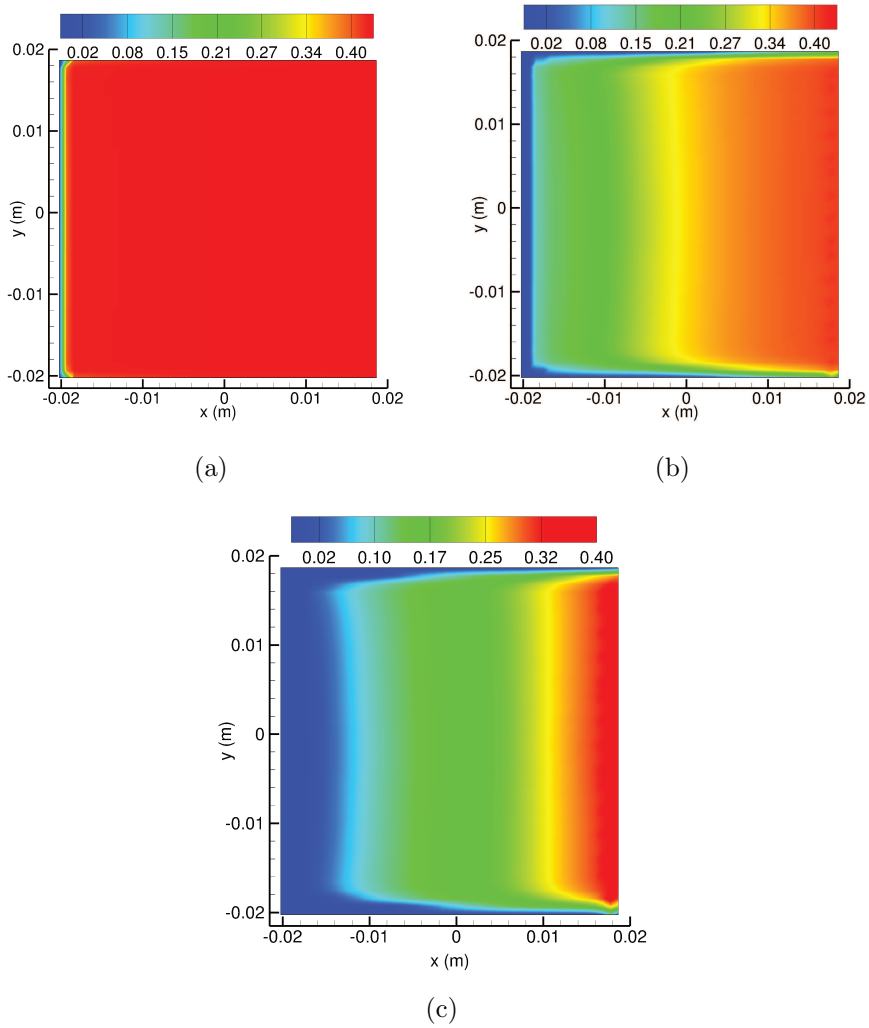

Figure 4.10: Contours of moisture mass fraction in the solid fuel along x at (a) $t =$ 5 s (b) $t = 6.5$ s and (c) $t = 7.75$ s on an xy-slice located at $z = 0.031$ m for a case with an initial FMC of 80%.

by an oxygen mass fraction of 0.11. At time 7.5 s in fig. 4.11(b), we observe an increased evaporation ahead of the ignition zone illustrated by the second peak in mass fraction of water vapor. This resulted in further reduction of oxygen ahead of the ignition zone. The first peak is due to formation of water due to combustion and second peak is due to evaporation from the solid fuel. In fig. 4.11(c) at time 11 s we observe the initiation of another reaction zone corresponding to second ignition point

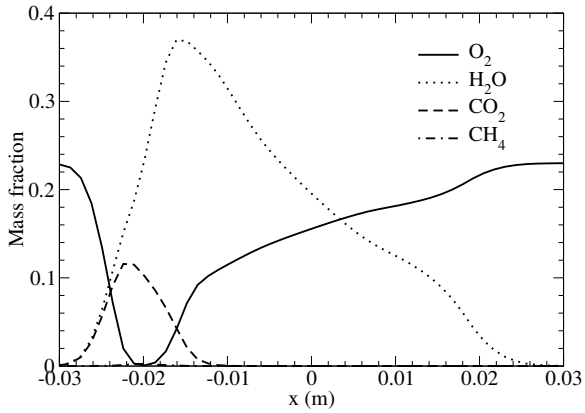

(a)

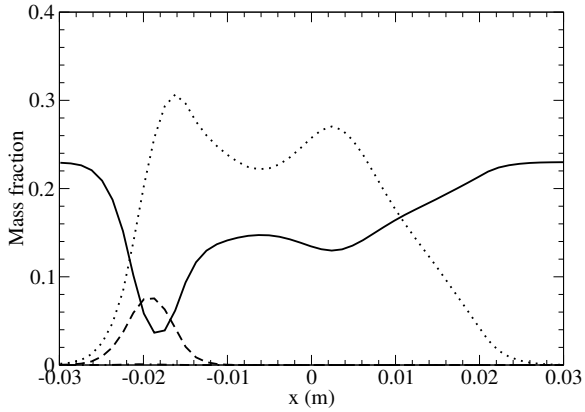

(b)

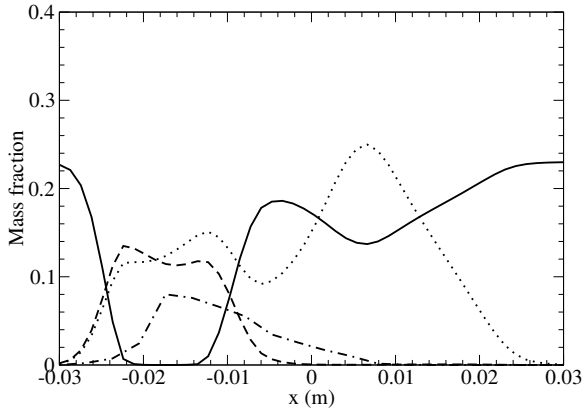

(c)

Figure 4.11: Variation of mass fraction of tracked gas species at time (a) 5 s (b) 7.5 s and (c) 11 s along x at $y = 0$ and $z = 0.035$ m in the gas phase domain for a case with an initial FMC of 80%.

accompanied by oxygen mass fraction of 0 at the leading edge of the solid fuel. This is due consumption of oxygen by the combustion reaction. However ahead of this region x = -0.0075, oxygen has replenished and this aids the flame spread to other regions of the solid fuel.

To investigate further, two-dimensional contours of temperature, volume fraction of oxygen and moisture are plotted at $5\,\mathrm{s}, 7.5\,\mathrm{s}$ and $11\,\mathrm{s}$ on an xz slice located at $y = 0$ in figs 4.12, 4.13 and 4.14 in the gas phase domain. The flaming combustion zone which is represented as the first ignition point in fig. 4.12(a) was observed initially at the tip of the solid fuel located close to the heating source. As seen from fig. 4.12(b), the water vapor is predominant in the ignition zone as well as in the region away from it, clearly manifesting the point that evaporation and combustion occur together. The water vapor present in the ignition zone is a result of combustion however its presence ahead of the ignition zone is due to evaporation form the solid fuel. The presence of this released water vapor in fig. 4.12(b) ahead of the ignition zone causes dilution and as a result oxygen gets depleted, fig. 4.12(c). At time $7.5\,\mathrm{s}$, ignition zone has reduced in fig. 4.13(a), and in fig. 4.13(b) high volume fraction of water vapor is observed and this is accompanied by oxygen depletion (fig. 4.13 c) ahead of the ignition zone. When most of the water vapor has evaporated (fig. 4.14 b) in the gas phase domain at $x = 0$, we observe a second ignition at the tip of the solid fuel (fig. 4.14a) and corresponding to this in fig. 4.14(b), oxygen has replenished ahead of the ignition zone. Also from fig. 4.14(b), we observe high mass fraction of water vapor at the trailing edge illustrating that significant amount of vapor is released during to evaporation compared to that formed during combustion. The

flame due to second ignition later spreads from the leading edge and the lateral edges towards the trailing edge of the solid fuel.

Figure 4.15 shows the relative importance of the convection and radiation heat transfer in igniting the solid fuel particle. The negative heat fluxes values observed in case of convection during initial time accounts for the heat transfer between the heated wall and the surrounding gas. However later in time when the solid fuel ignites, it undergoes cooling through natural convection which results in increased convective heat flux. The positive radiative heat flux observed during the initial time accounts for the radiation energy absorbed by solid fuel from the external gas phase domain. Later when the solid fuel ignites, it emits radiation back into the gas phase which results in negative heat flux as seen from the figure. The role of thermal radiation in causing gas phase ignition has also been investigated by considering many cases where in the solid fuel was exposed to a heated surface maintained at different temperatures. Ignition was observed only when the temperature of the heated surface exceeded 1100 K indicating that thermal radiation can ignite the fuel without the use of a pilot source provided the temperature of the heating source is significantly high.

Finally, shown in figs. 4.16(a) and (b) are a contour plot for temperature and velocity vectors in the gas phase at t= 15 s. From fig. 4.16(a), it is observed that the flame is turbulent due to the entrained flow from the external ambient air and due to the interaction with boundary layer developed over the heated wall. From fig. 4.16(b), its is evident that large scale vortical structures formed as a result of straining between the buoyant plume region and the external air. Furthermore, the

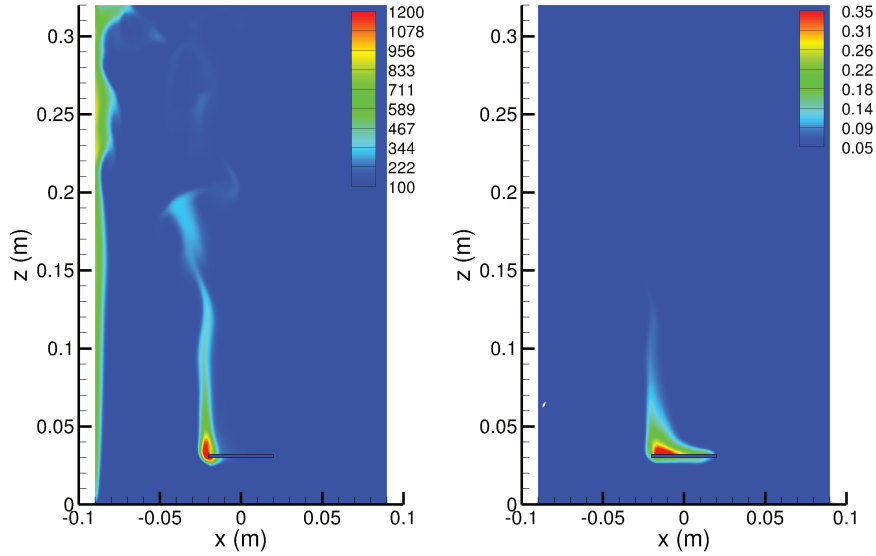

(a)

(b)

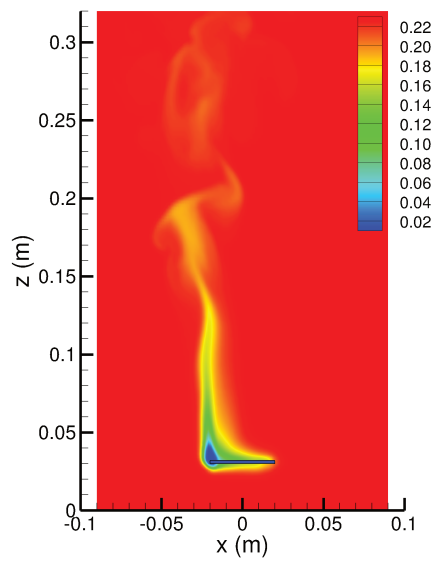

(c)

Figure 4.12: Gas phase contours of (a) temperature (°C), (b) water vapor mass fraction and (c) oxygen mass fraction at $t = 5$ s on an xz-slice located at $y = 0$ for a case with an initial FMC of 80%.

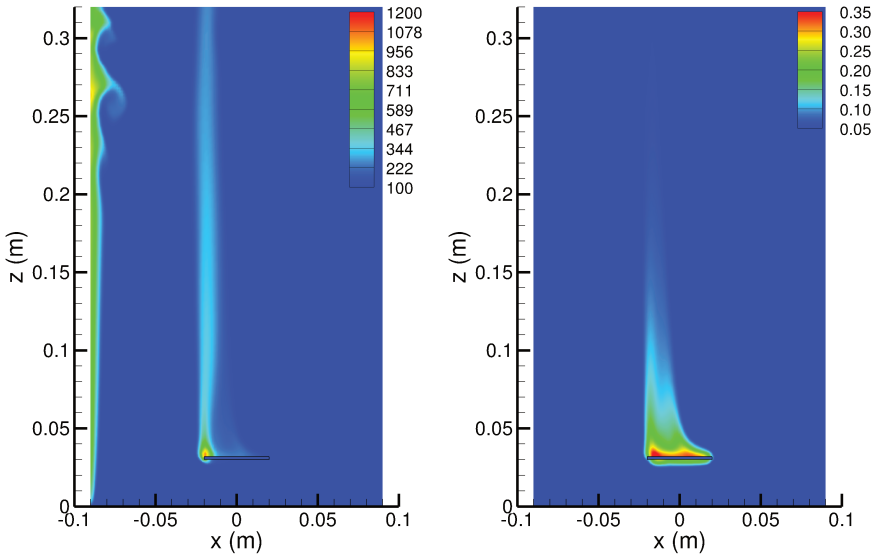

(a)

(b)

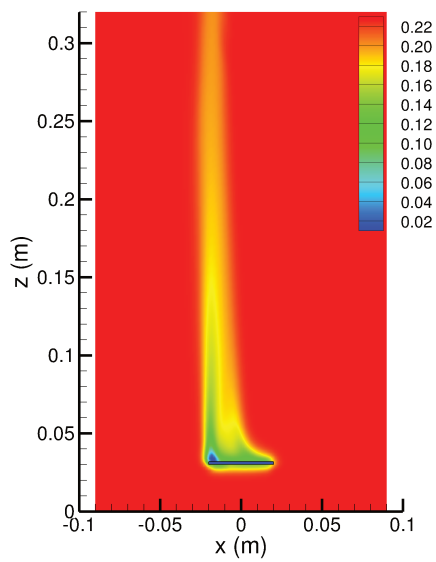

(c)

Figure 4.13: Gas phase contours of (a) temperature (°C), (b) water vapor mass fraction and (c) oxygen mass fraction along x at $t = 7.5$ s on an xz-slice located at $y = 0$ for a case with an initial FMC of 80%.

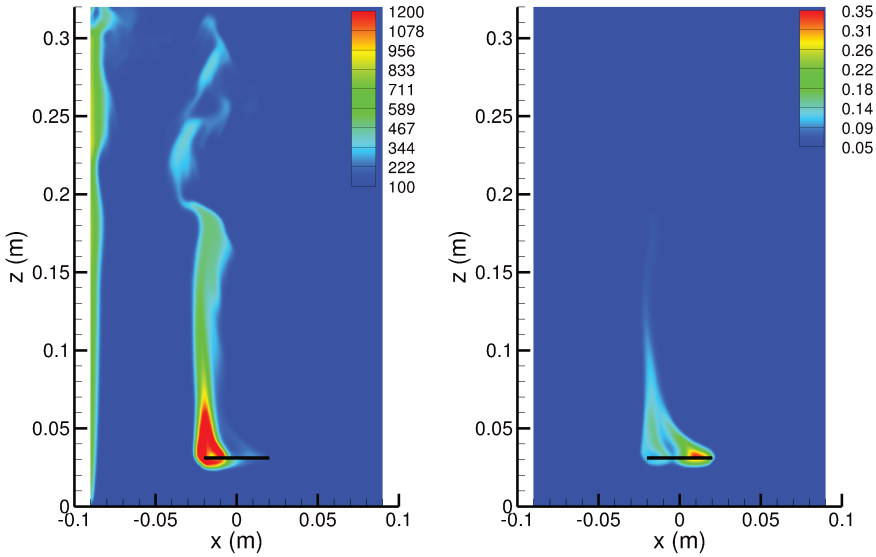

(a)

(b)

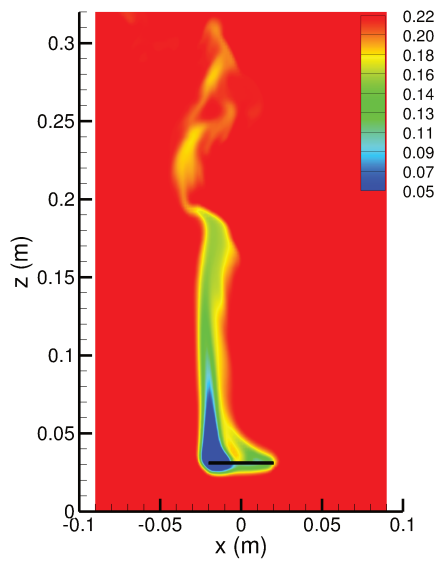

(c)

Figure 4.14: Gas phase contours of (a) temperature (°C), (b) water vapor mass fraction and (c) oxygen mass fraction along x at $t = 11$ s on an xz-slice located at $y = 0$ for a case with an initial FMC of 80%.

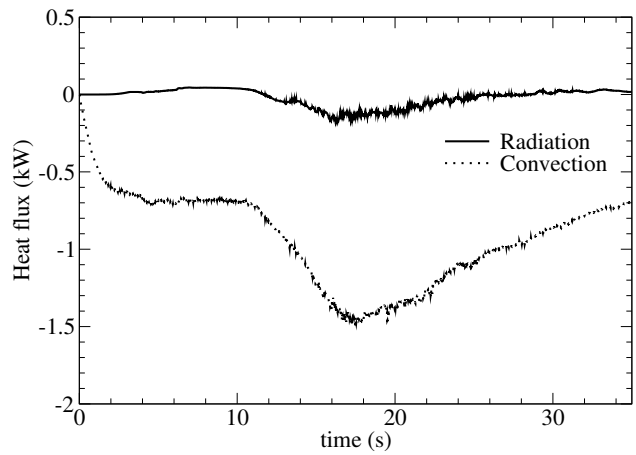

Figure 4.15: Time history of global radiation and convection fluxes for a case with FMC of 80%. Positive heat flux means heat is transferred from gas to solid particle and negative heat flux means vice versa.

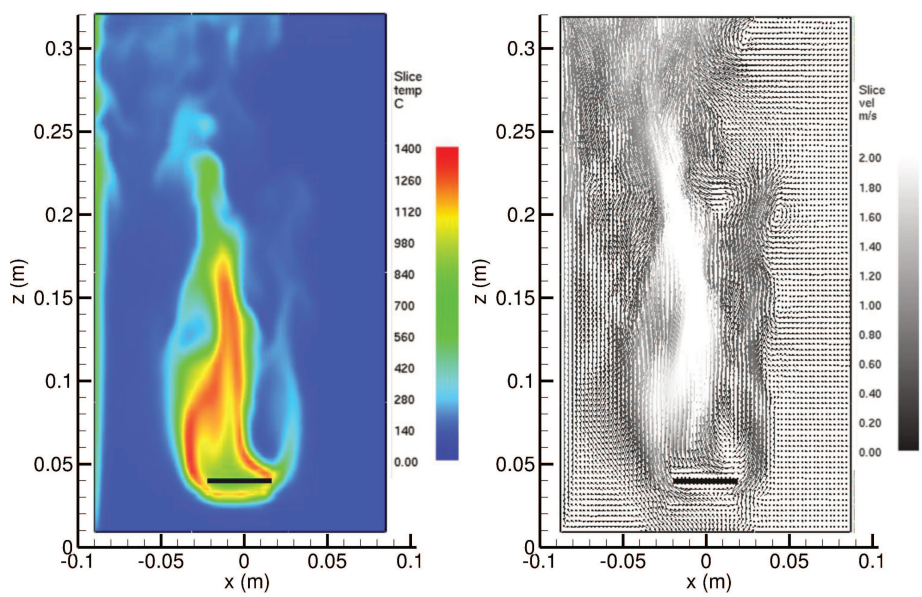

(a) (b)

Figure 4.16: (a) Gas phase temperature contours (°C), and (b) velocity vectors at time 15 s on an xz-slice located at $y = 0$ for a case with an initial FMC of 80%.

plume interaction with boundary layer formed over the heated wall is evident farther up in the plume region.

4.5 Chapter Summary

The effect of fuel moisture on pyrolysis and combustion of a live vegetation represented as a thin cellulosic fuel element subjected to radiative heating has been investigated. A thermal degradation reaction mechanism used for cellulose breakdown was initially verified and validated with previously published simulation and TGA experiments. Fuel moisture content of 5%, 40% and 80% were considered and studied in detail. The temperature response and thermal degradation rate was higher for the case with 5% FMC and ignition occurred prior to the 40% and 80% FMC case. The simulations also indicated that water evaporated locally near the point of ignition and remained elsewhere. Local peaks in the mass fraction of moisture was observed at a region located close to lateral edges of the solid fuel. In the gas phase, high volume fraction of water vapor observed in the region close to the combustion zone as well as away from this region.

CHAPTER 5

HORIZONTAL FUEL CONFIGURATION: INFLUENCE OF MOISTURE STATES AND CONVECTIVE HEAT TRANSFER

5.1 Introduction

The main focus of the study in this chapter is to investigate the influence of the convection heat transfer on pyrolysis and ignition of a horizontally oriented fuel element. A chemistry model, more advanced than that used in the previous chapter, which includes the important components hemicellulose and lignin in addition to cellulose and moisture [44], is utilized here. Also, another advanced aspect of the model, compared to the previous chapter, is to take into account various states of moisture within the fuel.

The moisture within vegetation exists in two forms depending on the Fiber Saturation Point (FSP). Most woods have an FSP ranging from 23–30% (wet basis) [37, 123]. Above the FSP, all water in plant cell lumen exists as free state whereas below FSP, it exists as bounded state in cell walls. Water is bound in cell walls to the hygroscopic constituents: cellulose and hemicellulose, however, it is freely present in the lumen.

Hemicellulose, cellulose and lignin are the three main components of biomass [110]. It was suggested in [128] and [129] that the pyrolysis of any biomass can be considered as the superposition of these three main components. Thus, the knowledge of decomposition characteristics of cellulose, hemicellulose and lignin is the basis for a better understanding of biomass thermochemical conversion. Di Blasi [4], as discussed in Chapter 1 used the Briodo–Shafizadeh kinetic model of cellulose pyrolysis and extended the primary reactions to include secondary reactions for tar cracking. Miller & Bellan [6] used this extended BS model as a "skeleton" and formulated a superposed kinetic scheme for cellulose, hemicellulose and lignin kinetics. This model has been incorporated in the present work as a reaction mechanism for the three primary biomass components involving multi-step kinetics for competitive primary pyrolysis and secondary tar decomposition reactions.

According to McAllister *et al.* [59], who studied ignition of fine fuels, when thermal radiation alone was used as a heating mode, an additional pilot source was required to initiate ignition. On the other hand, according to Pickett *et al.* [8], when convective heating was applied on the fuel sample by subjecting it to hot gases, it ignited without the aid of a pilot flame. As discussed in Chapter 1, there appears to be some consensus that convective heat transfer likely plays the major role in ignition and fire spread in fires propagating in high wind conditions.

The main aim of the work described in this chapter is to improve our understanding of the effects of different forms of moisture on pyrolysis and gas phase ignition of a solid fuel subjected to convective heat transfer. Here, the fuel is composed of moisture, cellulose, hemicellulose and lignin, which undergoes multi-step

chemical reactions. Here also, the solid model uses Gpyro3D [74] for pyrolysis while the gas phase fluid dynamics and ignition are modeled by FDS [9, 117]. In the results to be shown, ignition time is defined as the time at which the heat release rate (HRR) becomes positive in the gas phase over the surface of cellulose element. Any value above it would represent an active flame in the simulation.

5.2 Computational Setup

Prior work has observed appreciable temperature and moisture variation on the surface of leaf fuel particles [8] and these gradients were observed along the depth of the fuel, indicating a three-dimensional nature of pyrolysis [59]. Therefore, to investigate these effects during fire initiation and propagation on fuel elements where multidimensional heat and mass transfer effects are significant, a fully coupled Gpyro3D-FDS model is used. An overview of the governing equations in FDS (gas phase domain) and Gpyro3D (solid phase domain) outlining the variables involved during the coupling of solid and gas phases was presented in Chapter 2.

The considered fuel element is a rectangular cuboid ($0.03 \times 0.03 \times 0.002$ m, Length $\times$ Width $\times$ Thickness) with fixed thickness. This configuration modeled the experimental setup studied by Pickett *et al.* [8]. A schematic of the physical domain is shown in fig. 5.1(a,b). The computational domain used for the gas-phase solver FDS is a box of size $0.18 \times 0.18 \times 0.32$ m. The grid resolution used in x, y and z directions is $120 \times 120 \times 160$, respectively. The solid fuel element is centered in the gas-phase domain and is located at $z = 0.05$ m. The initial temperature, moisture content, pressure, gaseous species mass fractions, and condensed phase species were

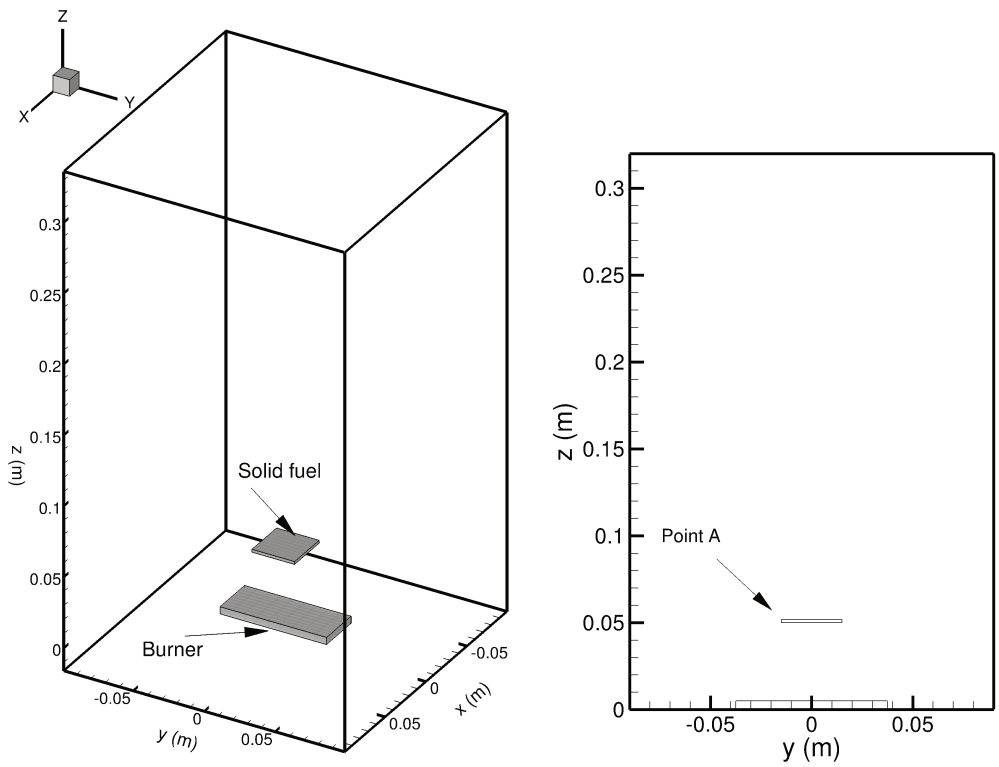

(a) (b)

Figure 5.1: (a) Isometric view of computational domain showing thin solid fuel subjected to convective heating from the burner, (b) two-dimensional view of computational domain along the zy-slice at $x = 0$. Point A is located at y = -0.015 m, $x = 0$, $z = 0.051$ m.

set uniform throughout the solid. The fuel element is simulated as a separate region modeled by Gpyro3D with a grid spacing of 0.0006 m in the x and y directions and 0.0003 m along the depth (z). Here, 9600 grid cells were used for the fuel element, which is exposed to convective heating due to the modeled burner with dimensions of 0.075×0.03 m, Length $\times$ Width. Heated air at 1000°C enters the domain through this burner at $t = 0$ s.

All computations were performed using message passing interface (MPI) protocol using 36 processors of Dense Memory Cluster (DMC) located at Alabama Su-

percomputer Authority. A typical simulation of 20 seconds required a wall time of 72 hours and 64 GB of memory.

5.3 Reaction Mechanism and Models

Initially, the solid phase domain consisted of moisture, cellulose, hemicellulose, lignin and the gas phase within the solid fuel consisted of standard air (nitrogen and oxygen). Their respective initial mass fractions are given in Table 5.1. The percentage distribution of cellulose, hemicellulose and lignin used were 33, 33 and 34 respectively % [44]. The initial mass fractions of other species were considered negligible. The initial temperature was set to equal an ambient temperature of 300K.

Table 5.1: Initial mass fractions

FMC	Free moisture	Bound moisture	Cellulose	Hemicellulose	Lignin	N_2	O_2
40%	0.2175	0.0725	0.2272	0.2272	0.2556	0.77	0.23
76%	0.315	0.105	0.19	0.19	0.20	0.77	0.23
120%	0.4125	0.1375	0.144	0.144	0.162	0.77	0.23

The reaction scheme outlined by Di Blasi [4] and Miller & Bellan [6] is shown in fig. 5.2.

Shown in fig. 5.2, reactions R1, R2, R3 are primary reactions and R4 is a secondary reaction. The primary reactions are concerned with conversion of virgin species to active state which later breaks down to lower molecular weight gases and char while the secondary reaction R4, which is an oxidation reaction, is concerned with breakdown of tar to low molecular weight gases. The term “virgin” refers to reactants cellulose, hemicellulose and lignin which follow the same reaction pathway (R1–R4).

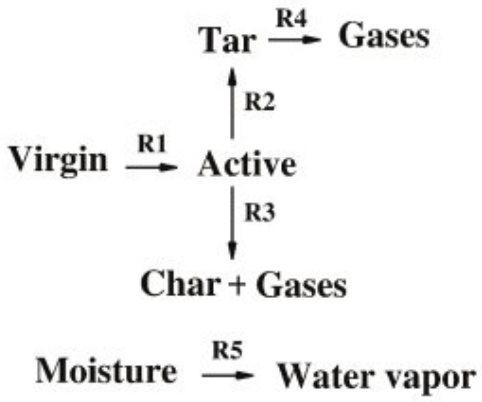

Figure 5.2: Generic reaction scheme used to model cellulose, hemicellose and lignin pyrolysis [6] along with vaporization reaction of moisture.

Here, R5 represents two evaporation reactions and has been incorporated to account for moisture in free and bound states. Free moisture evaporation reaction has been adopted from [120] and bound state evaporation has been adopted from [44]. This 12-step reaction model has been incorporated in Gpyro3D. The reaction kinetics and thermophysical properties for reactions R1-R5 are given in Tables 2 and 3 respectively.

Table 5.2: Kinetic data pertaining to 12-step reaction model in the solid fuel.

Cellulose			
Reaction	A (s^{-1})	E (kJ/mol)	Δh (kJ/kg)
R1	2.8×10^{19}	242.4	0
R2	3.28×10^{14}	196.5	418
R3	1.3×10^{10}	150.5	418
Hemicellulose			
Reaction	A (s^{-1})	E (kJ/mol)	Δh (kJ/kg)
R1	2.1×10^{16}	186.7	0
R2	8.75×10^{15}	202.4	418
R3	2.6×10^{11}	145.7	418
Lignin			
Reaction	A (s^{-1})	E (kJ/mol)	Δh (kJ/kg)
R1	9.6×10^{8}	107.6	0
R2	1.5×10^{9}	143.8	418
R3	7.7×10^{6}	111.4	418
Tar cracking			
Reaction	A (s^{-1})	E (kJ/mol)	Δh (kJ/kg)
R4	4.28×10^{6}	108	-42
Free water			
Reaction	A (s^{-1})	E (kJ/mol)	Δh (kJ/kg)
R5	2.8×10^{19}	88	44
Bound water			
Reaction	A (s^{-1})	E (kJ/mol)	Δh (kJ/kg)
R5	2.8×10^{19}	166	44

Table 5.3: Thermophysical properties pertaining to 12-step reaction model in the solid fuel.

Species	Molecular weight (g)	Density (kg/m^3)	Thermal conductivity (W/mK)	Specific heat (kJ/kgK)	Reference
Moisture	-	1000	0.596	4.2	[120]
Cellulose	-	420	0.24	2.3	[121], [4]
Hemicellulose	-	420	0.24	2.3	[121], [4]
Lignin	-	420	0.24	2.3	[121], [4]
Char	-	73	0.1	1.1	[121], [4]
Gases	28	-	0.025	1.005	Assumed (Air)
Tar	40	-	0.025	1.005	Assumed (Air)

The thermophysical properties were assumed to be identical for cellulose, hemicellulose and lignin [6]. Thermal conductivity and specific heat capacity were considered to be temperature dependent following correlations used for soft wood species [130]. The properties for the gas species present within the solid fuel were assumed from the available data for air .

$$\rho_{\text{cellulose}} = 1000\, G_m \left(1 + \frac{M_c}{100}\right) \qquad (\text{kg}\,\text{m}^{-3}), \tag{5.1}$$

$$k_{\text{cellulose}} = 0.08124 + 0.003695\, T \qquad (\text{W}\,\text{m}^{-1}\,\text{K}^{-1}), \tag{5.2}$$

$$c_{\text{cellulose}} = 0.1031 + 0.00386\, T \qquad (\text{kJ}\,\text{kg}^{-1}\,\text{K}^{-1}), \tag{5.3}$$

$$c_{\text{char}} = 1.39 + 0.00036\, T \qquad (\text{kJ}\,\text{kg}^{-1}\,\text{K}^{-1}), \tag{5.4}$$

As the solid fuel pyrolyzes, it releases fuel vapor into the gas phase domain external to the solid fuel. Initially, the gas phase domain consists of standard air (nitrogen and oxygen). A simplified stiochiometric relation

$$\text{CH}_4 + 2(\text{O}_2 + 3.76\text{N}_2) \rightarrow \text{CO}_2 + 2\text{H}_2\text{O} + 7.52\text{N}_2 \tag{5.5}$$

is used to model the chemical reaction between air and fuel vapor in the gas phase, where the latter is modeled as methane. It is noted that the main pyrolysis gases

produced by cellulose, contain carbon dioxide, carbon monoxide and hydrogen in addition to methane. Yang *et al.* [110] showed that methane is a main gas product during the pyrolysis of cellulose, hemicellulose and lignin.

5.4 Chemical Kinetic Model Validation

Prior to simulating the effects of FMC and convection on pyrolysis and ignition in the configuration described in Section 5.2, verification and validation of the kinetic model was performed. Most bench-scale pyrolysis experiments that have been conducted to date are designed to provide zero-dimensional behavior [74]. The verification exercise initially was done for simpler configurations using a 0D setup. Direct validation of results through the comparison with experiments involving the three-dimensional configuration using convection as the heat source will be discussed in the subsequent section.

The 12-step reaction mechanism has been validated against the experimental data of Koufapounas *et al.* [7] and numerical results of Miller & Bellan [6]. The experiments of Koufapounas *et al.* [7] involved heating beech wood to generate thermogravimetric analysis (TGA) data at a heating rate of 5 and 20 K/min. Miller & Bellan [6] used a similar heating rates in their numerical work, and validated their results against this data. In the current study, a zero-dimensional model of Gypro3D was used to predict both experimental data of Koufapounas *et al.* [7] and numerical results of Miller & Bellan [6]. The reaction R5 was discarded during this validation exercise since the experiments and numerical study did not consider a moist specimen. As seen in fig. 5.3, the residual mass initially for this setup is in reasonably

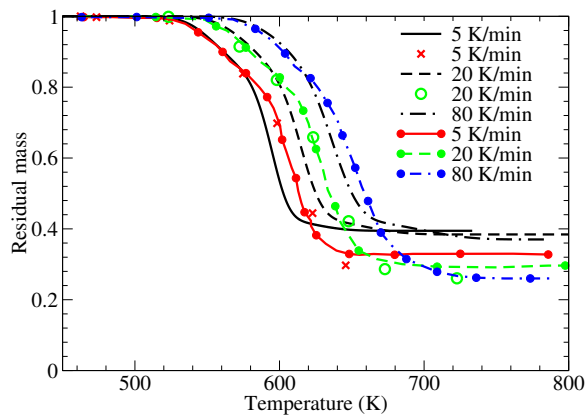

Figure 5.3: Results obtained in the current study (dark line) with simulation results of Miller & Bellan [6] (colored line with symbols) and TGA experimental results of Koufopanos *et al.* [7] (colored symbols) for various heating rates.

good agreement, however at a later time it differed. Our simulations indicated 38% and it was 25% in the experimental and numerical counterpart.

5.5 Results and Discussion

The time history of mass loss rate (MLR) obtained for a case of FMC 76% during the simulation has been compared with its experimental counterpart and is shown in fig. 5.4(a). The FMC chosen here was similar to that used by Pickett *et al.* [8]. The time at which MLR values became positive is treated as the initiation of moisture loss. In case of the simulation, this occurred at $t = 2$s and in the experiments it occurred at $t = 1$s. Two peaks are observed from the simulation results. The initial peak represents the formation of water vapor due to evaporation of free water. The second peak is mainly due to decomposition of virgin reactant giving rise to pyrolysate along with evaporation of bound water. The MLR decreased to zero at $t = 6.5s$ since all the free water was completely evaporated from the fuel. Also, it is observed that

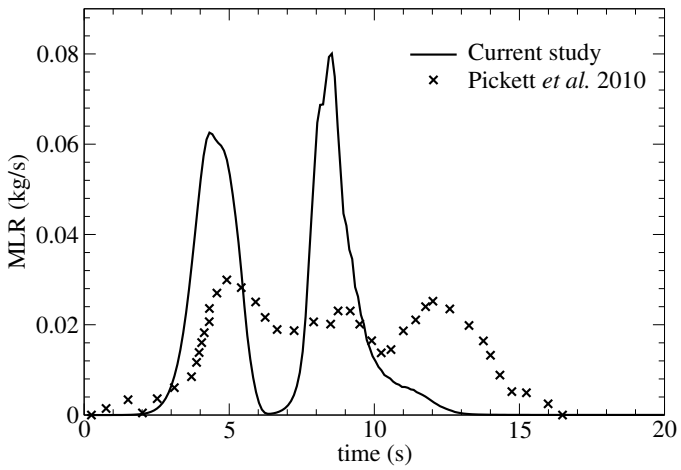

(a)

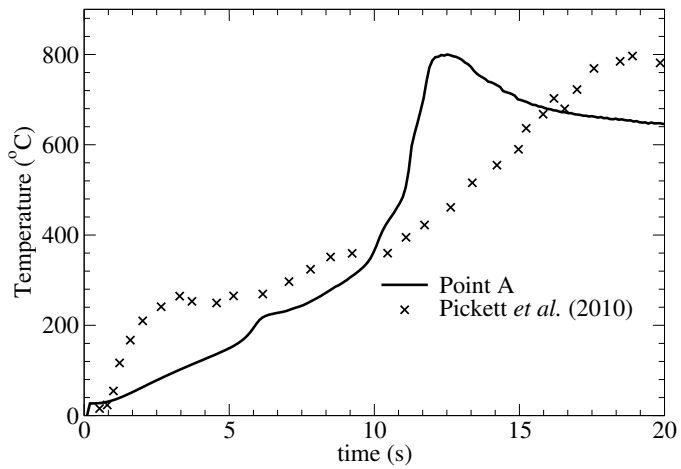

(b)

Figure 5.4: Time histories of (a) mass loss rate, (b) temperature at point A (solid line) with experimental results of Pickett *et al.* [8] (symbols) for an initial FMC of 76%.

the simulation over predicts the experimental data. This overprediction was believed to be due to the difference in initial mass of the solid fuel considered in the simulations and experiments. The initial mass in the numerical simulations was 1g, whereas in the experiments, it was 0.3-0.4g for the data presented here. This discrepancy was driven by computational limitations on the minimum thickness of the solid fuel. In the simulation, the thickness considered was 2mm and in experiments it was in the range

of 0.6-1mm. The time history of solid phase temperature between the simulation and experiments is shown in fig. 5.4(b). In the simulations, this was monitored at point A corresponding to the measurements made in the experiments. As seen, the peak temperature in the simulation was close to 800°C. The time at which this peak occurred differed from experiments as the burn out time in the simulation was close to t =13 s, whereas in experiments it was close to t =15s.

The classical combustion model for a thermally thin fuel particle assumes that all moisture will evolve first from the sample at a temperature near the boiling point of water [20]. Ignition occurs when a combustible mixture of pyrolysis gases is obtained and follows shortly after moisture evaporation is complete [8]. Results from our simulation based on the ignition of a modeled leaf, enabled us to test this assumption. The time history of temperature and mass fraction of free and bound moisture in the simulated fuel were plotted at a fixed point in fig. 5.5 for FMCs of 40, 76 and 120%. Point A as displayed in fig. 5.1, was located on the edge of the solid fuel. As FMC increased, the temperature response decreased; the difference in time was less than 1 second as seen in fig. 5.5(a). This behavior can be attributed to a higher bulk thermal conductivity as the amount of water in the solid fuel increased. Also, from this figure, we observed that ignition occurred when the temperature reached 350-400°C for all the FMC cases. The evolution of mass fraction of free and bound water is illustrated in fig. 5.5(b,c). Moisture loss occurred first in the driest fuel and last in the fuel with the greatest water content; however, the time at which all moisture was evaporated from the different leaves (cases) differed by around 1 second. In case of free moisture, water for all the FMC's evaporated earlier than bound water

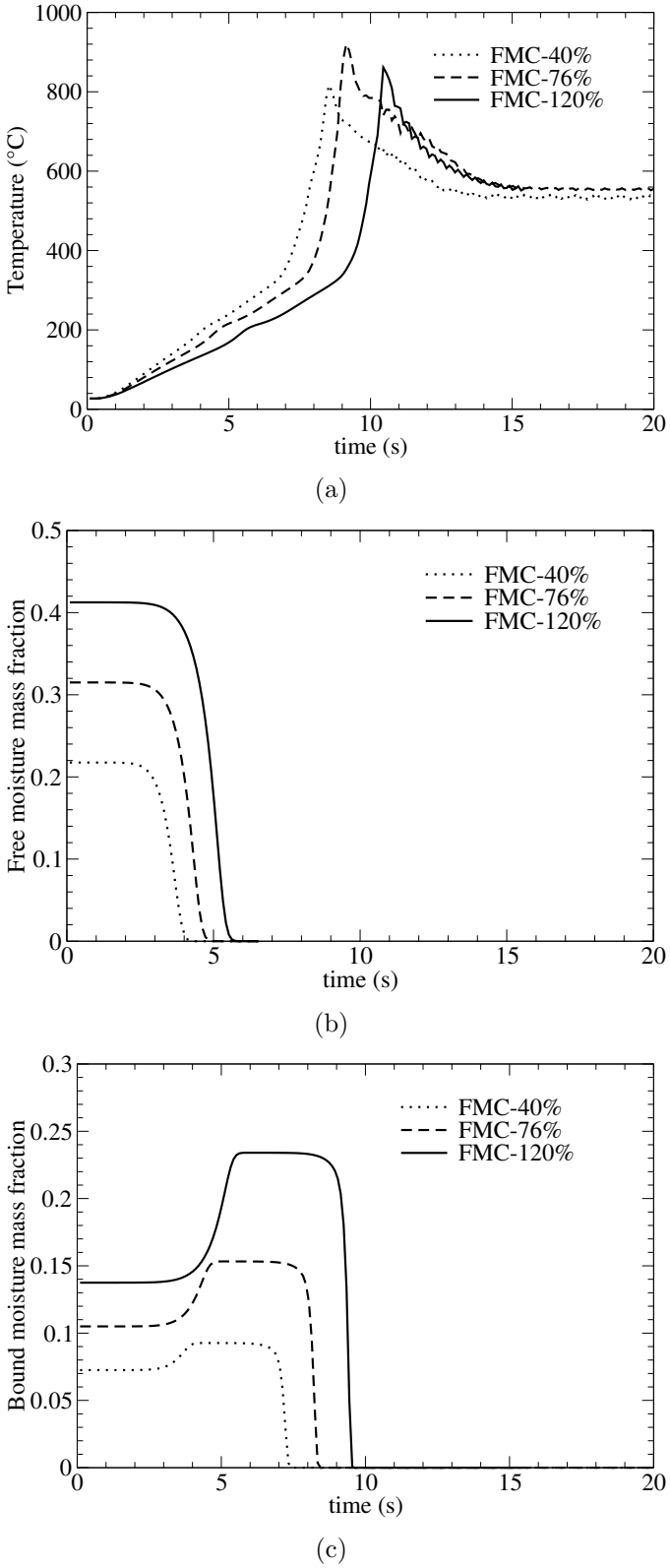

Figure 5.5: Time histories of (a) temperature, (b) free moisture mass fraction and (c) bound moisture mass fraction at point A for three cases with an initial FMC of 40, 76 and 120%.

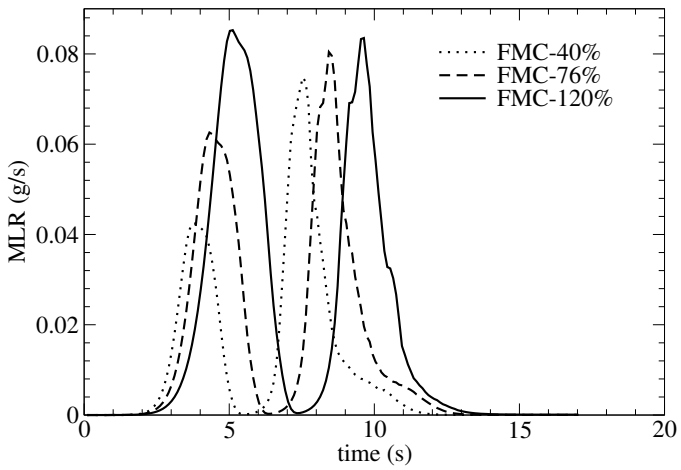

(a)

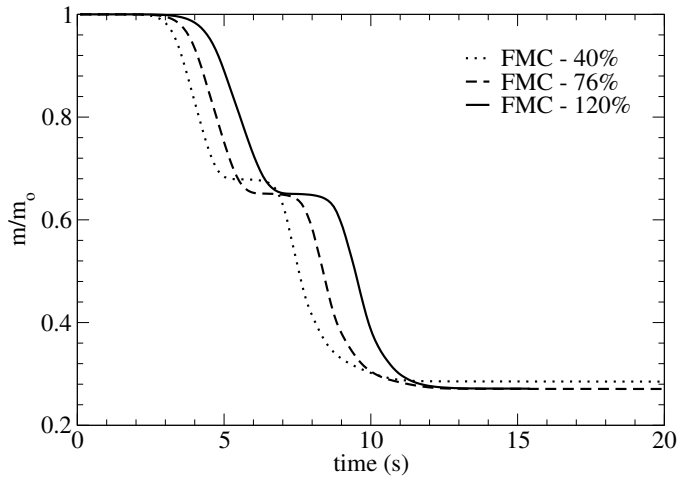

(b)

Figure 5.6: Time histories of (a) mass loss rates, (b) normalized mass for three cases with an initial FMC of 40, 76 and 120%.

and this process occurred before the time of ignition. In case of bound moisture, it is observed that the mass fraction increases slightly, this was a result of evaporation of free water prior to bound water evaporation. Also bound water remained within the solid fuel at the time of ignition.

The evolution of overall mass loss rate (MLR, rate at which gas species are formed from the solid) and normalized mass (by initial wet mass) is shown in fig. 5.6(a)

and 5.6(b), respectively. In fig. 5.6(a), water vapor released by evaporation of free and bound water, and fuel vapor, which is formed from cellulose, hemicellulose and lignin were the species that diffused from the solid phase to the gas phase domain surrounding the solid fuel. The initiation of moisture loss occurred at t =2s for a FMC of 40, 76 and 120%. It is noted that the MLR curves for each of these FMC cases exhibited two overall peaks. The first peak is caused by evaporation of the free water and the second peak is caused by the combined contribution of fuel vapor and water vapor from fuel and bound water evaporation, respectively. The MLR associated with the second peak did not differ greatly between FMC; maximum MLR of the second peak ranged from 0.08 to 0.09 g/s. Oxidation of the gaseous fuel vapors resulted in flaming combustion. Water vapor (from evaporation) and fuel vapor (pyrolyzates from active cellulose) comprised the gas species that diffused from the solid phase to the external gas phase domain. The normalized mass exhibited a similar trend for all three FMCs.

The time histories of overall HRR is plotted in fig. 5.7 for a FMC of 40, 76 and 120%. In fig. 5.7, HRR quantifies the amount of heat generated due to stoichiometric combustion of fuel vapors with oxygen in the gas phase. The fuel vapors were modeled as methane and are assumed to react at stoichiometric proportion with air. The ignition time for 76% FMC case in the simulation was $t = 7$s and in the experimental counterpart it was close to 8s. Also from this figure, it is clear that FMC affected the time at which ignition occurred as the ignition times were $t = 6$, and 8s for FMC of 40, and 120% respectively.

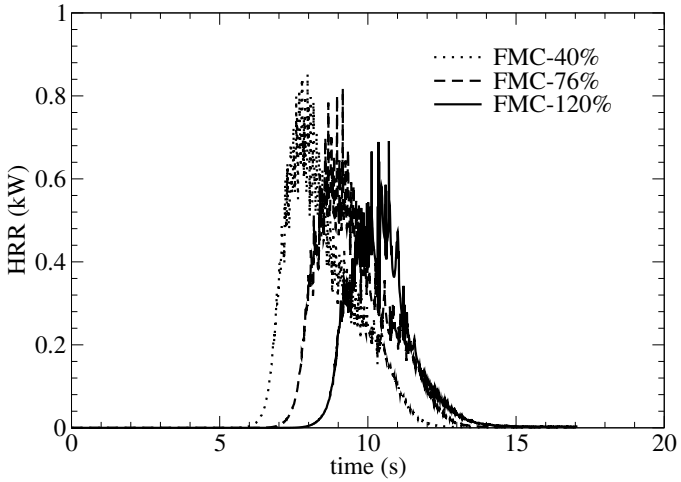

Figure 5.7: Time histories of heat release rates for three cases with an initial FMC of 40, 76 and 120%.

In order to investigate the evolution of moisture in detail, an FMC of 76% was chosen. The solid fuel degradation model, based on the 12-step extended BS mechanism included seven solid and four gas phase species (Eq. R1-R5). Figures 5.8(a,b) illustrates the time history of all solid and gas species at point A, respectively. The conversion of solid species into gas species during thermal decomposition occurred as follows. For solid species, the first degradation reaction occurred near 3 s and accounted for phase transformation of free water to water vapor. An increase in the mass fraction of bound water and the virgin species such as cellulose, hemicellulose and lignin occurred (fig. 5.8a) as the mass of moisture was removed from the solid phase. Shortly after this, as the temperature of the solid fuel increased, the virgin species converted to active state which then later broke down to char, fuel vapors, and tar. Char remained as a residual species in the solid fuel, not going through further degradation. In fig. 5.8(b), water vapor was formed in the condensed phase

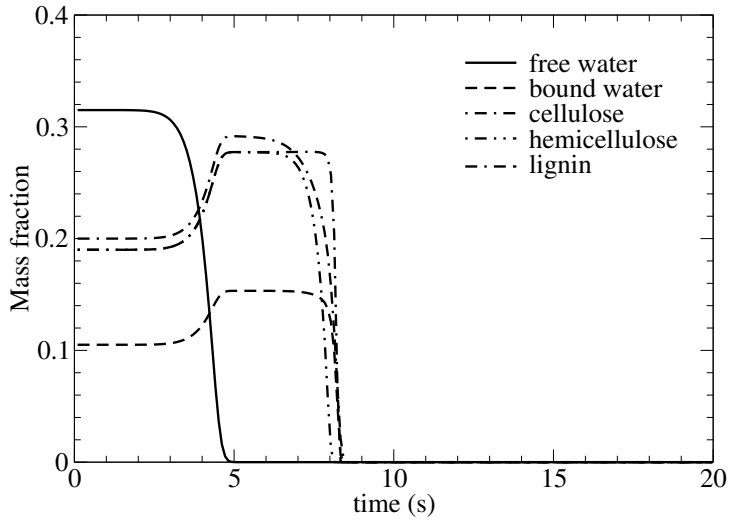

(a)

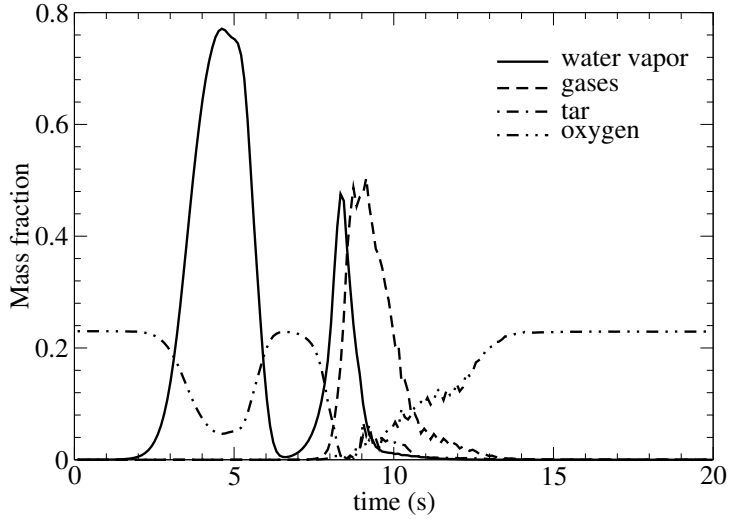

(b)

Figure 5.8: Time histories of (a) solid species and (b) gas species within the solid fuel at point A for a FMC of 76%.

due to both free water and bound water evaporation. The first peak is due to free water followed by the second peak due to bound water evaporation. It is noted that fuel vapors began to evolve at $t = 7.5s$ before the diffusion of water vapor. The fuel vapors that are diffused later into the gas phase domain at 7.5 s, resulted in ignition caused by reaction with oxygen. The time history of mass fraction of oxygen within the solid exhibited an unusual behavior: Initially when the mass fraction of water vapor increased during evaporation of free water, the oxygen mass fraction reduced correspondingly in fig. 5.8(b). Later when water vapor was formed at the second peak along with fuel vapors, mass fraction of oxygen decreased. The initial reduction of oxygen within the solid fuel was due to the reduction of oxygen in the gas phase external to the solid fuel. The reduction of oxygen in turn occurred as a result of presence of water vapor in the gas phase domain, which displaced the available oxygen around the solid fuel. Oxygen was reduced at later times due to the presence of products of combustion and water vapor from bound water. Tar cracking also consumed oxygen; however, it eventually diffused back into the condensed phase from the external gas phase domain.

The spatial variation of bound water mass fraction within the solid fuel is plotted along an xy slice at different time instants $t = 7, 7.3$ in fig. 5.9(a,b). From this figure we observe that at the time of ignition, the solid fuel still contained a large quantity of bound moisture. In fig. 5.9(a), a drying front propagated from the edges traveling towards the center over time along y direction. Later as seen in fig. 5.9(b) this drying front, propagated along x direction towards the edges from the center of the solid fuel. Evaporation occurred at the edges and center of the solid

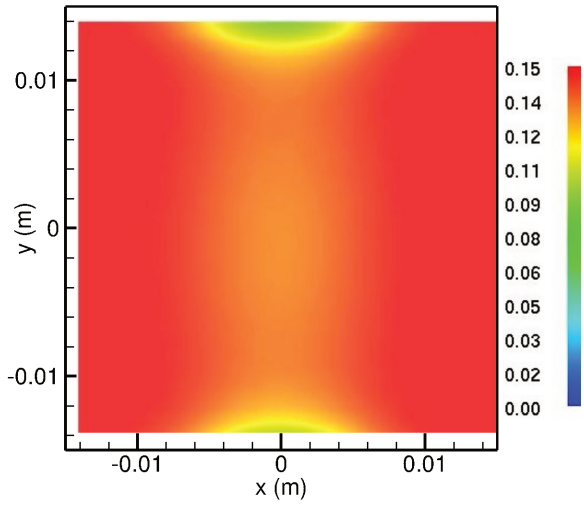

(a)

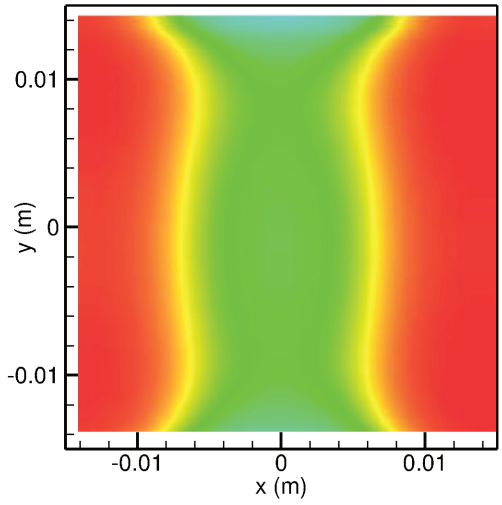

(b)

Figure 5.9: Contours of bound water mass fraction in the solid fuel at (a) $t = 7$ s (b) $t = 7.3$ s on an xy-slice located at $z = 0.051$ m for a case with an initial FMC of 76%.

fuel at a higher rate than the other regions. This was a result of non-uniform heating which arose due to the formation of vortices above the surface of the solid fuel. These vortices were a result of the convective flow of hot gases from the burner located below the solid fuel. Discussion related to the presence of vortices is presented in the later part of this Section.

Two-dimensional contours of temperature, mass fraction of water vapor and oxygen are plotted in the gas phase along an xz slice located at $y = 0$ for a FMC of 76% as shown in figs. 5.10(a-c) at $t = 3$s. Heated air exits the burner and it encounters the solid fuel along the path as shown in fig. 5.10(a). The solid fuel acts as an obstruction causing flow separation. As a result of this, vortices are generated above the solid fuel which are later convected out of the computational domain. These vortices formed above the solid fuel surface deviate the path of hot gases thus lowering the temperature in that region as can be observed in fig. 5.10(a). Figure 5.10(b) shows water vapor generated around the solid fuel close to the edges as a result of free moisture evaporation. Free moisture is converted to water vapor before the initiation of gas phase ignition due to its low activation energy. As the water vapor is released into the gas phase domain and transported, it displaces the available oxygen around the solid fuel thus lowering its mass fraction. This effect can be seen from fig. 5.10(c) where the mass fraction of oxygen is lowered at the edges of the solid fuel. As the oxygen at this instant is reduced in the gas phase, it also reduces within the solid fuel as discussed in fig. 5.8(b).

Two-dimensional contours of temperature, mass fraction of water vapor and oxygen are plotted in the gas phase along an xz slice located at $y = 0$ for an FMC

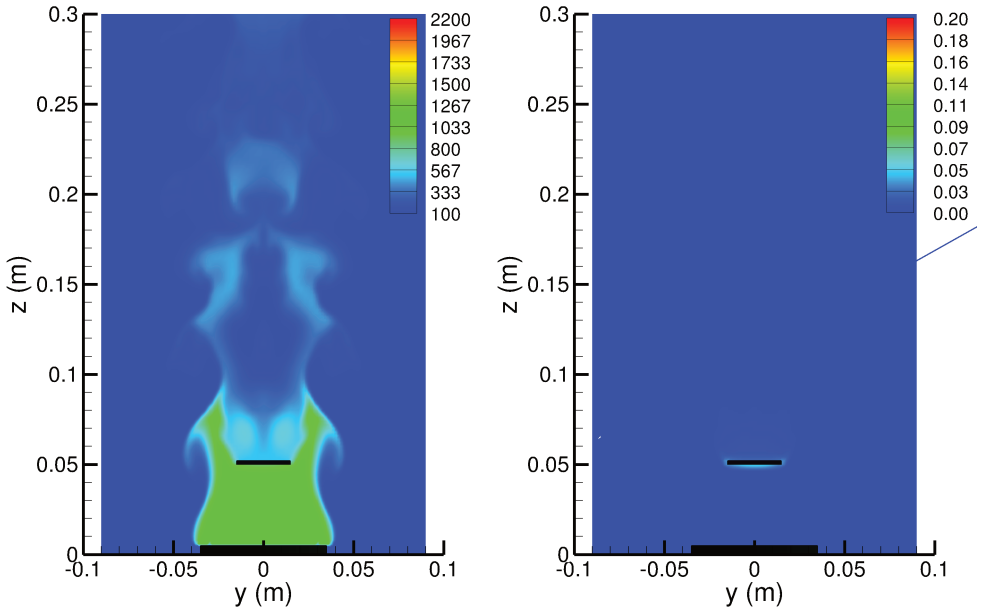

(a) (b)

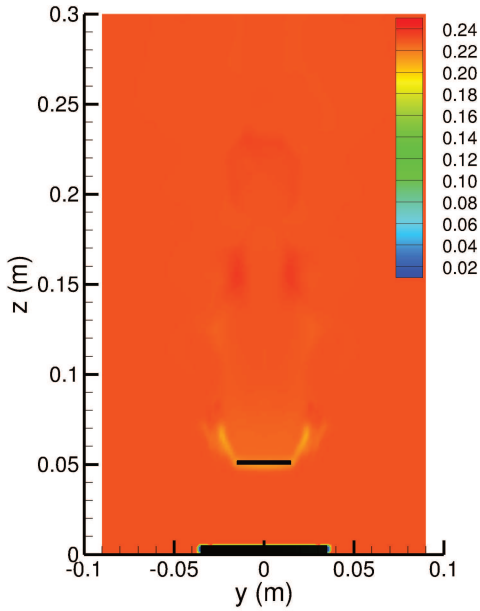

(c)

Figure 5.10: Color contours of (a) temperature (b) mass fraction of water vapor and (c) oxygen mass fraction in the gas phase at t =3 s on an xz-slice located at y =0 for a case with an initial FMC of 76%.

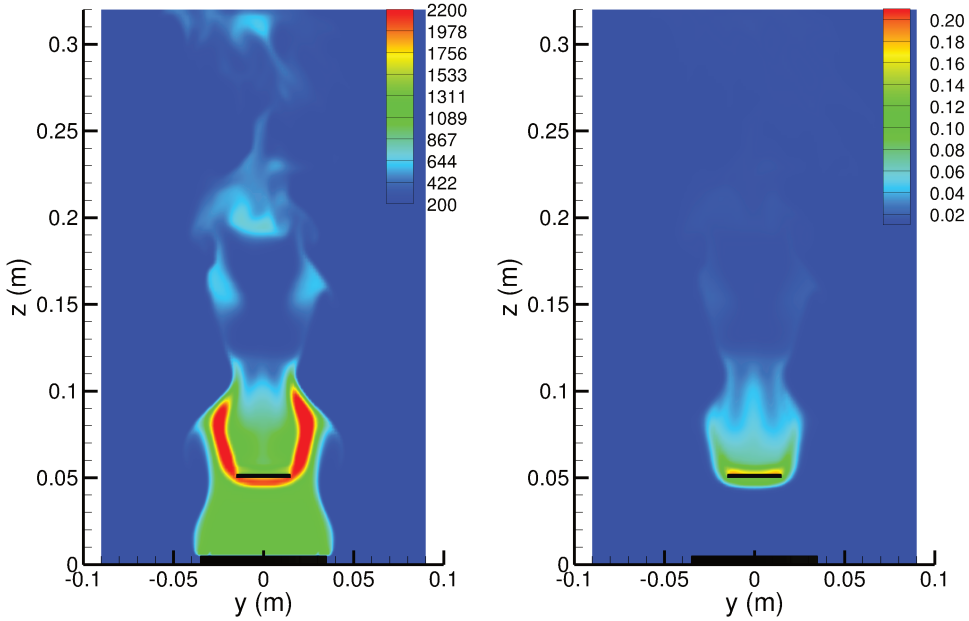

(a) (b)

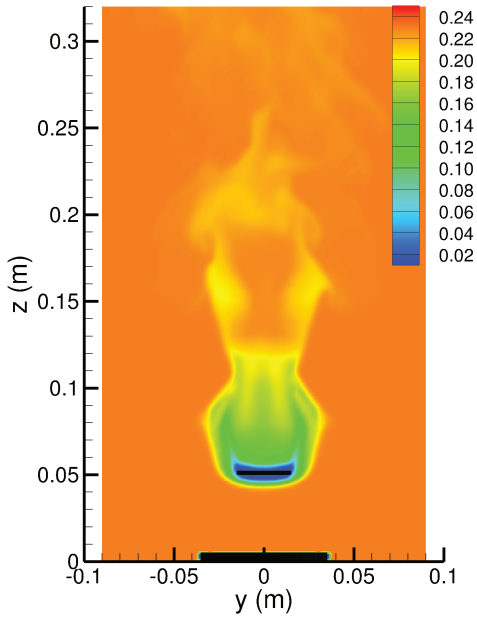

(c)

Figure 5.11: Color contours of (a) temperature (b) mass fraction of water vapor and (c) oxyegn mass fraction in the gas phase at t =8 s on an xz-slice located at y =0 for a case with an initial FMC of 76%.

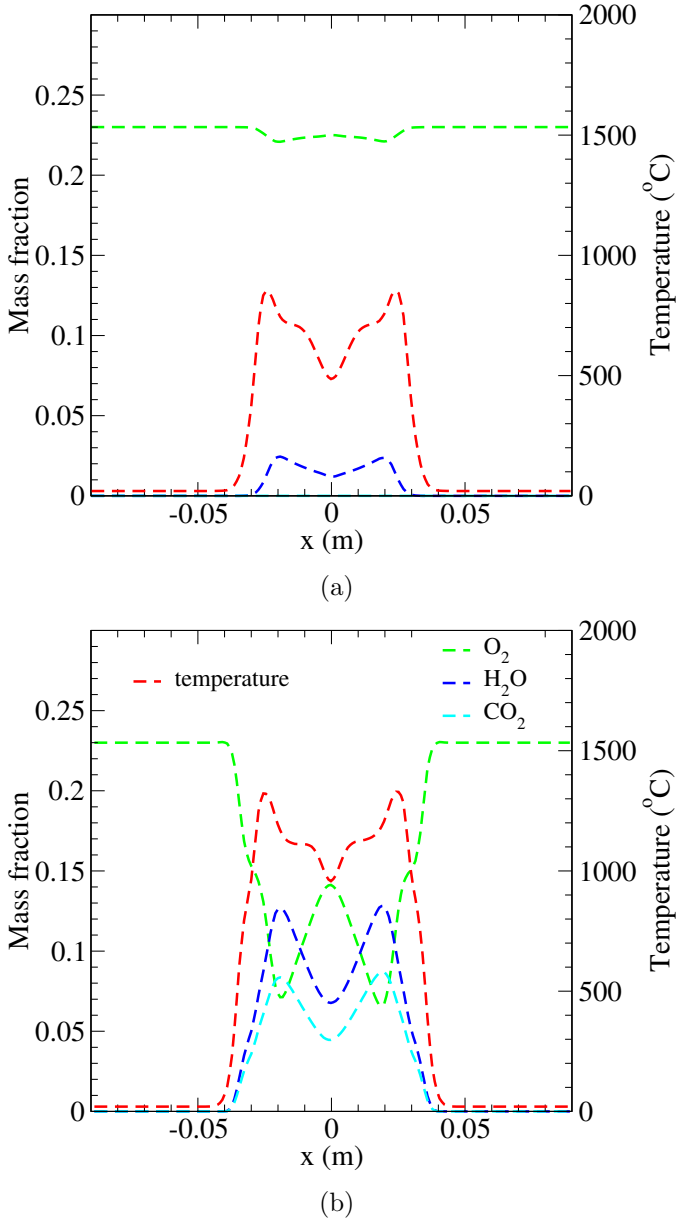

Figure 5.12: Variation of mass fraction of tracked gas species at time (a) 3 s (b) 8 s along x at $y = 0$ and $z = 0.06$ m in the gas phase domain for a case with an initial FMC of 76%.

of 76% as shown in figs. 5.11(a), (b) and (c) at $t = 8$s. The solid fuel at this instant had ignited, therefore the temperatures in the vicinity of the solid fuel were high as illustrated in fig. 5.11(a). The periphery of the solid fuel ignited prior to the center since only edges were exposed to the hot gases. Following this in fig. 5.11(b), high mass fraction of water vapor was observed close to the periphery compared to the center of the solid fuel. The water vapor here is formed due to the evaporation of bound moisture as well as combustion. As shown in fig. 5.9, bound water was still evaporating within the solid fuel. From this observation, it is clear that the bound moisture evaporation front followed the free moisture evaporation during the ignition process. This simulation indicates that the evaporation and ignition processes occur together in live fuels and are consistent with the experimental findings of Pickett *et al.* [8].

As described by Byram [114], water vapor in the combustion environment arises from two sources–evaporation of water contained in the fuel and water produced by the combustion reaction. The mass fractions of H_2O, CO_2, O_2 and temperature immediately above the solid fuel were plotted along x direction in the gas phase at time instants $t = 3, 8$s in fig. 5.12. At time 3 s in fig. 5.12 (a), it was observed that the temperature at the edges of the solid fuel, $x = -0.015, 0.015$m, was higher by 250 ^{o} C, compared to the center, $x = 0$. Also we observe that at the region where H_2O is high, O_2 is displaced, reducing its mass fraction. At time 8 s in fig. 5.12 (b), when the solid fuel underwent ignition, H_2O is formed as a result of combustion in addition to evaporation of bound water. Moreover, CO_2, the other product of combustion follows a similar trend with respect to H_2O. From this figure, O_2 is deficient in the reaction

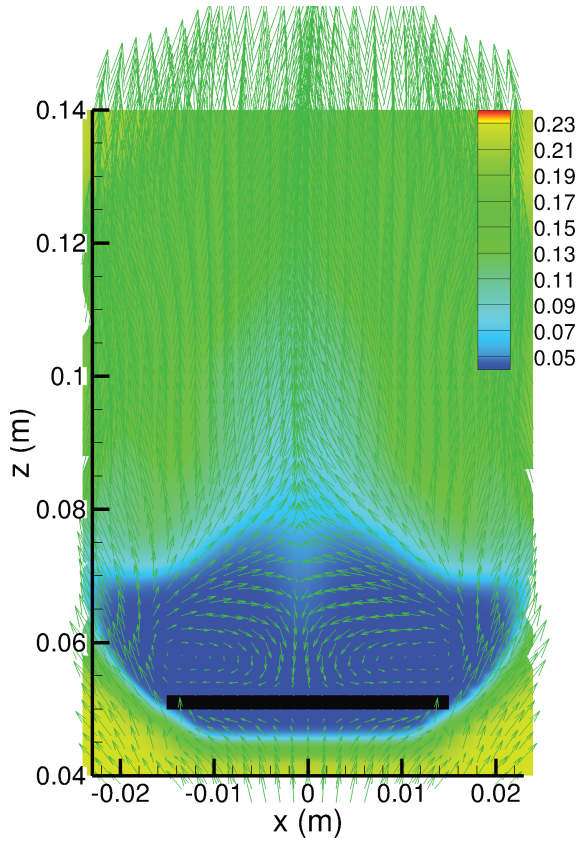

Figure 5.13: Contours of oxygen mass fraction and velocity vectors along an xz slice at $y = 0$for a case with an initial FMC of 76%.

zone due to two reasons– consumption during combustion and displacement by water vapor. However the mass fraction of O_2 is high at the center of the solid fuel in the gas phase.

As discussed in fig. 5.10, heated air exits the burner and as it encounters the solid fuel along the path, it undergoes flow separation. Due to this effect, vortices are generated above the solid fuel which are later convected downstream. Two-dimensional contours of oxygen mass fraction and velocity vectors has been plotted along an xz slice at $y = 0$ in fig. 5.13. This figure illustrates the vortex formation

above the surface of the solid fuel. As shown, the axis of vortex is parallel to y direction. The vortex affects the distribution of species such as CO_2, and H_2O above the surface of the solid fuel due to both evaporation and combustion. Since a vortex is essentially a low pressure region, it displaces the species from the center $x = 0$m, to edges $x = -0.015, 0.015$m. This displacement explains the reason for the appearance of two peaks in the profiles of products of combustion at edges in fig. 5.12(b). As the products of combustion are displaced from the center, oxygen diffuses into this region, creating a peak in the mass fraction value as observed in fig. 5.12(b). Oxygen present in this region aids flame spread in y direction from the edge towards the center as discussed before in fig. 5.9(a).

Figure 5.14 shows the relative contribution of the convective and radiative heat transfer in igniting the solid fuel particle. The positive convective heat flux observed during the initial time $t = 0$ to 5s in fig. 5.14(b), accounts for the energy absorbed by solid fuel due to the external heat source in the gas phase. Later when the solid fuel ignites, at peak MLR ($t = 9$s) it radiates and convects energy back to the gas phase which results in negative heat flux as seen from the figure 5.14(a).

HRR iso-surface of 26 kW/m^3 at $t = 9$s, (during the peak MLR) in the gas phase as shown in fig. 5.15. This value was chosen since it was a peak value at this instant of time. It is observed that when the entire solid fuel is burning, the edges burn vigorously than the rest of the fuel. It is important to note that in case of experiments, the leaves tested could have non-homogeneous distribution of moisture content initially, or there may be variation in thickness *i.e.* the center of the fuel could be thicker/thinner compared to other region. These factors in addition to the effects

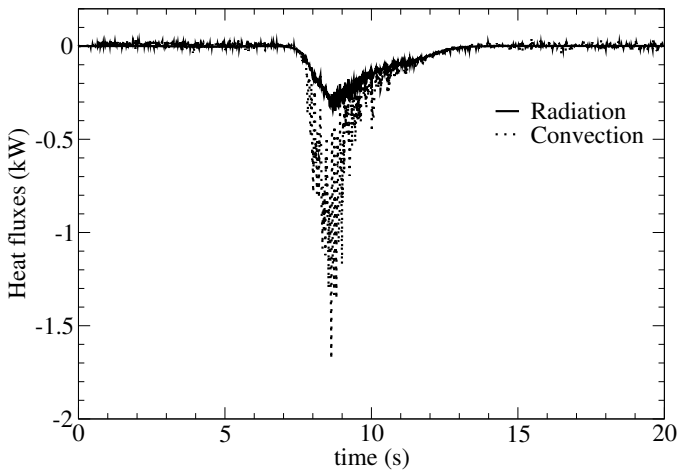

(a)

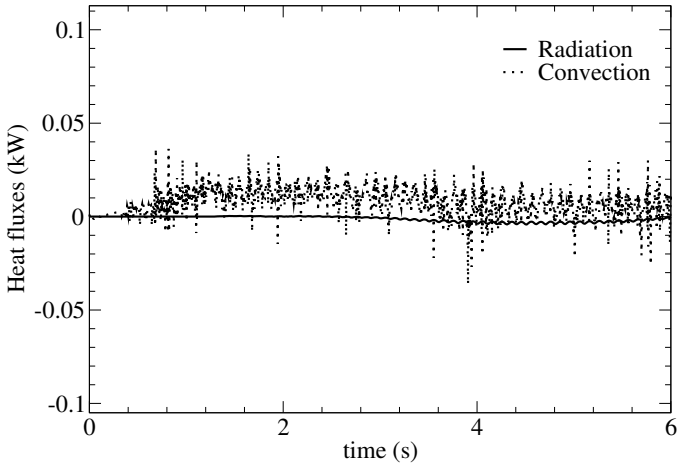

(b)

Figure 5.14: (a)Time history of global radiation and convection fluxes for a case with FMC of 76%. (b) Close up of the figure during the initial preheating stage. Positive heat flux means heat is transferred from gas to solid particle and negative heat flux means vice versa.

of fluid dynamics simulated in this study, can also influence the heating pattern as discussed by Prince *et al.* [44].

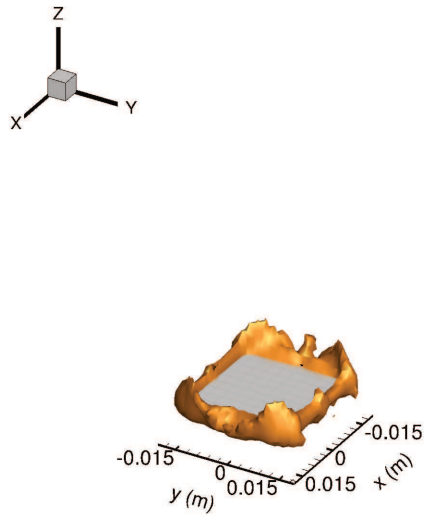

Figure 5.15: Iso-surface of heat release rate (HRR) at $t = 9$s for a case with an initial FMC of 76%.

5.6 Chapter Summary

The effect of moisture states on pyrolysis and ignition of a thin solid fuel particle subjected to convective heating has been investigated. An advanced 12-step thermal degradation reaction mechanism used was initially validated with other TGA experiments and numerical simulation. Later using the three dimensional computational model, it was compared with the experimental data obtained using the FFB apparatus. The simulations were consistent with the experimental results in terms of ignition and burnout time prediction, fire initiation and spread pattern. A FMC of 40, 76 and 120% was considered to study the effect of moisture content. The temperature response and thermal degradation rate was higher for the case with 40% FMC and ignition occurred prior to the 120% FMC case. Local evaporation of moisture and temperature rise at the periphery of the solid fuel was observed, also a significant

amount of moisture remained in the sample at the time of ignition. Free water completely evaporated from the solid fuel before igntion, however bound water remained within the solid fuel at the time of ignition.

CHAPTER 6

VERTICAL FUEL CONFIGURATION: INVESTIGATION OF THE EFFECT OF HEATING MODES

6.1 Introduction

In the previous chapter, we investigated the effects of moisture content on ignition behavior of an individual leaf-like fuel oriented horizontally when subjected to convective heat transfer. The focus in this Chapter is to investigate the flame spread pattern on a vertically oriented fuel element that is exposed to both convective and radiative heat transfer.

During a wildfire, the leaves of live fuel species such as manzanita (Arctostaphylos glandulosa) are oriented at various positions. Prior to combustion, most leaves are oriented upwards within 45° of vertical [44]. Before and after ignition, leaves pivot on their stems, extending first horizontally, away from their associated branch, and frequently continue downward. As the leaves burn out, they typically recoil partway to their original position. This behavior is likely to occur because the outward face of the stem is exposed to heating, and thus dries, burns and contracts ahead of the shielded, inward face of the stem. Horizontally-oriented leaves are a good representation of the average position of leaves during the majority of the combus-

tion process as investigated in detail in Chapter 4 and 5. However, vertically-oriented leaves best describe the early stages of heating and combustion which is the focus of this Chapter.

For no-wind/ low-wind conditions as discussed in Chapter 1, radiation was the dominant heating mode. In case of high wind conditions, convection-based modeling seems appropriate to predict fire spread in highly wind-driven fires. There could also be conditions where both heating transfer modes influence the ignition and fire spread.

The main aim here is to investigate the effects of combined heating modes and moisture content on pyrolysis and gas phase combustion of an individual live leaf oriented vertically. Results obtained from the numerical simulations for a fuel moisture content (FMC, dry basis) of 44, 65, and 90% are reported. The solid phase model uses Gpyro3D [74] for pyrolysis and the gas phase fluid dynamics and ignition are solved by FDS [9, 117]. A detailed description of mathematical models with main assumptions and governing equations used in Gpyro3D and FDS are given in Chapter 2. In this Chapter, ignition is defined to be the time at which the heat release rate (HRR) exceeded 200 kW/m^3 in the gas phase.

6.2 Computational Setup and Model

Combustion experiments were performed by Prince *et al.* [44] on freshly harvested manzanita (Arctostaphylos glandulosa) oriented vertically in the flat flame burner (FFB) apparatus. Video images, mass and temperature data were collected for various FMC of the fuel. Convective and/ radiative heat source were used in or-

der to investigate the effect of heating modes on ignition. A considerable amount of temperature and moisture variation was observed along the surface and depth of the fuel, indicating the three-dimensional nature of pyrolysis. The computational domain and the kinetic model discussed below mimics this setup to model the ignition and subsequent burning of the fuel.

The experimental setup and the computational domain used are shown in fig. 6.1(a, b). The solid fuel element has dimensions of $0.03 \times 0.002 \times 0.03$ m for Length $\times$ Width $\times$ Thickness. The computational domain used for the gas-phase solver FDS is a rectangular cube of size $0.18 \times 0.25 \times 0.32$m. The gas phase grid resolution used in x, y and z directions is $120 \times 160 \times 216$, respectively. The solid fuel particle is oriented vertically and is centered in the gas-phase domain located at $z = 0.055$m in the computational domain. The initial temperature, moisture content, pressure, gaseous species mass fractions, and condensed phase species are uniform throughout the solid. The fuel element is simulated as a separate region modeled by Gpyro3D with a grid spacing of 0.0006 m in x and y directions and 0.0003 m along the depth, resulting in 9600 grid cells. The fuel element for convection-only case is exposed to a modeled burner with a dimension of 0.18×0.25 m, L $\times$ W from which heated air enters the domain at 1000^oC and at a velocity of 0.6 m/s. In case of combined heating mode, it is exposed to a heated wall with dimensions 0.18×0.32 m, L $\times$ W providing 50 kW/m^2 (750K) input/initial heat flux. The center of the solid fuel is located 5 cm above the top surface of the burner and is 11 cm from the heated wall, surrounded by solid walls on the sides with the top surface being open. Initially, the condensed/solid-phase domain consists of moisture, cellulose, hemicellulose, and

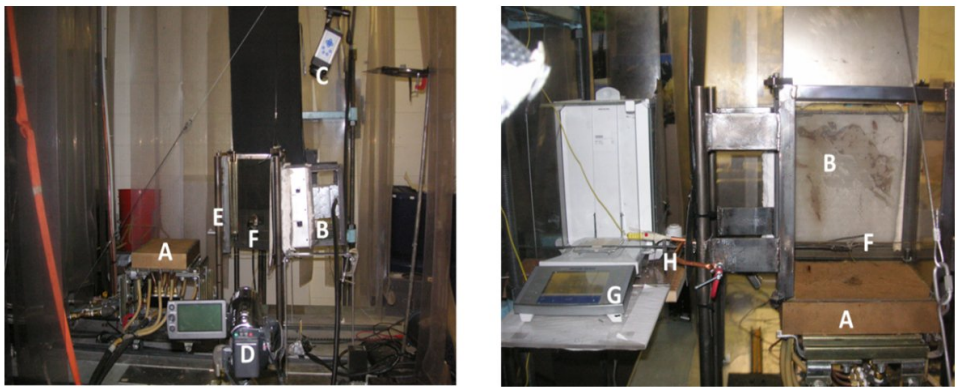

(a)

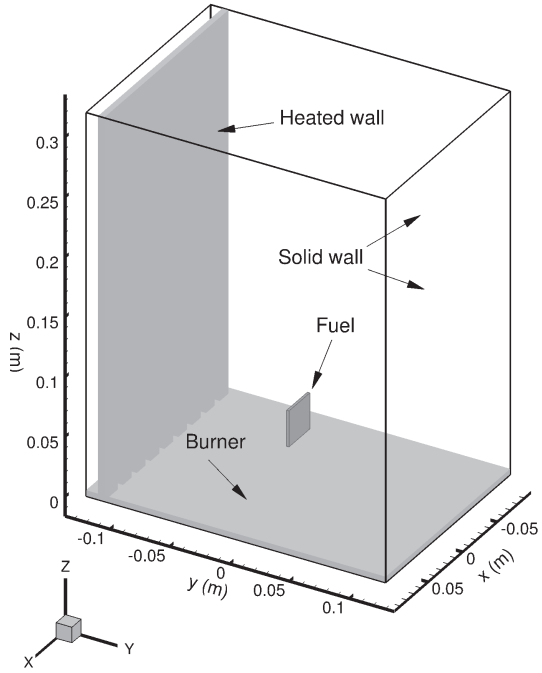

(b)

Figure 6.1: Figure 1: (a) Experimental apparatus: flat flame burner (A), radiant panel (B), IR camera (C), video camera (D), glass cage to prevent ambient air entrainment (E), sample location (F), mass balance (G) and sample holding rod (H); (b) Isometric view of computational domain showing a thin solid fuel subjected to combined convection and radiation surrounded by solid wall.

lignin. The gas phase within the solid fuel consists of standard air (nitrogen and oxygen). Their respective initial mass fractions are given in Table 6.1.

Table 6.1: Initial mass fractions

FMC	Free moisture	Bound moisture	Cellulose	Hemicellulose	Lignin	N_2	O_2
44%	0.225	0.075	0.23	0.23	0.24	0.77	0.23
65%	0.3	0.1	0.198	0.198	0.204	0.77	0.23
90%	0.3525	0.1175	0.17	0.17	0.19	0.77	0.23

The initial mass fraction of other species were considered negligible. The initial gas species in the FDS domain was standard air. The initial temperature was set to an ambient temperature of 300 K both within the solid as well as the external gas phase domain. The 12-step reaction model discussed in Chapter 5 has been incorporated in Gpyro3D. This reaction scheme accounts for two evaporation reactions for moisture evolution based on free and bound state along with decomposition kinetics for cellulose, hemicellulose and lignin. The thermophysical properties were assumed identical for cellulose, hemicellulose and lignin [6]. Thermal conductivity and specific heat capacity are temperature dependent and modeled using correlations for soft wood species [130]. These correlations were used for the solid species for all the simulations invoking the coupled solver with various FMC's (44, 65 and 90%). The properties for the gas species were assumed from the available data for air. In the external gas phase domain, the pyrolysate released from the solid was modeled as methane and it underwent stoichiometric combustion with oxygen.

All the computations discussed above were performed using the message passing interface (MPI) protocol on 60 processors of Dense Memory Cluster (DMC) lo-

cated at Alabama supercomputer Authority. A typical simulation of 10 seconds of burning required a wall time of 48 hours and 120 GB of memory.

6.3 Results and Discussion

The 12-step kinetic model used in the numerical simulations was initially validated against the experimental and simulation data of Koufopanos *et al.* [7] and Miller & Bellan [6], respectively, using a zero-dimensional model of Gypro3D. Details of this validation exercise are discussed in Chapter 5. Using the convection-only heating case shown in fig. 6.1(b), the effect of FMC on solid and gas phase ignition is discussed, followed by the effect of combined convection and radiation by incorporating the heater into the computational setup (fig. 6.1b). During this discussion, computational results were also compared with the experimental data obtained using the FFB burner. Although more detailed results pertaining to the experimental data could be obtained elsewhere [44], a global result comparison with mass loss rate was presented here for the purpose of numerical validation.

6.3.1 Convection-only Heating

The time history of mass loss rate (MLR) obtained at an FMC of 65% has been compared with its experimental counterpart in fig. 6.2.

The time at which MLR becomes positive can be treated as the time of initiation of moisture loss. In case of simulations, this occurred at 1.8s and in experiments, it occurred much earlier, at 0.5s. It is further observed that the simulation over predicts the peak experimental mass loss rate. This over prediction is believed to be due

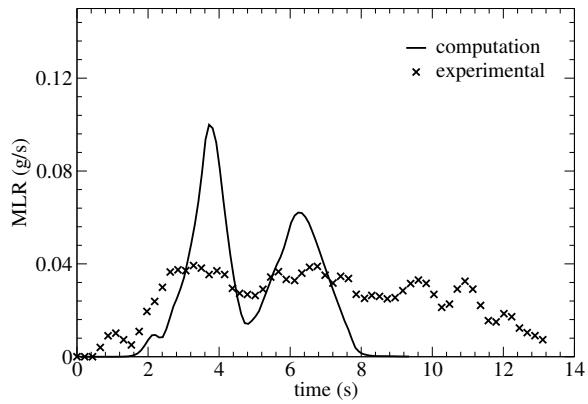

(a)

Figure 6.2: Comparison of time histories of mass loss rate (solid line) with experimental results of manzanita species (symbols) for an initial FMC of 65% using convection-only heating.

to the larger initial mass of the solid fuel considered in the simulations. The initial mass in simulations was 1g whereas it was 0.38g in the experiments; this discrepancy was driven by computational limitations on the minimum thickness of the solid fuel. In the numerical simulations the solid fuel thickness was 2mm while the thickness of manzanita leaves in the experiments was measured between 0.5 and 1mm. The computational model was utilized to study the process leading up to ignition in detail.

The time history of temperature and mass fraction of free and bound moisture in the simulated fuel at a fixed point is plotted in figure 6.3 for FMCs of 44, 65 and 90%. This point is located on the leading edge of the solid fuel at $x = y = 0, z =$ 0.04m. At higher FMC, temperature response is delayed; the difference in time was less than 1 second (fig. 6.3 a). This behavior is attributed to a higher bulk thermal conductivity as the fraction of water in the solid fuel is increased. Also from this figure, it is evident that ignition occurrs when the temperatures reaches 450-500°C

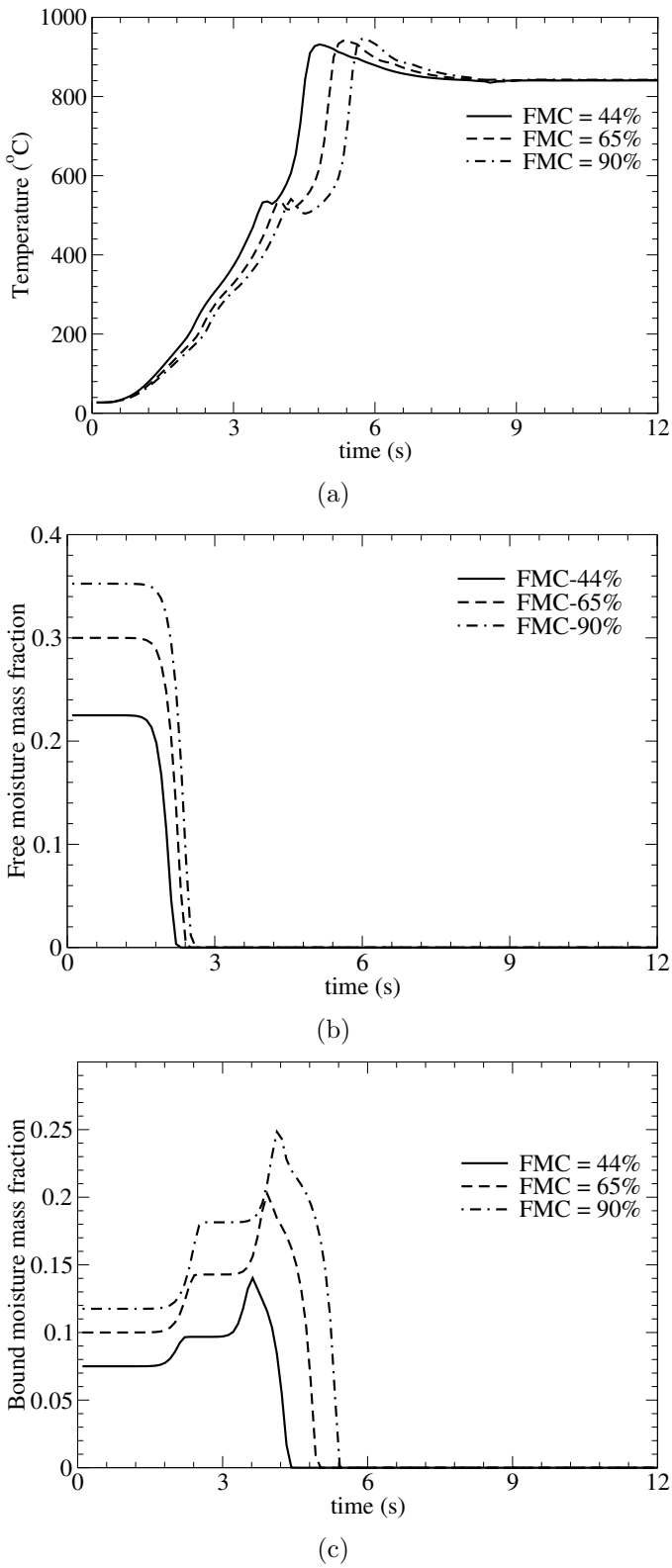

Figure 6.3: Time history of (a) temperature, and (b) mass fraction of free moisture (c) mass fraction of bound moisture at a point $x = y = 0, z = 0.04$m (see fig. 6.1) for three cases with an initial FMC of 44, 65 and 90%.

at all FMC's investigated. The evolution of mass fraction of free and bound water is seen in fig. 6.3(b, c). Moisture loss occurred first in the driest fuel and last in the fuel with the greatest water content. In case of free moisture, water for all the FMC's evaporated earlier than bound water and this process occurred before the time of ignition. The mass fraction of bound water increases slightly at $t = 2,3$s as a consequence of evaporation of free water and degradation of other solid species. Complete moisture loss occurrs first in the driest fuel and later in the fuel with the greatest water content; however, the time at which all moisture is evaporated from the different leaves (cases) differed roughly by 1 seconds.

The evolution of overall MLR and HRR is plotted in fig. 6.4 for FMCs of 44, 65 and 90%. From fig. 6.4(a), it is seen that initiation of moisture loss occurrs at 1.9s at all FMCs. It is noted that the MLR curves for each of these FMC cases exhibit two overall peaks. The first peak is caused by evaporation of the free water and the second peak is caused by the combined contribution of fuel vapor and water vapor from fuel degradation and bound water evaporation. Oxidation of the gaseous fuel vapors resulted in flaming combustion. In fig. 6.4(b), HRR quantifies the rate of heat generation due to combustion of fuel vapors in the gas phase. For the 65% FMC case, ignition time was 3.3s in simulations while it was 3.1s in the FFB experiments. The ignition times were 3.2s and 3.4s for the other FMC's of 40 and 90% investigated. Although the ignition times for various moisture contents were close to each other, there was a significant difference in the time at which HRR achieved the peak value.

The 65% FMC case was investigated in greater detail. The solid fuel degradation model, based on the 12-step extended BS mechanism included seven solid and

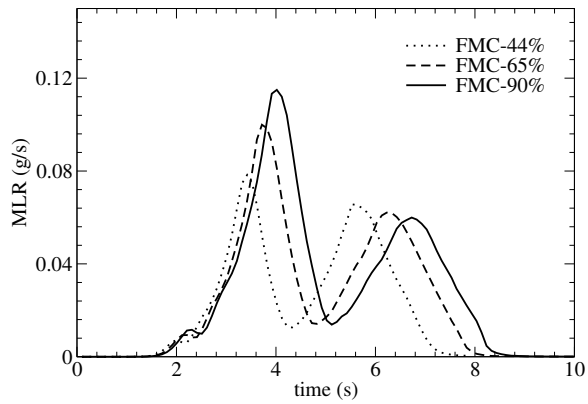

(a)

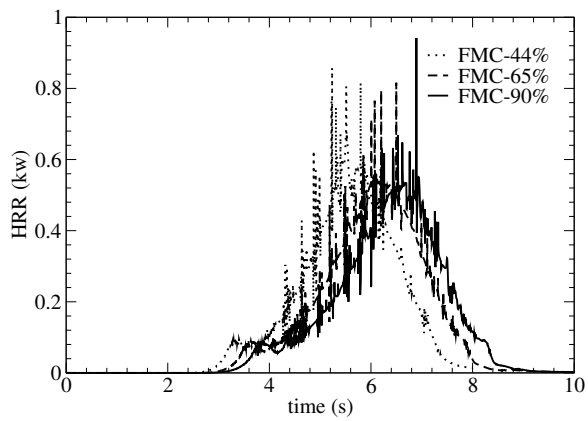

(b)

Figure 6.4: Time history of (a) mass loss rate and (b) heat release rate in the solid phase for three cases with an initial FMC of 44, 65 and 90%.

four gas phase species. Fig. 6.5(a) and (b) illustrates the time history of all solid and gas species at the leading edge ($x = y = 0, z = 0.04$m) of the solid fuel, respectively. In case of solid species, the first degradation reaction occurred around 2 s and accounted for phase transformation of free water to water vapor. An increase in the mass fraction of bound water and the virgin species such as cellulose, hemicellulose and lignin occurred, as the free water was removed from the solid phase. Shortly thereafter, the temperature of the solid fuel increases, the virgin species converted to active state which then later broke down to char, fuel vapors, and tar. Char remained

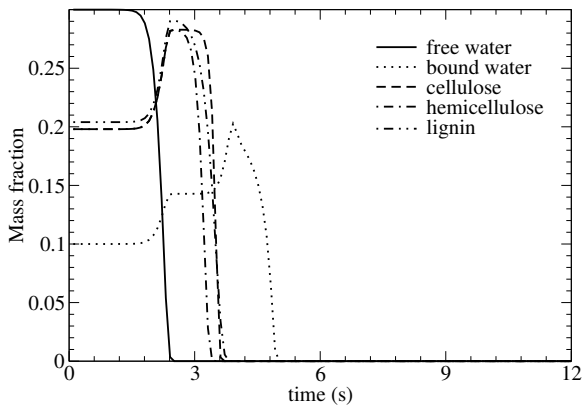

(a)

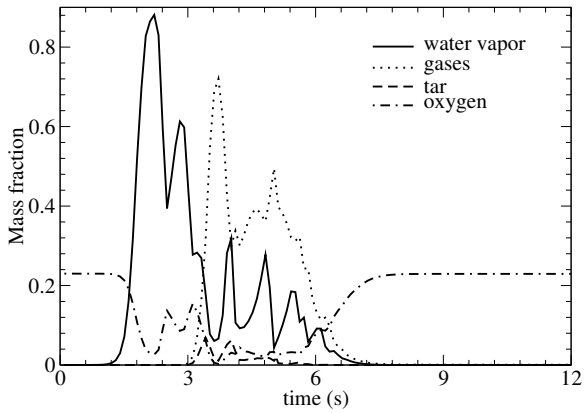

(b)

Figure 6.5: Time history of (a) solid species and (b) gas species within the solid phase for a case with an initial FMC of 65% at point $x = y = 0, z = 0.04$m.

as a residual species in the solid fuel and did not undergo further reaction. In fig. 6.5(b) note that water vapor is formed in the solid due to both free and bound water evaporation. The curve exhibits multiple peaks, where the first peak is due to free water followed by the bound water evaporation. Fuel vapors began to evolve even before the water vapor diffused out. The fuel vapors which are later diffused into the gas phase domain at 3 s resulted in ignition due to reaction with oxygen (fig. 6.4). Also from this figure, the time history of mass fraction of oxygen at the leading edge exhibited unusual behavior. Initially when the mass fraction of water vapor increased

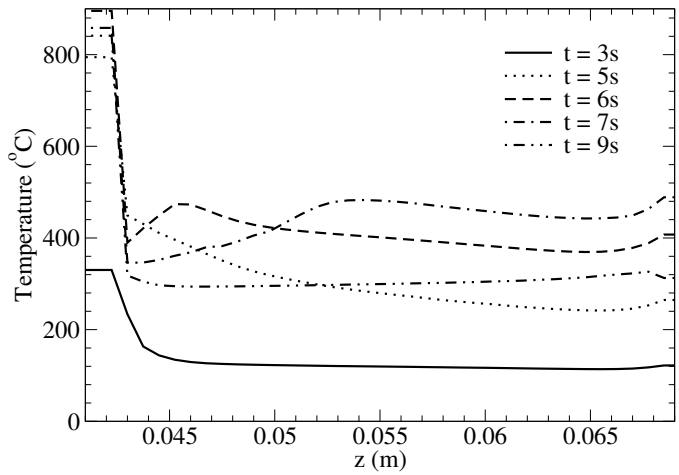

Figure 6.6: Variation of temperature along length of the solid fuel, z at $x = y = 0$ at various time instants for a FMC of 65%

during evaporation of free water, the oxygen mass fraction reduced correspondingly. Later when water vapor was formed as a result of bound water evaporation along with fuel vapors, oxygen was reduced again. The initial reduction in oxygen within the solid fuel was due to the reduction of oxygen in the gas phase external to the solid fuel. This occurs due to the presence of water vapor during evaporation in the gas phase where it displaces the oxygen around the solid fuel. As a result of this, oxygen within the solid diffuses out thereby causing reduction in its mass fraction. Later in time, oxygen mass fraction within the solid fuel decreased due to the formation of products of combustion in the FDS domain. Tar cracking also consumed oxygen; however, oxygen eventually diffuses back into the solid from the external gas phase domain after the fuel was burnt out.

The variation of temperature along the length of the solid fuel at various time instants is shown in fig. 6.6. At time $t = 3$s, the leading edge of the solid fuel $z = 0.04$m ignites first as this is located closer to the burner. As indicated in the

figure, the temperature at this location is higher than the rest of the fuel at all time instants. At time $t = 5, 6, 7$s the temperature increases due to ignition and it is observed that the region located between the center and trailing edge of the fuel exhibit lower values of temperature compared to values at the trailing edge. Also it appears that at these time instants, a reaction front initially located at $z = 0.046$m at $t = 6$s travels towards the trailing edge of the fuel with time. At $t = 9$s, when most of the solid fuel has burnt out, the reaction front reaches the trailing edge as evident from the figure.

Figures 6.7(a-b), representing two-dimensional contours of temperature, has been plotted at $t = 7, 7.5$s allows investigation of the variation of temperature along the length and thickness of the fuel. As discussed earlier, the trialing edge in fig. 6.7 (a, b) is heated prior to the region located at the center of the solid fuel. This could be attributed to two reasons- 1) tilting of the flame formed initially at the leading edge under the influence of hot gases from the burner during which it makes contact with the trailing edge, preheating it before the region located at the center 2) a boundary layer could be formed on the surface of solid fuel due to flow of hot gases from the burner, reducing the heat transfer in this region. Also, from this figure we observe a reaction front travelling from the leading edge to the trailing edge of the fuel.

Figure 6.8 illustrates the variation of temperature and vertical component of velocity along the length of the solid fuel, at $y = -0.0012$m and $x = 0$m at time $t = 4$s. This represents the variation along a line just above the surface of the solid fuel in the gas phase domain while noting that the solid fuel is located between $z = 0.04$ and $z = 0.07$. At this time instant, the leading edge of the solid fuel has

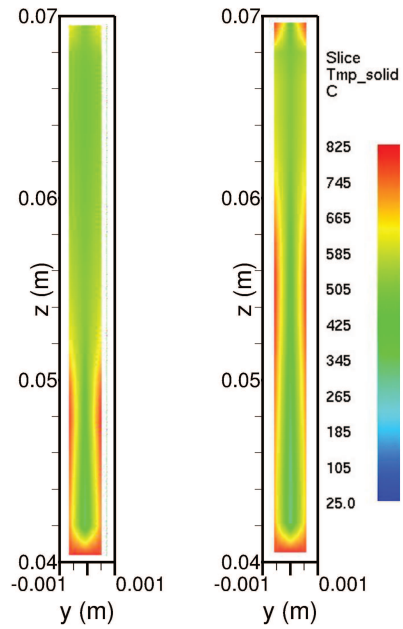

Figure 6.7: Contours of temperature within the solid fuel along a zy slice at (a) $t = 7$ s (b) $t = 7.5$ s and located at $x = 0$ m for a case with an initial FMC of 65%.

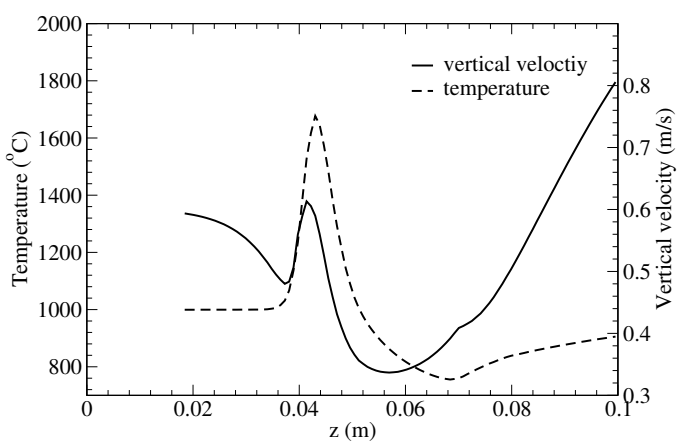

Figure 6.8: Variation of temperature and vertical component of velocity along z axis at point $y = -0.0012$m and $x = 0$m at time $t = 4$s

ignited. As a result, the temperature and velocity is higher at this point. As the flow of hot air encounters the solid fuel, it creates a boundary layer above the surface of the solid. From fig. 6.8, the effects of boundary layer can be observed as the velocity is reduced from 0.6 m/s at the leading edge of the solid fuel to 0.25 m/s at the trailing edge. Similarly we observe that the temperature is reduced by 200°C in the gas phase domain at these locations. This reduction could be attributed to the growth in boundary layer over the surface of the solid fuel. Beyond the trailing edge of the solid fuel the temperature and velocity show an increase.

The spatial variation of free water mass fraction within the solid fuel was plotted along an zx slice at time instants $t = 3, 3.5, 4$s in fig. 6.9a-c. From this figure we observe the heating pattern at the time of ignition. In fig. 6.9(a) a drying front propagated from the leading edge to the center with time along the z direction. However in fig. 6.9(b) and (c), before the drying front reached the center, the lateral and trailing edge of the fuel appear to have undergone evaporation. Evaporation occurred at the leading, lateral and trailing edge of the solid fuel at a higher rate compared to the region located at the center. As discussed in connection with fig. 6.7, this could be due to flame tilt which makes contact with the trailing edge, preheating it before the center. In addition, the boundary layer growth above the surface of the solid fuel as discussed in fig. 6.8 could lower the heat transfer in the center region. These results are in general agreement with the observation made by Prince *et al.* [44] through their IR measurements. It is important to note that in case of experiments, the leaves tested could have non-homogeneous distribution of moisture content initially, or there may be variation in thickness *i.e.* the center of the fuel

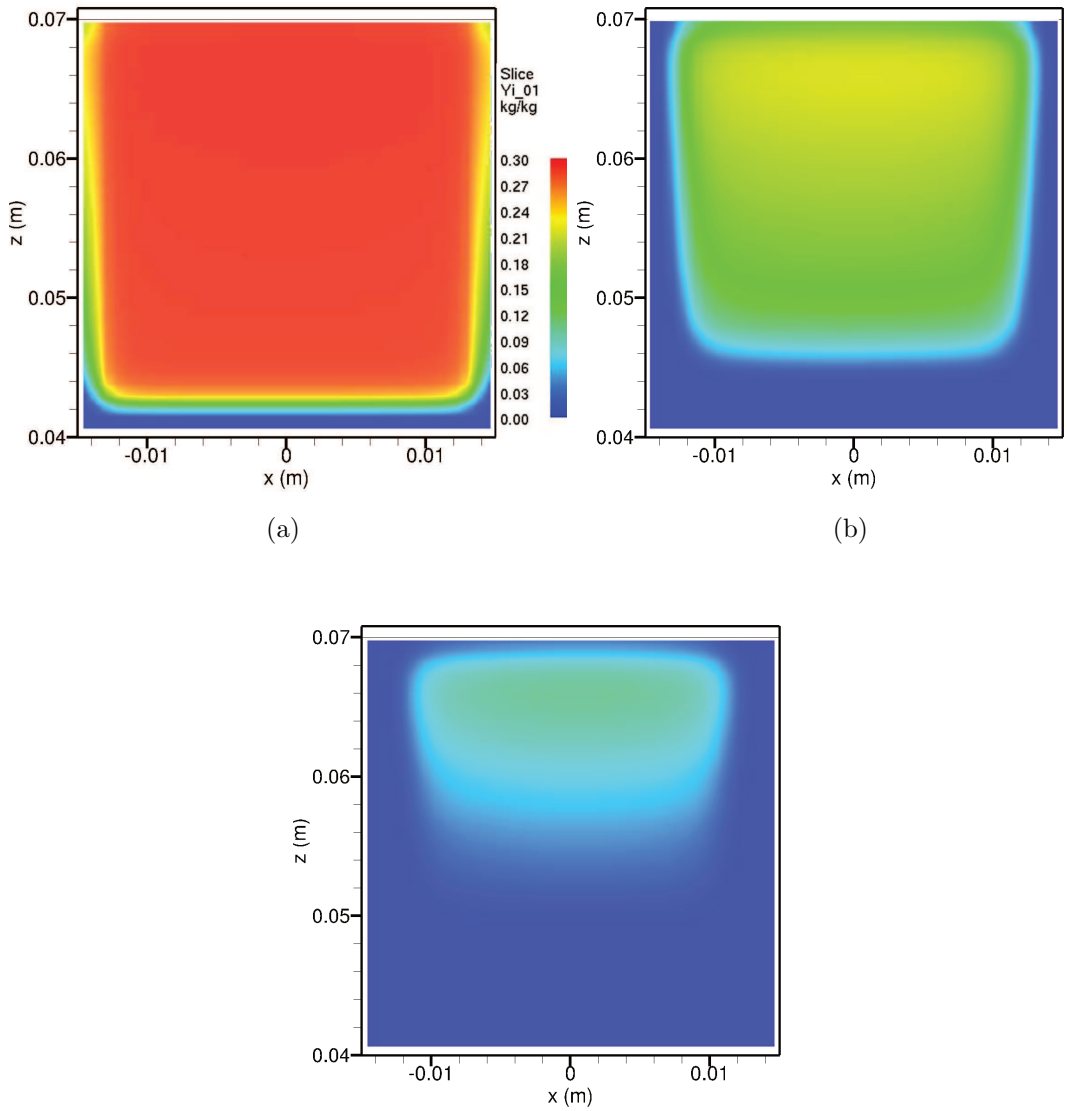

Figure 6.9: Contours of moisture mass fraction in the solid fuel at (a) $t = 3$ s (b) $t = 3.5$ s and (c) $t = 4$ s on a xz-slice located at $y = 0$ m for a case with an initial FMC of 65%.

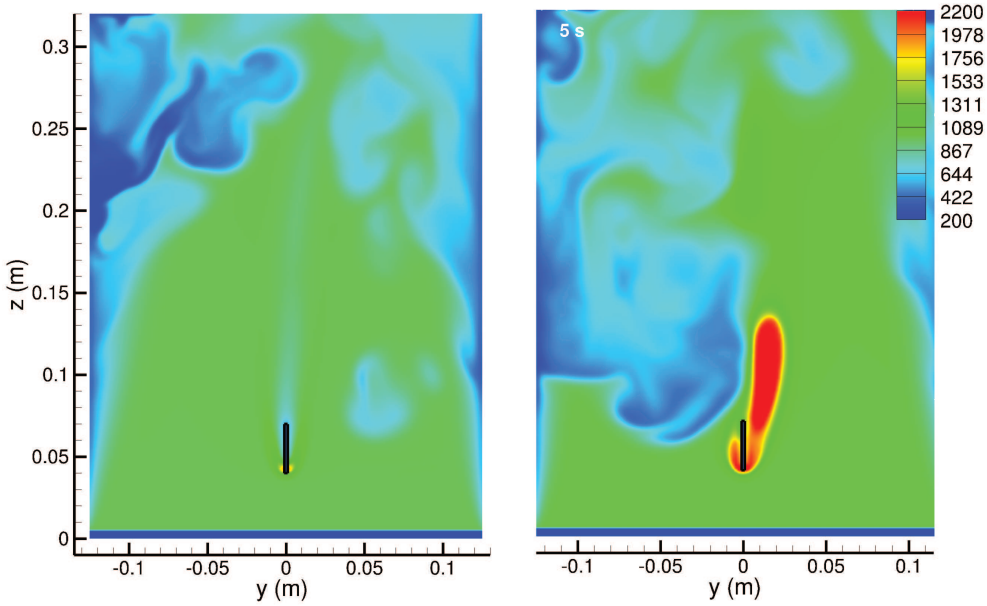

(a) (b)

Figure 6.10: Contours of gas-phase temperature at times (a) $t = 3$ s, and (b) $t = 4.75$ s on a yz slice located at $x = 0$ for a case with an initial FMC of 65% using convection-only heating.

could be thicker/thinner compared to other regions. Such an initial condition has been neglected in the present simulation. These factors can also influence the heating pattern discussed here.

Now the focus is shifted to the gas phase region computed by FDS. Two-dimensional contours of temperature on a yz slice passing through $x = 0$ are plotted at times $t = 3$s and $t = 4.75$s in figs. 6.10(a) and (b), respectively. In fig. 6.10(a), strong mixing between the ambient air and the hot air that exits the burner is observed. Since solid wall boundary conditions were used to model the glass cage used in FFB apparatus, boundary layers are also observed near the sidewalls. Also the tip of the

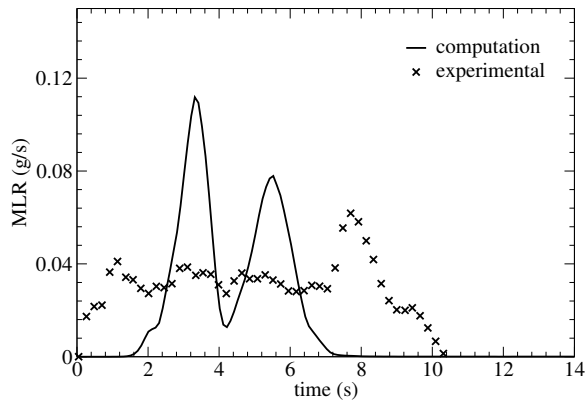

Figure 6.11: Comparison of time histories of mass loss rate (solid line) with experimental results of manzanita species (symbols) for an initial FMC of 65% using convection-only heating.

solid fuel appears to have ignited at this time instant. At $t = 4.75$s in fig. 6.10(b), the ignition zone has spread towards the trailing edge of the solid fuel.

6.3.2 Combined Convection and Radiation Heating

The time history of MLR for FMC of 65% under combined heating mode is shown in fig. 6.11. It is seen that the simulation over predicts the experimental peak mass loss rate, as was also the situation in the convective heating studies. Due to the presence of radiation, the peak MLR is 20% higher than that in convection-only case (fig. 6.2). The burn out time was around 7.1s in comparison to 10s in experiments. Due to the presence of radiation, the solid fuel was consumed approximately 1s earlier than convective heating case discussed in Section 6.3.1.

The evolution of overall MLR and HRR under the influence of combined mode and convection-only heating are plotted in fig. 6.12 for a FMCs of 65%. In fig. 6.12 (a), the initiation of moisture loss occurred at 1.9s for both cases. Also, we observe

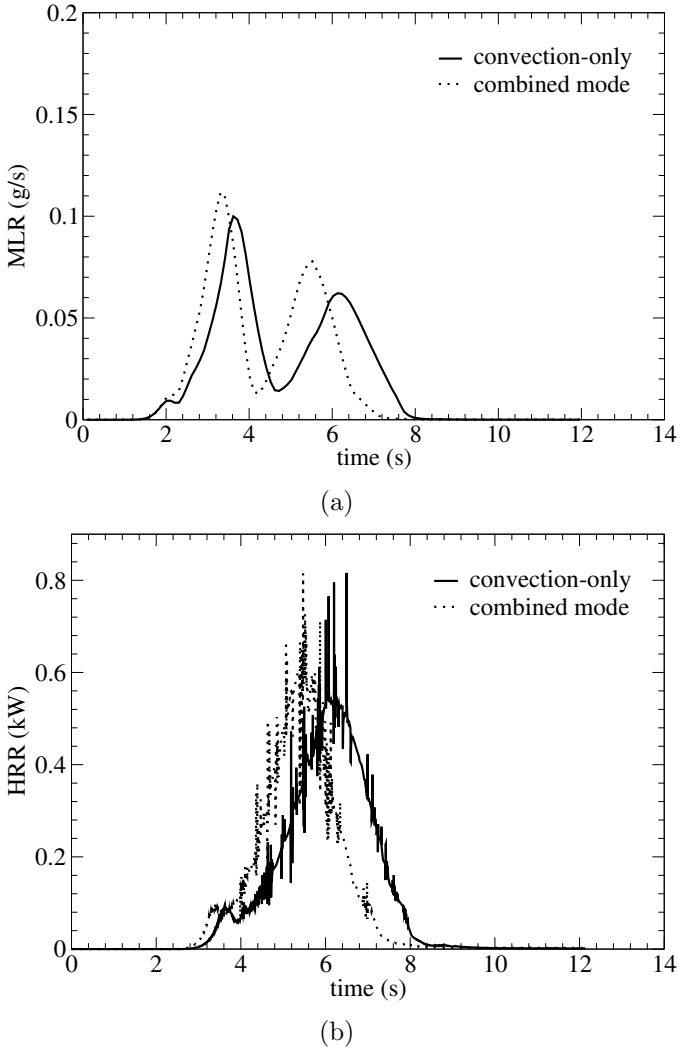

Figure 6.12: Comparison between time histories of (a) mass loss rate (b) heat release rate, using convection-only (solid line) and combined heating mode (dashed line) for an initial FMC of 65%.

two peaks, one at $t = 3s$ and the other at $t = 5.5$s. The first peak is due to evaporation while the second peak is due to ignition. It appears that the difference in the MLR peaks between the convective-only and combined heating mode at $t = 5.5$s is higher than the difference value at time instant $t = 3$s. This effect of radiation on ignition can also be observed from the HRR plots. This figure indicates that when radiation

is used as the heating source, it has significant impact on the processes after ignition, while the preheating process is only marginally affected.

6.4 Chapter Summary

The effect of heating mode and moisture content on pyrolysis and combustion of a vertically oriented manzanita species was investigated. The simulations were carried out by using a detailed 12-step kinetic mechanism as the pyrolysis model. Using a three dimensional computational model, it was compared with the experimental data obtained by the FFB apparatus for both convection-only and combined radiation-convection heating. The simulation and experimental results were consistent as far as ignition time, fire initiation and spread pattern were concerned. In the solid fuel, local evaporation of moisture and rise of temperature was observed along the leading, lateral and trailing edge of the fuel. Furthermore, a significant amount of moisture remained at the center of the sample at the time of ignition, suggesting that different points in the domain pyrolyze at different instants. When FMCs of 44, 65 and 90% were considered, it was observed that the temperature response was higher for the case with 44% FMC and ignition occurred prior to the 65 and 90% FMC case; however, the MLR values were small for lower FMC case. For the combined heating mode case, the peak MLR was found 20% higher as compared to the convection-only heating case.

CHAPTER 7

CONCLUSIONS AND FUTURE WORK

7.1 Summary and Conclusions

Multiple sets of simulations were carried out to investigate the ignition and pyrolysis of live fuels under various heating conditions.

First, the simulations were conducted for dry woody materials to model thick branches neglecting the effect of moisture content and focused on the decomposition of the solid phase. Quantities such as ignition time, mass loss rate and charring rate were analyzed under the influence of convection and/or radiation. The effects of the flame dynamics in the gas phase were neglected and a one-dimensional slab configuration was used for the solid phase. The chemistry was simplified through assuming one-step kinetic mechanism for the wood decomposition. The increase in radiative source temperature in presence of convection substantially affected the ignition time; however, there were marginal effects on mass loss rate and charring rate. In case of convective heating in presence of radiation, ignition time was marginally affected; however, mass loss rate and charring rate were not affected.

Then, a leaf-like three dimensional configuration was studied with the full effects of the surrounding gas phase taken into account. Effects of moisture content

on ignition was the main focus and the fuel considered was assumed cellulose, which is a more realistic species than wood for a leaf. The solid fuel was under the radiative heating only and a 5-step chemical kinetic mechanism was used for pyrolysis. The modeling was carried out by a fully coupled solid-gas solver Gpyro-3D / FDS. Fuel moisture content of 5%, 40% and 80% were considered. It was shown that the temperature response and thermal degradation rate was higher for the case with 5% FMC and ignition occurred prior to the 40% and 80% FMC case. The simulations also indicated that water evaporated locally near the point of ignition while present elsewhere with fuel, indicating that different points in the fuel evaporate and pyrolyse at different times. Local peaks in the mass fraction of moisture was observed at a region located close to lateral edges of the solid fuel, which indicates a non-uniform evaporation phase during ignition of the fuel. In the gas phase, a high volume fraction of water vapor observed in the region close to the combustion zone as well as away from this region illustrated that evaporation and ignition can occur together. Oxygen was displaced by water vapor during evaporation ahead of the ignition zone, indicating that FMC of the fuel affected not only the pyrolysis process but also the gas phase combustion.

In the next task of the modeling activities, an improved chemistry model was used, which included hemicellulose and lignin along with cellulose and moisture. It was a 12-step kinetic mechanism for the solid phase to simulate the multi-component decomposition process in detail. This allowed to investigate the effect of different states of moisture on the ignition behavior of a leaf-like fuel under the influence of convective heat transfer. The solid fuel was oriented horizontally to mimic the burn-

ing experiments of individual manzanita (Arctostaphylos glandulosa) species leaves by the Flat Flame Burner (FFB) apparatus. The modeling results were consistent with the experimental results in terms of ignition and burnout time prediction, fire initiation and spread pattern. Free water evaporated before ignition occurred and it affected the temperature response of the solid fuel. The evaporation of bound water occurred at the point of ignition and the evaporation continued until most of the fuel was burnt out. Water vapor in the gas phase due to bound water evaporation reduced the oxygen concentration around the solid fuel thereby affecting the gas phase combustion process. Evaporation occurred initially at the periphery of the solid fuel and a significant amount of moisture remained at the center of the fuel at the time of ignition, indicating that different points in the domain evaporate and pyrolyze at different times. The heating pattern observed here was attributed to the the formation of vortices above the surface of the solid fuel which deviates the path of hot gases thus lowering the temperature in that region.

In the final task, the previous study was repeated after the orientation of the fuel element was changed to a vertical direction. The modeling results were compared against the individual live fuel burn data of a vertically oriented manzanita species obtained using the FFB apparatus for both convection-only and combined radiation-convection heating. The modeling and experimental results were in a good agreement as far as ignition time, fire initiation and spread pattern were concerned. In the solid fuel, local evaporation of moisture was observed at a point closer to the burner. Furthermore, a significant amount of moisture remained in the sample at the time of ignition, suggesting that different points in the domain pyrolyze at different instants.

Evaporation occurred at a higher rate near the leading, lateral and trailing edge of the solid fuel compared to the region located at the center. This pattern of heating was either due to the flame tilt observed during simulation or due to the effect of fluid dynamics, where a boundary layer growth was observed above the surface of the solid fuel. These observations were in general agreement with the observation made through experiments. However is important to note that in case of experiments, the leaves tested could have non-homogeneous distribution of moisture content initially, or there may be variation in thickness *i.e.* the center of the fuel could be thicker/thinner compared to other region. These factors were neglected in modeling, which could have in impact on the heating pattern.

7.2 Future Work

During this investigation, certain assumptions were intrinsic to the numerical model – 1) uniform distribution of moisture, cellulose, hemicellulose and lignin within the solid fuel initially 2) the thermophysical properties used for the solid phase species were isotropic. This may not be an accurate representation of a live fuel. However, with the aid of experiments in characterising the live fuel species, simulations in the future could mimic live fuels more closely.

A 12-step kinetic mechanism was used within the solid fuel to predict the experimental mass loss rate. The results obtained were satisfactory, however this could be further improved by modifying this kinetic model using genetic algorithm approach [3].

In the gas phase domain, a one-step model was used to model the combustion reaction. The combustion model used was based on Eddy dissipation Concept which assumes infinitely fast chemistry. The turbulence model used was based on constant Smagorinsky. These factors play a major role in simulating the ignition behavior and could be improved using: 1) A muti-step reaction mechanism in the gas phase domain, 2) Finite rate chemistry, 3) Dynamic Smagorinsky model to deal with turbulence.

Within the solid fuel, pyrolysate and tar were the gas species formed as a result of decomposition. Pyrolysate was allowed to diffuse into the gas phase domain however tar remained within the solid, some of which underwent oxidation reaction. Tar could be allowed to diffuse into the gas phase similar to pyrolysate, and its reaction with oxygen could be modeled separately.

The results pertaining to the gas phase domain is dependent on the grid size used due to the LES approach adopted here. Results could be regenerated using a higher resolution to analyze the grid dependence.

APPENDICES

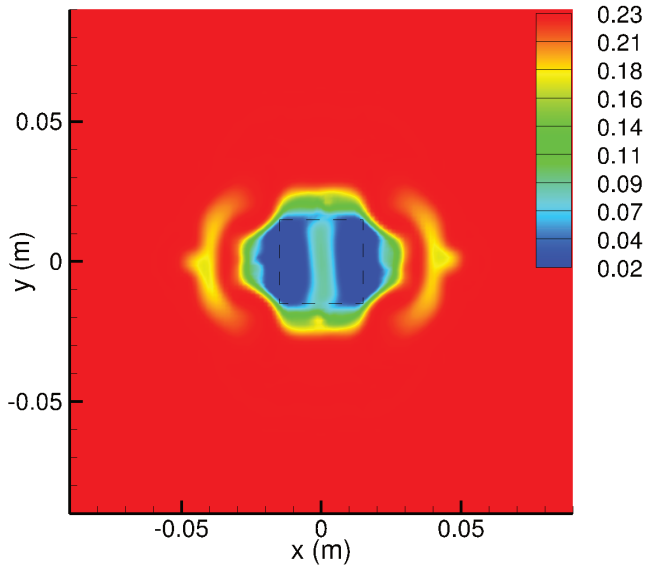

(a)

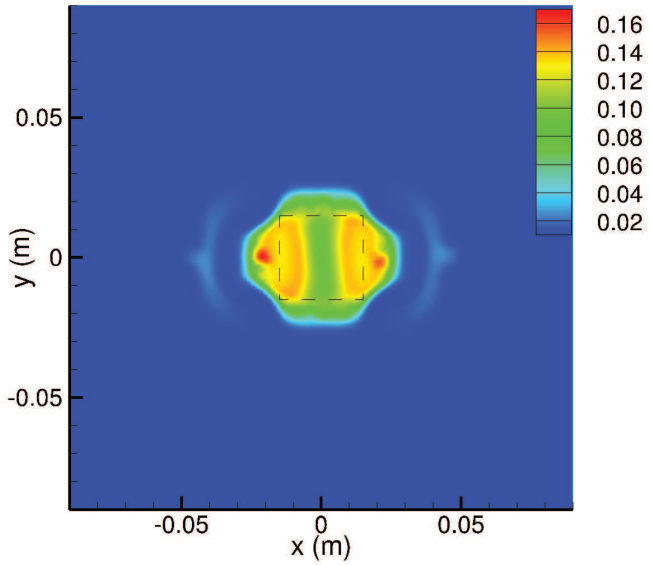

(b)

Figure 1: Two dimensional contours of a) oxygen mass fraction b) mass fraction of carbon dioxide along a xy slice located at $z = 0.6$ for an initial FMC of 65%.

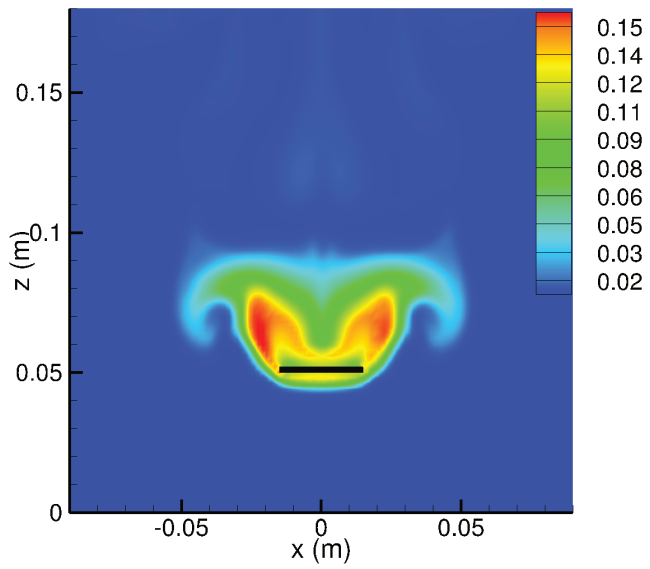

(a)

Figure 2: Two dimensional contours of water vapor mass fraction along a xz slice located at $y = 0$ for an initial FMC of 65%.

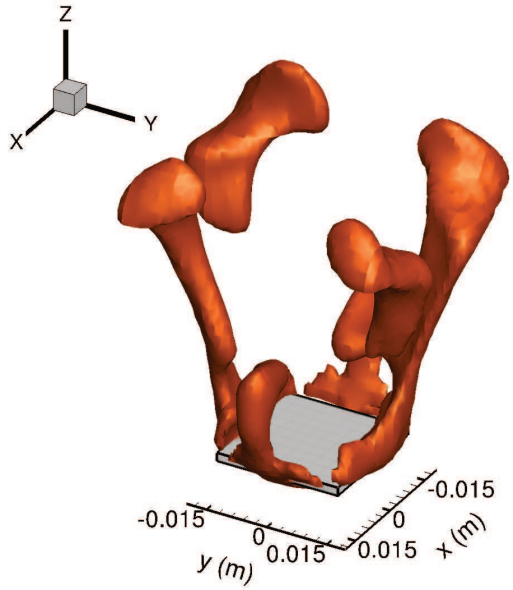

(a)

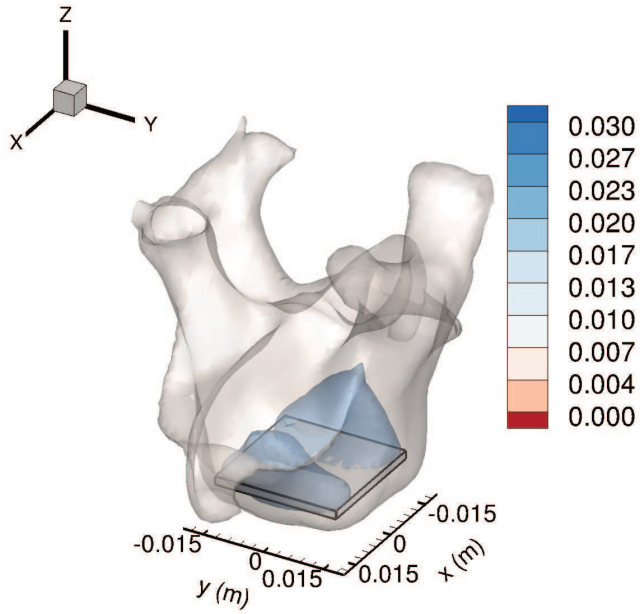

(b)

Figure 3: Iso-surface of a) temperature at 2000 ^{o}C and b) water vapor mass fraction value of $0.01, 0.03$ at $t = 9$s for an initial FMC of 65%.

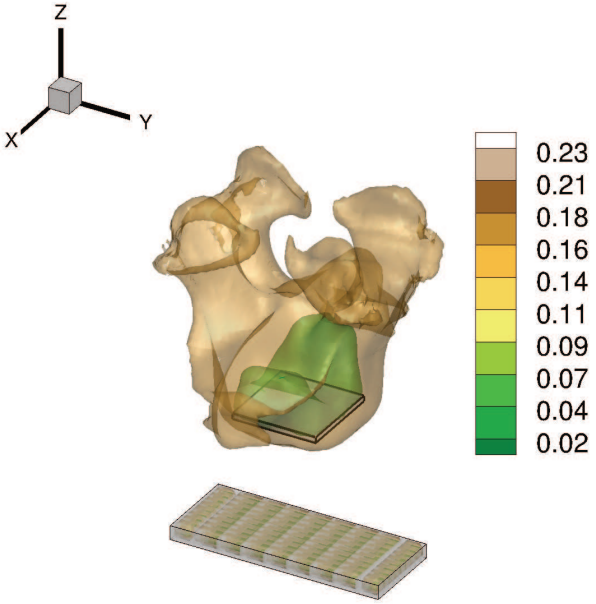

(a)

Figure 4: Iso-surface of oxygen mass fraction value of $0.04, 0.23$ at $t = 9$s for an initial FMC of 65%.

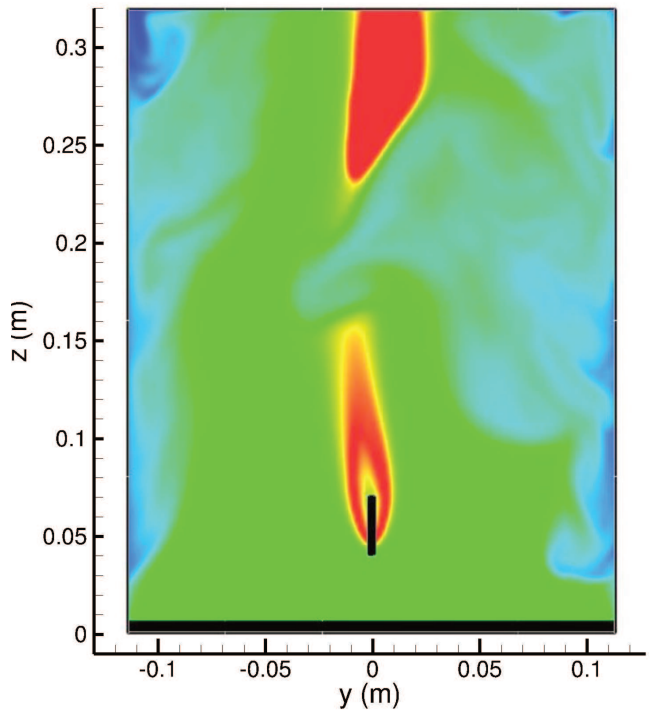

(a)

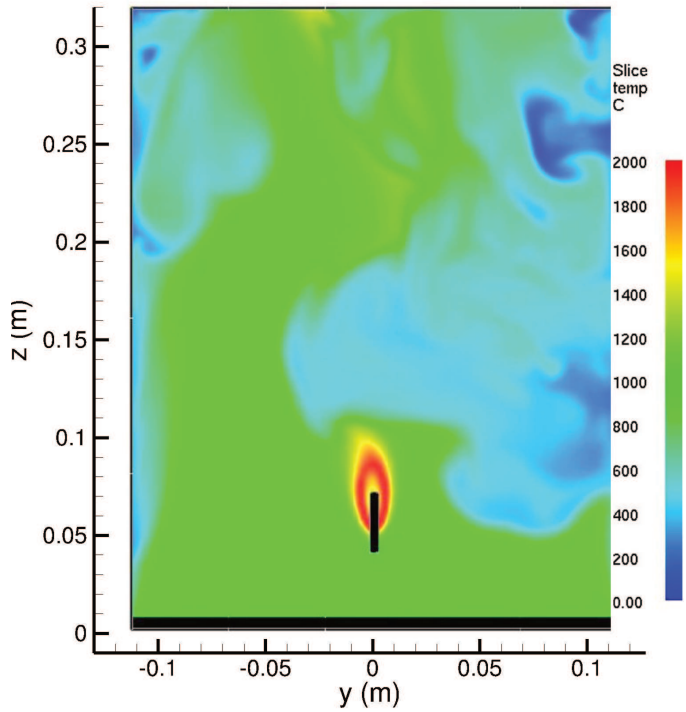

(b)

Figure 5: Two dimensional contours of temperature along a yz slice located at $x = 0$ for an initial FMC of 65% for convection-only heating case at time instants (a) $t = 7$s and (b) $t = 7.5$s.

REFERENCES

[1] G. H. Yeoh and K. K. Yuen. *Computational fluid dynamics in fire engineering: theory, modelling and practice*. Butterworth-Heinemann, 2009.

[2] T.J. Ohlemiller, T. Kashiwagi, and K. Werner. Wood gasification at fire level heat fluxes. *Combustion and Flame*, 69(2):155–170, 1987.

[3] C. Lautenberger and C. Fernandez-Pello. A model for the oxidative pyrolysis of wood. *Combustion and Flame*, 156(8):1503–1513, 2009.

[4] C. Di Blasi. Numerical simulation of cellulose pyrolysis. *Biomass and Bioenergy*, 7(1-6):87–98, 1994.

[5] T. B. Reed and F. Posey. Unpublished data, 1980. Solar Energy Research Institute (SERI) is now National Renewable Energy Laboratory (NREL).

[6] R. S. Miller and J. Bellan. A generalized biomass pyrolysis model based on superimposed cellulose, hemicelluloseand lignin kinetics. *Combust. Sci. Technol.*, 126:97 – 137, 1997.

[7] C. A. Koufopanos, A. Lucchesi, and G. Maschio. Kinetic modelling of the pyrolysis of biomass and biomass components. *Can. J. Chem. Eng.*, 67(1):75–84, 1989.

[8] B. M. Pickett, C. Isackson, R. Wunder, T. H. Fletcher, B. W. Butler, and D. R. Weise. Experimental measurements during combustion of moist individual foliage samples. *International Journal of Wildland Fire*, 19:153–162, 2010.

[9] K. McGrattan, R. McDermott, S. Hostikka, and J. Floyd. Fire dynamics simulator (version 5): User's guide. Special Publication 1019-5, U.S. Department of Commerce, National Institute of Standards and Technology, 2007.

[10] California Department of Forestry and Fire Protection (www.fire.ca.gov). Benefits of fire, 2012.

[11] National Interagency Coordination Center. Wildland fire summary and statistics annual report. Technical report, National Interagency Fire Center, 3833 S. Development Ave., Boise, Idaho, 83705, 2012.

[12] A. L. Westerling, H. G. Hidalgo, D. R. Cayan, and T. W. Swetnam. Warming and Earlier Spring Increase Western U.S. Forest Wildfire Activity. *Science*, 18(5789):940 – 943, Aug. 2006. Published Online July 6 2006.

[13] S. W. Running. Is Global Warming Causing More, Larger Wildfires? *Science*, 313(5789):927 – 928, Aug. 2006. Published Online July 6 2006.

[14] A. M. Grishin. *Mathematical Modelling of Forest Fires and New Methods of Fighting Them*. Publishing House of Tomsk State University, Tomsk, Russia, 1997.

[15] R. E. Keane, J. K. Agee, P. Fulé, J. E. Keeley, C. Key, S. G. Kitchen, R. Miller, and L. A. Schulte. Ecological effects of large fires on US landscapes: benefit or catastrophe? *International Journal of Wildland Fire*, 17:696 – 712, 2008.

[16] National Wildfire Coordinating Group. Wildland Fire Suppression Tactics Reference Guide. Technical Report PMS - 465, National Wildfire Coordinating Group Traning Working Team, April 1996.

[17] H.E. Schimke and L. R. Green. Prescribed fire for maintaining fuel-breaks in the central Sierra Nevada. GPO, USDA Forest Service, Pacific Southwest Forest and Range Exp. Sta., 1970.

[18] L. R. Green. Burning by Prescription in Chapparal. General Technical Report PSW-51, USDA Forest Service, 1981.

[19] M. A. Reams, T. K. Haines, C. R. Renner, M. W. Wascom, and H. Kingre. Goals, obstacles and effective strategies of wildfire mitigation programs in the Wildland−Urban interface. *Forest Policy and Economics*, 7(5):818 – 826, 2005.

[20] R.C. Rothermel. A mathematical model for predicting fire spread in wildland fuels. Research Paper INT-115, U.S. Department of Agriculture, Intermountain Forest and Range Experiment Station, Ogden, UT, 1972.

[21] P. Andrews. Behave: fire behaviour prediction and fuel modelling system – burn subsystem, part 1. General Technical Report INT-194, U.S. Department of Agriculture, Forest Service, Intermountain Forest and Range Experiment Station, Ogden, UT, 1986.

[22] M. A. Finney. Farsite fire area simulator: Model development and evaluation. Special Publication RMRS-RP-4, U.S. Department of Agriculture, Forest Service, Rocky Mountain Research Station, 1998.

[23] F. Shafizadeh. *The Chemistry of Pyrolysis and Combustion*, chapter 14, pages 489–529. American Chemical Society, 1984.

[24] A. J. Stamm. Thermal degradation of wood and cellulose. *Industrial & Engineering Chemistry*, 48(3):413–417, 1956.

[25] D. Meier and O. Faix. State of the art of applied fast pyrolysis of lignocellulosic materials a review. *Bioresource Technology*, 68(1):71 – 77, 1999.

[26] M. Brebu and C. Vasile. Thermal degradation of lignin - a review. *Cellulose Chemistry and Technology*, 44(9):353–363, 2010.

[27] Jacques Ld. Cellulose pyrolysis kinetics: An historical review on the existence and role of intermediate active cellulose. *Journal of Analytical and Applied Pyrolysis*, 94:17–32, 2012.

[28] F. J. Kilzer and A. Broido. Speculations on the nature of cellulose pyrolysis. *Pyrodynamics*, 2:151–163, 1965.

[29] P.K. Chatterjee and C.M. Conrad. Kinetics of the pyrolysis of cotton cellulose. *Textile Research Journal*, 36:487–494, 1966.

[30] F. Shafizadeh. *Pyrolytic Reactions and Products of Biomass*, chapter 11, pages 183–217. Springer Netherlands, Dordrecht, 1985.

[31] R. Capart, L. Khezami, and A. K. Burnham. Assessment of various kinetic models for the pyrolysis. *Thermochimica Acta*, 417:79 – 89, 2004.

[32] P.C. Lewellen, W.A. Peters, and J.B. Howard. Cellulose pyrolysis kinetics and char formation mechanism. *Symposium (International) on Combustion*, 16(1):1471 – 1480, 1977.

[33] A. G. W. Bradbury, Y. Sakai, and F. Shafizadeh. A kinetic model for pyrolysis of cellulose. *Journal of Applied Polymer Science*, 23:3271–3280, 1979.

[34] N. Bech, M. B. Larsen, P. A. Jensen, and K. D. Johansen. Modelling solid-convective flash pyrolysis of straw and wood in the pyrolysis centrifuge reactor. *Biomass and Bioenergy*, 33:999–1011, 2009.

[35] D. R. Weise and C. S. Wright. Wildland fire emissions, carbon and climate: Characterizing wildland fuels. *Forest Ecology and Management*, 317:26–40, 2013.

[36] R. M. Nelson, Jr. Water relations of forest fuels. In E.A. Johnson and K. Miyanishi, editors, *Forest Fires: Behavior and Ecological Effects*, pages 79–149. Academic Press, San Diego, CA, 2001.

[37] W. Matt Jolly, Ann M. Hadlow, and Kathleen Huguet. De-coupling seasonal changes in water content and dry matter to predict live conifer foliar moisture content. *International Journal of Wildland Fire*, 23(4):480, 2014.

[38] M. Janssens. Piloted ignition of wood: a review. *Fire Materials*, 15(4):151 – 167, 1991.

[39] D. L. Simms and M. Law. The ignition of wet and dry wood by radiation. *Combustion and Flame*, 11(5):377–388, 1967.

[40] Byram G. M. Combustion of forest fuels. In Davis K. P., editor, *Forest fire: control and use*. McGraw Hill, San Diego, CA, 1959.

[41] S. C. Ferguson, A. Dahale, B. Shotorban, S. Mahalingam, and D. R. Weise. The role of moisture on combustion of pyrolysis gases in wildland fires. *Combustion Science and Technology*, 185:435–453, 2013.

[42] X. Zhou, S. Mahalingam, and D. R. Weise. Modeling of marginal burning state of fire spread in live chaparral shrub fuel bed. *Combustion and Flame*, 143(3):183–198, 2005.

[43] K. M. Yedinak, J. D. Cohen, J. M. Forthofer, and M. A. Finney. An examination of flame shape related to convection heat transfer in deep-fuel beds. *International Journal of Wildland Fire*, 19(2):171–178, 2010.

[44] D. R. Prince and T. H. Fletcher. A combined experimental and theoretical study of the combustion of live vs. dead leaves. In *8th US National Combustion Meeting of the Combustion Institute, Park City, UT*, 2013.

[45] C.E. Van Wagner et al. Calculations on forest fire spread by flame radiation. 1967.

[46] G .M. Byram, H. B. Clements, E. R. Elliott, and P. M. George. An experimental study of model fires. Technical report, DTIC Document, 1964.

[47] P. H. Thomas, D. L. Simms, and H. G. Wraight. Fire spread in wooden cribs. *Fire Safety Science*, 537:1–1, 1964.

[48] H. E. Anderson and R. C. Rothermel. Influence of moisture and wind upon the characteristics of free-burning fires. In *Symposium (International) on Combustion*, volume 10, pages 1009–1019. Elsevier, 1965.

[49] H. E Anderson. *Heat transfer and fire spread*. Intermountain Forest and Range Experiment Station, Forest Service, US Department of Agriculture, 1969.

[50] D. Frankman, B. W. Webb, B. W. Butler, and D. J. Latham. Fine fuel heating by radiant flux. *Combustion Science and Technology*, 182(2):215–230, 2010.

[51] F. A. Albini. A model for fire spread in wildland fuels by-radiation. *Combustion Science and Technology*, 42(5-6):229–258, 1985.

[52] P. J. Pagni and T. G. Peterson. Flame spread through porous fuels. In *Symposium (International) on Combustion*, volume 14, pages 1099–1107. Elsevier, 1973.

[53] R. C. Rothermel, H. E. Anderson, et al. Fire spread characteristics determined in laboratory. 1966.

[54] R. O. Weber. Modelling fire spread through fuel beds. *Progress in Energy and Combustion Science*, 17(1):67–82, 1991.

[55] J-L Dupuy. Testing two radiative physical models for fire spread through porous forest fuel beds. *Combustion Science and Technology*, 155(1):149–180, 2000.

[56] B. W. Butler, J. Cohen, D. J. Latham, R. D. Schuette, P. Sopko, K. S. Shannon, D. Jimenez, and L. S. Bradshaw. Measurements of radiant emissive power and temperatures in crown fires. *Canadian Journal of Forest Research*, 34(8):1577–1587, 2004.

[57] W. R. Anderson, E. A. Catchpole, and B. W. Butler. Convective heat transfer in fire spread through fine fuel beds. *International journal of wildland fire*, 19(3):284–298, 2010.

[58] D. I. Lawson and D. L. Simms. The ignition of wood by radiation. *British Journal of Applied Physics*, 3(9):288, 1952.

[59] S. McAllister, I. Grenfell, A. Hadlow, W.M. Jolly, M. Finney, and J. Cohen. Piloted ignition of live forest fuels. *Fire Safety Journal*, 51:133–142, 2012.

[60] V. Babrauskas. *Ignition Handbook*. Fire Science Publishers, Issaquah, WA, 2003.

[61] T. H. Fletcher, B. M. Pickett, S. G. Smith, G. S. Spittle, M. M. Woodhouse, E. Haake, and D. R. Weise. Effects of moisture on ignition behavior of moist california chaparral and utah leaves. *Combustion Science and Technology*, 179(6):1183–1203, 2007.

[62] F. A. Albini. Estimating wildfire behavior and effects. General technical report INT-30, USDA Forest Service, 1976.

[63] A. L. Sullivan. Wildland surface fire spread modeling, 1990-2007. 1: Physical and quasi-physical models. *International Journal of Wildland fire*, 18:349 – 368, 2009.

[64] A. L. Sullivan. Wildland surface fire spread modeling, 1990-2007. 2: Empirical and quasi-empirical models. *International Journal of Wildland fire*, 18:369 – 386, 2009.

[65] A. L. Sullivan. Wildland surface fire spread modeling, 1990-2007. 3: Simulation and mathematical analogue models. *International Journal of Wildland fire*, 18:387 – 403, 2009.

[66] I. R. Noble, G. A. V. Bary, and A. M. Gill. McArthur's fire-danger meters expressed as equations. *Australian Journal of Ecology*, 5:201 – 203, 1980.

[67] X. Zhou, D. Weise, and S. Mahalingam. Experimental measurements and numerical modeling of marginal burning in live chaparral fuel beds. *Proceedings of the Combustion Institute*, 30(2):2287 – 2294, 2005.

[68] R. O. Weber. Modelling fire spread through fuel beds. *Progress in Energy and Combustion Science*, 17(1):67 – 82, 1991.

[69] R. C. Rothermel. A mathematical model for predicting fire spread in wildland fuels. Research paper int-115, USDA Forest Service, 1972.

[70] H. F. William. Fire spread through porous fuels from the conservation of energy. *Combustion and Flame*, 16(1):9 – 16, 1971.

[71] P. L. Andrews. BEHAVE: Fire Behavior Prediction and Fuel Modeling System - BURN Subsystem, Part 1. General Technical Report INT - 194, USDA Forest Service, Intermountain Research Station, Ogden, UT, 84401, 1986.

[72] Y. Haseli, J.A. van Oijen, and L.P.H. de Goey. Modeling biomass particle pyrolysis with temperature-dependent heat of reactions. *Journal of Analytical and Applied Pyrolysis*, 90(2):140 – 154, 2011.

[73] R. O. Weber. Toward a comprehensive wildfire spread model. *International Journal of Wildland Fire*, 1(4):245 – 248, 1991.

[74] C. W. Lautenberger. Gpyro3d: A three dimensional generalized pyrolysis model. *Fire Safety Science (IAFSS Symposium)*, 2014.

[75] N. Peters. Theoretical and Numerical Combustion. Cambridge university PressJohn Wiley and Sons, Cambridge, UK, 2000.

[76] T. Poinsot and D. Veynante. Turbulent Combustion. Edwards, second edition, 2005.

[77] B. F. Magnussen and B. H. Hjertager. On mathematical modeling of turbulent combustion with special emphasis on soot formation and combustion. *Symposium (International) on Combustion*, 16(1):719 – 729, 1977.

[78] W. Grosshandler. Radcal: A narrow band model for radiation calculations in a combustion environment. NIST Technical Note TN 1402, National Institute of Standards and Technology, Gaithersburg, Maryland, 1993.

[79] W. Mell, A. Maranghides, R. MecDermott, and S. L. Manzello. Numerical simulation and experiments of burning douglas fir trees. *Combustion and Flame*, 156:2023–2041, 2009.

[80] C. P. Bankston, B. T. Zinn, R. F. Browner, and E. A. Powells. Aspects of the mechanisms of smoke generation by burning materials. *Combustion and Flame*, 41:273–292, 1981.

[81] G. D. Raithby and E. H. Chui. A finite-volume method for predicting radiant heat transfer in enclosures with participating. *Journal of Heat Transfer*, 112 (2):415–423, 1990.

[82] J. P. Holman. *Heat Transfer*. McGraw–Hill, New York, 7th edition edition, 1990.

[83] R. B. Bird, W. E. Stewart, and E. N. Lightfoot. *Transport Phenomena, Revised 2nd Edition*. John Wiley and Sons, New York, 2007.

[84] L.H. Thomas. Elliptic problems in linear differential equations over a network. Report, Columbia University, Watson Scientific Computing Laboratory, New York, NY, 1949.

[85] S. V. Patankar. *Numerical Heat Transfer and Fluid Flow*. Hemisphere, New York, 1980.

[86] DK Shen, MX Fang, and WK Chow. Ignition of wood-based materials by thermal radiation. *International Journal on Engineering Performance-Based Fire codes*, 8:69–83, 2006.

[87] DL Simms and Margaret Law. The ignition of wet and dry wood by radiation. *Combustion and Flame*, 11(5):377–388, 1967.

[88] A. Atreya, C. Carpentier, and M. Harkleroad. Effect of sample orientation on piloted ignition and flame spread. *Fire Safety Science Proceedings*, page 97, 1986.

[89] H. E. Thomson, D. D. Drysdale, and C. L. Beyler. An experimental evaluation of critical surface temperature as a criterion for piloted ignition of solid fuels. *Fire Safety Journal*, 13(2):185–196, 1988.

[90] R. Bilbao, J. F. Mastral, J. F. Lana, J. A. Ceamanos, M. E. Aldea, and M. A. Betran. A model for the prediction of the thermal degradation and ignition of wood under constant and variable heat flux. *Journal of Analytical and Applied Pyrolysis*, 62(1):63–82, 2002.

[91] C. P. Brescianini, M. A. Delichatsios, and A. K. Webb. Mathematical modeling of timeto ignition in the early fire hazard test. *Combustion Science and Technology*, 175(2):319–331, 2003.

[92] M. A. Delichatsios. Piloted ignition times, critical heat fluxes and mass loss rates at reduced oxygen atmospheres. *Fire Safety Journal*, 40(3):197–212, 2005.

[93] V. Babrauskas. Ignition of wood: a review of the state of the art. *Journal of Fire Protection Engineering*, 12(3):163–189, 2002.

[94] Y Lizhong, G. Zaifu, Z. Yupeng, and F. Weicheng. The influence of different external heating ways on pyrolysis and spontaneous ignition of some woods. *Journal of Analytical and Applied Pyrolysis*, 78(1):40–45, 2007.

[95] Z. Tan, G. Su, and J. Su. Improved lumped models for combined convective and radiative cooling of a wall. *Applied Thermal Engineering*, 29(11):2439–2443, 2009.

[96] B. V. Babu and A. S. Chaurasia. Modeling for pyrolysis of solid particle: kinetics and heat transfer effects. *Energy Conversion and Management*, 44(14):2251–2275, 2003.

[97] C. Lautenberger and C. Fernandez-Pello. Approximate analytical solutions for the transient mass loss rate and piloted ignition time of a radiatively heated solid in the high heat flux limit. *Fire Safety Science*, 8:445–456, 2005.

[98] S. McAllister, M. Finney, J. Cohen, et al. Critical mass flux for flaming ignition of wood as a function of external radiant heat flux and moisture content. In *7th US national technical meeting of the Combustion Institute, Georgia Institue of Technology, Atlanta, GA*, pages 20–23, 2011.

[99] X. Zhou, S. Mahalingam, and D. Weise. Modeling of marginal burning state of fire spread in live chaparral shrub fuel bed. *Combustion and Flame*, 143(3):183–198, 2005.

[100] M. A. Finney, J. D. Cohen, S. McAllister, and W. M. Jolly. On the need for a theory of wildland fire spread. *International journal of wildland fire*, 22(1):25–36, 2013.

[101] Y. Haseli, J. A. van Oijen, and L. P. H. de Goey. Analytical solutions for prediction of the ignition time of wood particles based on a time and space integral method. *Thermochimica Acta*, 548:65–75, 2012.

[102] B. Benkoussas, J. L. Consalvi, B. Porterie, N. Sardoy, and J. C. Loraud. Modelling thermal degradation of woody fuel particles. *International Journal of Thermal Sciences*, 46(4):319–327, 2007.

[103] D. J. Rasbash, D. D. Drysdale, and D. Deepak. Critical heat and mass transfer at pilot ignition and extinction of a material. *Fire Safety Journal*, 10(1):1–10, 1986.

[104] T. L. Bergman, F. P. Incropera, and A. S. Lavine. *Fundamentals of heat and mass transfer*. John Wiley & Sons, 2011.

[105] M. G. Cruz, B. W. Butler, M. E. Alexander, and D. X. Viegas. Development and evaluation of a semi-physical crown fire initiation model. *Forest Ecology and Management*, (234):S96, 2006.

[106] P. L. Andrews et al. Modeling wind adjustment factor and midflame wind speed for rothermel's surface fire spread model. 2012.

[107] T. Defraeye, B. Blocken, and J. Carmeliet. Convective heat transfer coefficients for exterior building surfaces: Existing correlations and cfd modelling. *Energy Conversion and Management*, 52(1):512–522, 2011.

[108] B. W. Butler, J. Cohen, D. J. Latham, R. D. Schuette, P. Sopko, K. S. Shannon, D. Jimenez, and L. S. Bradshaw. Measurements of radiant emissive power and temperatures in crown fires. *Canadian Journal of Forest Research*, 34(8):1577–1587, 2004.

[109] K. M. Bryden, K. W. Ragland, and C. J. Rutland. Modeling thermally thick pyrolysis of wood. *Biomass and Bioenergy*, 22(1):41–53, 2002.

[110] H. Yang, R. Yan, H. Chen, D. H. Lee, and C. Zheng. Characteristics of hemicellulose, cellulose and lignin pyrolysis. *Fuel*, 86:1781–1788, 2007.

[111] K. W. Ragland and D. J. Aerts. Properties of wood for combustion analysis. *Bioresource Technology*, 37:161–168, 1991.

[112] C. M. Countryman. Moisture in living fuels affects fire behavior. *Fire Management Notes*, 35(2):10–14, 1974.

[113] V. Tihay and P. Gillard. Pyrolysis gases released during the thermal decomposition of three mediterranean species. *Journal of Analytical and Applied Pyrolysis*, 88(2):168–174, 2010.

[114] G. M. Byram. Combustion of forest fuels. In K.P. Davis, editor, *Forest fire: control and use*, pages 61–89. McGraw-Hill, New York, 1959.

[115] J. R. Gallacher, V. Lansinger, S. Hansen, D. Jack, D. R. Weise, and T. H. Fletcher. Effects of season and heating mode on ignition and burning behavior of three species of live fuel measured in a flat-flame burner system. Pasadena, CA, 2014. Spring Technical Meeting of the Western States Section of the Combustion Institute.

[116] B. M. Jenkins, L. L Baxter, T. R. Miles Jr, and T. R. Miles. Combustion properties of biomass. *Fuel Processing Technology*, 54:17–46, 1998.

[117] K. McGrattan, S. Hostikka, J. Floyd, H. Baum, R. Rehm, W. Mell, and R. McDermott. Fire dynamics simulator (version 5): Technical reference guide. Special Publication 1018-5, U.S. Department of Commerce, National Institute of Standards and Technology, 2007.

[118] M. Kokkala and D. Baroudi. A thermal model for upward flame spread on a combustible wall. Technical report, Valtion Teknillinen Tutkimuskeskus, Espoo, Finland, 1993.

[119] N. Boonmee and J. G. Quintiere. A theoretical investigation of surface glowing ignition leading to gas flaming autoignition. *Fire Safety Science–Proceedings of the 8th International Symposium*, pages 139–150, 2005.

[120] K. M. Bryden, K. W. Ragland, and C. J. Rutland. Modeling thermally thick pyrolysis of wood. *Biomass and Bioenergy*, 22:41–53, 2002.

[121] L. J. Curtiss and D. J. Miller. Transport model with radiative heat transfer for rapid cellulose pyrolysis. *Industrial and Engineering Chemistry Research*, 27:1775–1783, 1988.

[122] A. Dahale, S. Ferguson, B. Shotorban, and S. Mahalingam. Effects of distribution of bulk density and moisture content on shrub fires. *International Journal of Wildland Fire*, 22 (5):625–641, 2013.

[123] R. J. Ross. Wood handbook. General Technical Report FPLGTR190, Forest Products Laboratory, United States Department of Agriculture Forest Service, 2010.

[124] S. B. Pope. Ten questions concerning the large-eddy simulation of turbulent flows. *New journal of Physics*, 6(1):35, 2004.

[125] K. Hill, J. Dreisbach, F. Joglar, B. Najafi, K. McGrattan, R. Peacock, and A. Hamins. Verification and validation of selected fire models for nuclear power plant applications, volume 7: Fire dynamics simulator. Final Report NUREG-1824, U.S. Nuclear Regulatory Commission, Office of Nuclear Regulatory Research, 2007.

[126] B. L. Yashwanth, B. Shotorban, and S. Mahalingam. A computational investigation of the role of moisture in live fuels subject to pyrolysis and ignition through convective heat transfer. Cincinnati, OH, 2015. 9th US National Meeting Organized by the Central States Section of the Combustion Institute.

[127] B. L. Yashwanth, J. Gallacher, B. Shotorban, S. Mahalingam, T. H. Fletcher, and D. R. Weise. Experimental and numerical investigation of the effect of heating modes and moisture content on pyrolysis and ignition of live fuels. Cincinnati, OH, 2015. 9th US National Meeting Organized by the Central States Section of the Combustion Institute.

[128] J. J. Manya, V. Enrique, and L. Puigjaner. Kinetics of biomass pyrolysis: a reformulated three-parallel-reactions model. *Ind. Eng. Chem. Res.*, 42(3):434–441, 2003.

[129] T. R. Rao and A. Sharma. Pyrolysis rates of biomass materials. *Energy*, 23(11):973–978, 1998.

[130] Z. T. Yu, X. Xu, L. W. Fan, Y. C. Hu, and K. F. Cen. Experimental measurements of thermal conductivity of wood species in china: effects of density, temperature, and moisture content. *For. Product. J.*, 61(2):130–135, 2011.